BENEMÉRITA UNIVERSIDAD AUTÓNOMA DE PUEBLA

INSTITUTO DE FÍSICA “LUIS RIVERA TERRAZAS”

“ROLE OF DEFECTS IN THE MECHANICAL PROPERTIES OF GRAPHENE-COPPER HETEROSTRUCTURES”

TESIS

QUE PARA OBTENER EL GRADO DE

MAESTRO EN CIENCIAS
(EN LA ESPECIALIDAD DE CIENCIA DE MATERIALES)

PRESENTA
THAISON TALLES FELIX

DIRECTORA DE TESIS
DRA. LILIA MEZA MONTES

No. de CVU: 1007009

SEPTIEMBRE 2021

Acknowledgments

I would like to heartfully express my gratitude towards Dr. Lilia Meza Montes and Dr. María del Rayo Chávez Castillo for their guidance and support that immensely contributed to the development of this thesis.

Also, I genuinely thank all the staff and professors from Instituto de Física "Luis Rivera Terrazas" for their administrative support, maintenance, and adaptation during the COVID-19 pandemic.

Additionally, I thankfully acknowledge computer resources, technical advice and support provided by Laboratorio Nacional de Supercómputo del Sureste de México (LNS), a member of the CONACyT national laboratories, as well as CONACyT themselves for the given financial support during the course of my master's studies.

Finally, I thank Vicerrectoría de Investigación y Estudios de Posgrado for the support granted for the conclusion of this thesis within "Programa IV. Investigación y Posgrado. Apoyar a los programas de posgrado para lograr su incorporación al Padrón Nacional de Calidad. Indicador establecido en el Plan de Desarrollo Institucional 2017-2021".

Dedicated to...

my parents and family, who believed in me since the beginning of this journey;

to my friends, whom I could and can always count on;

and to Victoria and her family, who have provided me incredible support throughout my stay in Mexico.

Abstract

Through molecular dynamics simulations of tensile tests, the effect of vacancies and Stone-Wales defects in the mechanical properties of sandwich-like heterostructures, composed by graphene and two symmetric copper layers at a nanoscale, is studied. The dependency on the armchair and zigzag chiralities of the graphene layer is also investigated. The mechanical properties were determined through the analysis of the stress-strain curves obtained from the performed tensile tests. Also, the Young's modulus and Poisson's ratio were estimated. The effect of vacancies and Stone-Wales defects, which were introduced in the graphene layer at densities of 0.01, 0.02, and 0.03, were studied separately. Results for pristine systems were also obtained in order to get a good overview of how such defects modify the properties of the heterostructure. Furthermore, pristine and defective pure graphene nanoribbons and a pure copper nanofilm of comparable sizes to that of the heterostructure were also studied individually for a better understanding of their behavior under tensile load when assembled.

The results showed a decrease in the Young's modulus and in the yield strength of the materials as density of defects increases affecting, thereby, the stiffness of graphene-copper heterostructures. This effect was more noticeable when the defects were vacancies, which worsened this mechanical property more than Stone-Wales defects. However, the toughness and ductility of some of the defective systems, compared to the pristine ones, showed an improvement, specially in the zigzag chirality since, in general, they were tougher and more ductile than when the stress was applied along the armchair edge, as well as more elastic. Nonetheless, the armchair chirality made heterostructures stiffer. The same behavior was also observed in the analyzed pure graphene nanoribbons. Finally, all the analyzed graphene-copper heterostructures, pristine or defective, showed a substantial improvement in stiffness compared to the pure copper nanofilm. Though, pure copper was still more elastic than the heterostructures.

Our findings could be useful to understand the role defects play in the mechanical properties of graphene-based systems, as well as to appreciate the strengthening mechanism induced by this two-dimensional material in metals like copper. Moreover, they can be useful for the design of alike systems, which, in real life, are extremely likely to present defects of different types.

Resumen

Mediante simulaciones de dinámica molecular de ensayos de tracción, se estudia el papel que tienen las vacancias y defectos tipo Stone-Wales en las propiedades mecánicas de heteroestructuras tipo sándwich, compuestas por grafeno y dos capas simétricas de cobre a nanoescala. También se investiga la dependencia respecto a las quiralidades *armchair* y zigzag de la capa de grafeno. Las propiedades mecánicas se determinaron mediante el análisis de las curvas esfuerzo-deformación obtenidas de los ensayos de tracción. Asimismo, se estimaron el módulo de Young y el coeficiente de Poisson. El efecto de las vacancias y de los defectos tipo Stone-Wales, a densidades de 0.01, 0.02 y 0.03 en la capa de grafeno, se estudió por separado. También se estudiaron sistemas prístinos con el fin de obtener una visión general de cómo tales defectos modifican las propiedades de la heteroestructura. Además, nanocintas prístinas y defectuosas de grafeno puro y una nanopelícula de cobre puro, de tamaños comparables al de la heteroestructura, se estudiaron individualmente para comprender mejor su comportamiento bajo tracción cuando se ensamblan.

Los resultados mostraron una disminución en el módulo de Young y en el límite elástico de los materiales al aumentar la densidad de defectos, afectando, por lo tanto, la rigidez de las heteroestructuras. Este efecto fue más notorio con las vacancias, las cuales empeoraron esta propiedad más que los defectos Stone-Wales. Sin embargo, la tenacidad y ductilidad de algunos de los sistemas defectuosos en comparación con los prístinos mostraron una mejora, especialmente en la dirección zigzag ya que, en general, resultaron más tenaces y dúctiles que en el caso *armchair*, además de más elásticos. No obstante, En este último caso, los sistemas resultaron más rígidos. El mismo comportamiento también se observó en las nanocintas de grafeno puro. Finalmente, todas las heteroestructuras estudiadas, prístinas o defectuosas, mostraron una mejora sustancial en la rigidez en comparación con la nanopelícula de cobre puro. Sin embargo, el cobre puro resultó más elástico.

Nuestros hallazgos podrían ser útiles para comprender el papel de los defectos en las propiedades mecánicas de los sistemas basados en grafeno, así como para apreciar el mecanismo de fortalecimiento inducido por este material bidimensional en metales como el cobre. Además, pueden ser útiles para el diseño de sistemas similares, los cuales, en la vida real, tienen una alta probabilidad de presentar defectos de diferentes tipos.

Participation in Events

- Role of Defects in the Mechanical Properties of Graphene-Copper Heterostructures, T. T. Felix, L. Meza-Montes, Simposio estudiantil de posgrado en ciencia de materiales BUAP 2021, Puebla Pue., Mexico (2021).
- Rol de defectos en las propiedades mecánicas de heteroestructuras compuestas por grafeno y cobre, T. T. Felix, M. R. Chávez-Castillo, L. Meza-Montes, LXIV Congreso Nacional de Física, Tijuana BCN., Mexico (2021).

Contents

Guide to Figures

Guide to Tables

Chapter 1

Introduction

In 2004, through mechanical exfoliation of graphite, Kostia Novoselov and Andre Geim produced, for the first time, graphene, a material consisting of a single layer of carbon atoms arranged in a two-dimensional honeycomb lattice.[1,2] Since then, such material has been widely studied, and amazing properties and potential applications have been revealed. Perhaps, the mechanical properties are the most astonishing ones: a mono-layered pristine graphene sheet possesses incredible stiffness and tensile strength, around 1 TPa and 130 GPa, respectively. That makes graphene 200 times stronger than steel. Graphene has, therefore, the title of the strongest material ever tested.[3]

These superior mechanical properties allow the exploration of graphene as a reinforcement in other materials, e.g. metals like copper. The strengthening mechanism of nanolayered graphene-copper heterostructures was studied by Zhang *et al.* through molecular dynamics simulations of tensile tests.[4,5] An improvement on the stiffness, or Young's modulus, of pure copper nanofilms with the introduction of a layer of graphene was shown. Also, simultaneous positive and negative Poisson's ratio was found in such nanocomposites. The negative Poisson's ratio occurs when a material under tensile load presents an expansion perpendicular to the applied force. That characteristic defines an auxetic material. A conventional material, on the other hand, becomes thinner perpendicular to the applied force.

The combination of mono-layers to form heterostructures, such as the above mentioned graphene-copper one, has contributed to expand the field of study of complex materials. An important subject is the role defects play on their mechanical properties. It has been reported that the Young's modulus of graphene sheets with defects has a linear behavior

regarding the concentration of vacancies, with a slight drop regarding Stone-Wales defects. Furthermore, the presence of these defects can considerably reduce deformation and stiffness.[6,7] In addition, the study of other mechanical properties, including shear strength and accommodation capacity in the graphene-copper interface, depending on the quality of the graphene layer, suggests that the mechanical properties can be adjusted through interfaces designed with certain amount of defects.[8]

Thus, since these properties can be modified by defects, in this work the role of vacancies and Stone-Wales defects in the mechanical properties of graphene-copper heterostructures is studied. For that, molecular dynamics simulations of tensile tests were performed to obtain the stress-strain curves and estimate the Young's modulus and Poisson's ratio at different densities of defects in the graphene layer. Monovacancies and Stone-Wales defects are randomly introduced in the graphene layer, separately. The same trend was observed in three realizations of the distribution of defects, although for the sake of simplicity only one realization is presented in detail.

Our findings are reported in this thesis, which is organized as follows: in Chapter 1, which corresponds to this introduction, a brief presentation of graphene and graphene-copper heterostructures was made, as well as the problem statement. Following that, an overview on the determination of mechanical properties of materials is made, and further information about nanoscale graphene, copper, and graphene-copper heterostructures, focusing on their mechanical properties, is given in Chapter 2. Subsequently, the methodology of this work, which was based on molecular dynamics simulations, is described in Chapter 3, and in Chapter 4, the obtained results are presented and discussed. Thereafter, the conclusions and future work are presented in Chapter 5. Finally, in Appendices A, B, and C several snapshots of some of the performed tensile tests on the analyzed pure graphene nanoribbons, pure copper nanofilm, and graphene-copper heterostructures, respectively, are shown.

Chapter 2

Mechanical Behavior of Nanosystems

2.1 Mechanical Properties of Materials

In Materials Science and Engineering, some of the most widely studied properties of materials for applications in a variety of fields are the mechanical properties. These properties help us understand how a material behaves under external forces or load, and how they affect its mechanical strength and ability to be molded in suitable shapes. Some of the most representative mechanical properties of a material include the elasticity, stiffness, plasticity, ductility, hardness, flexibility, and toughness.

2.1.1 Tensile Testing

Several experiments can be conducted to define such properties. Perhaps, the most common technique consists in uniaxial tensile testing where a sample is put through controlled tension, being stretched along its long central axis until failure. Figure 2.1 illustrates this technique, by which a couple of measurements can be obtained. One of them is the tensile load F, that divided by the cross-sectional area A of the specimen gives the stress σ that the material sustains along the direction of the applied load:

$$\sigma = \frac{F}{A}. \tag{2.1}$$

Other measurements are the dimensions of the sample (x, y, and z) at different degrees of

elongation with which, if the initial dimensions (x_0, y_0, and z_0) are known, the ratio of the change between the initial and final lengths of the specimen, known as the strain ε, can be calculated:

$$\varepsilon_x = \frac{x - x_0}{x_0}, \qquad (2.2) \qquad \varepsilon_y = \frac{y - y_0}{y_0}, \qquad (2.3) \qquad \varepsilon_z = \frac{z - z_0}{z_0}. \qquad (2.4)$$

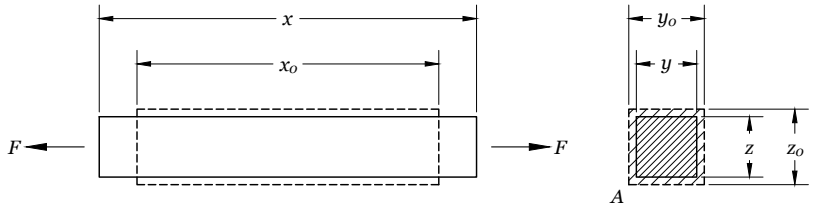

Figure 2.1: Specimen under tensile load. The dashed and continuous lines represent the initial and final dimensions, respectively.

2.1.2 Stress-Strain Curve and Young's Modulus

Knowing the stress needed to reach a certain strain along the direction of the load in a tensile test, the stress-strain curve (SSC) of the analyzed material can be plotted. These graphs provide not only information of how a solid behaves mechanically when strained at a certain axis, but also other specific mechanical properties of that material.

Two kinds of graphs can be obtained: the "engineering" and the "true" SSCs. In the first one, the original cross-sectional area of the specimen is used in equation 2.1, no matter how it changes throughout the straining process. In the second one, however, the instantaneous cross-sectional area at each strain during the test are used to calculate σ. As a result, the "true" curves are usually above the "engineering" ones, specially at higher strains.[9–11]

Figure 2.2 illustrates a generalized SSC of a solid. Five key points of interest (A, B, C, D, and E) and two regions are shown. Each one of theses points represent a limit that the specimen reaches during the straining process. Point A is the proportional limit. Up to this point, the curve has a linear behavior and obeys Hooke's law: the ratio of the stress with the strain results in a proportionality constant which is known as the Young's modulus or modulus of elasticity E. E can also be simply defined as the slope or the first derivative of the linear region that goes up to point A in the SSC. Therefore, the stress σ

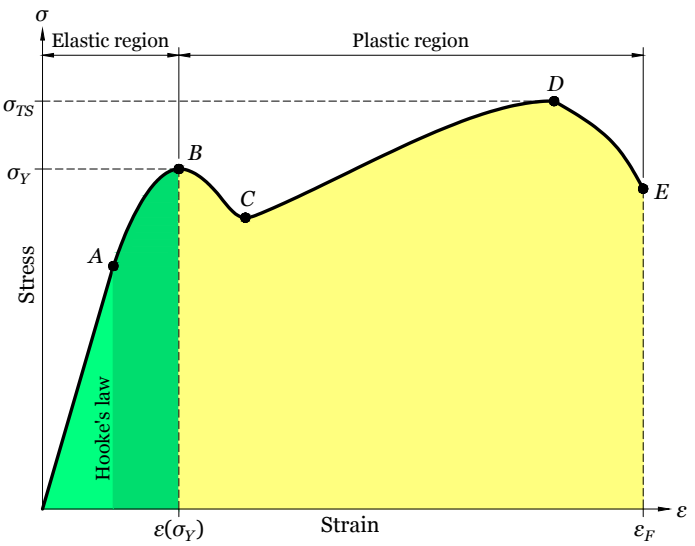

Figure 2.2: Generalized illustration of a stress-strain curve.

can be written as:

$$\sigma = E\varepsilon. \tag{2.5}$$

After this point, if the stretching continues, points B and later C are reached. These are known as the upper and lower yield points, respectively. The yield point is defined as the elastic limit. In other words, before this point the material's SSC is still in the elastic region (green region in the graph portrayed in figure 2.2) at which, if the load is removed completely, the material returns to its original shape. Beyond this limit, if the loading process continues, the material's SSC enters the plastic region (yellow region in the graph portrayed figure 2.2), at which, even if the load is removed entirely, the material is not able to recover its original shape anymore, and plastic deformation takes place. At point B the yield strength σ_Y of the material, which is the maximum stress that the material can handle before it starts behaving plastically, is also defined, as well as the maximum elastic strain $\varepsilon(\sigma_Y)$. Suppose that the load is not removed, eventually the SSC will reach point D, which is a maximum. This is the ultimate stress point that defines the maximum stress σ_{TS} that the material can endure before the failure process begins. After this point, the material starts fracturing until its SSC reaches point E, that is, the fracture or breaking point, where failure occurs after the fracture or final strain ε_F is reached.

Defined the characteristic points of the SSC, as well as the stresses and strains

related to them, the material can be characterized due its mechanical properties as follows:

- **elastic**, if $\varepsilon(\sigma_Y)$ is high;
- **plastic**, if $\varepsilon(\sigma_Y)$ is low;
- **ductile**, if ε_F is high (large plastic region);
- **brittle**, if ε_F is low (small plastic region);
- **stiff**, if σ_Y is high;
- **flexible**, if σ_Y is low;
- **tough**, if σ_{TS} and ε_F are high.

2.1.3 Poisson's Ratio

Besides the SSC and all the information it provides about the mechanical behavior of a material under tensile load, another parameter that can be obtained from a tensile test is the Poisson's ratio (ν), which is the ratio between the transverse and the axial strains:

$$\nu = -\frac{\varepsilon_{transverse}}{\varepsilon_{axial}}. \tag{2.6}$$

In a three-dimensional (3D) system, like the one shown in figure 2.1, where the load is being applied along the x-axis, ε_x is the axial strain, while ε_y and ε_z are the transverse ones. Hence, the y- and z-directions Poisson's ratio (ν_{xy} and ν_{xz}, respectively) can be calculated as:[10]

$$\nu_{xy} = -\frac{\varepsilon_y}{\varepsilon_x}, \tag{2.7}$$

$$\nu_{xz} = -\frac{\varepsilon_z}{\varepsilon_x}. \tag{2.8}$$

Usually, materials will have negative transverse strains because contraction takes place along the transverse axes. That is, taking the system illustrated in figure 2.1 as an example, the initial y- and z-dimensions are larger than the dimensions acquired after stretching starts along the x-axis, and through equations 2.3 and 2.4, negative ε_y and ε_z are obtained. This occurs in conventional materials, and since the Poisson's ratio equation has a negative sign that will multiply the negative sign of the transverse strain, conventional materials have positive ν values. However, it is not the case for all materials, which we discuss in the next subsection.

2.1.4 Auxetic Materials

In contrast to the above, there is a class of materials known to as auxetic materials[4,5,12–21]

where one or both transverse strains, like the axial strain, will also be positive. This means that the material not only expands along the axis of the uniaxial tensile load, but also expands along one or both transverse axes. Consequently, a negative Poisson's ratio (NPR) is observed in these cases.

The importance of auxetic materials originates on the properties they have, which make possible their usage in a large range of potential applications. It has been reported that these materials have good indentation, shear, and fracture resistance. Moreover, they present a synclastic behavior, that is, the ability of a body to form a dome-shaped doubly curvature under deformation. Also, auxetic materials have superior acoustic absorption compared to conventional materials, a variable permeability, as well as a good morphological memory, which is the capacity of a solid to return to its original shape after being subjected to plastic or semi-plastic deformations. All these properties allow such materials to be employed in several applications, like their use as piezoelectric sensors, in biomedical engineering, textiles, and smart filters, as well as in the automotive, aerospace, and military sectors.[12,13]

A couple of examples of materials that present a NPR include borophene,[15] as well as two-dimensional (2D) mono-layered B_4N[16] and $PdSe_2$[17] structures. Also, an auxetic behavior was observed in SiO_2 in the α-cristobalite structure.[18] Moreover, 69% of cubic elemental metals strained along the [1 1 0] direction possesses a NPR.[19] Graphene strained at specific angles,[20] as well as copper (Cu) nanosystems and graphene-copper (G-Cu) nanocomposites,[4,5,21] which are the objects of study of this work, were also found to be auxetic at certain strains. In the next sections an overview on the later three materials is made.

2.2 Graphene

As mentioned in the introduction of this thesis, since its discovery in 2004 by Kostya Novoselov and Andre Geim using mechanical exfoliation of graphite,[1,2] graphene, which consists of a single layer of carbon (C) atoms arranged in a two-dimensional (2D) honeycomb lattice, has been widely studied and amazing properties and potential applications (e.g. use in mobile devices, coating, sensors, aerospace industry, energy storage, building materials) have been revealed. Regarding the mechanical properties, graphene is probably the material that possesses the most astonishing ones being 200 times stronger than steel.[3]

Such exciting mechanical properties can be explained by the strong bonds of the C atoms that compose the graphene lattice. To understand such structure, it is essential to understand the characteristics of elemental C and its 3D allotropes beforehand.

Starting with the element, C has an electronic configuration that can form different types of valence bonds through atomic orbital hybridization to a variety of elements, including other C atoms. With the atomic number 6, the $1s^2$, $2s^2$, $2p_x^1$, and $2p_y^1$ atomic orbitals are occupied by electrons (figure 2.3a[22]) of which only the four outer ones participate in the formation of covalent chemical bonds. Hybrid orbitals can be formed by the promotion of one of the 2s electrons into the empty $2p_z$ orbital.

In diamond, for example, the three 2p levels hybridize with the 2s-energy level providing the formation of four equivalent sp^3-orbitals, as shown in figure 2.3b.[22] An electron occupies each one of them. The overlap of one C atom sp^3-orbitals with the other C atoms sp^3-orbitals forms the 3D diamond structure where the binding energy of the C-C bonds is quite strong, 345 kJ/mol, resulting in the high hardness of the material.

Nonetheless, in graphite the hybridization occurs with only two of the three 2p-orbitals and three sp^2-orbitals form, as illustrated in figure 2.3c.[22] The orientation of these orbitals is perpendicular to the remaining 2p-orbital, which lies symmetrically in the xy plane at 120° angles. This leads to the formation of in-plane covalent sp^2 bonds between carbon atoms, affecting the planar hexagonal honeycomb-like structure of graphite. These in-plane σ-bonds form each of the in-plane graphite layers, and each one of them is a graphene sheet. Such C-C bonds in graphene have a binding energy of 615 kJ/mol, being significantly stronger than the C-C bonds in sp^3-hybridized diamond. In contrast, the inter-plane π-bonds that are formed by the remaining 2p-orbitals have a much lower binding

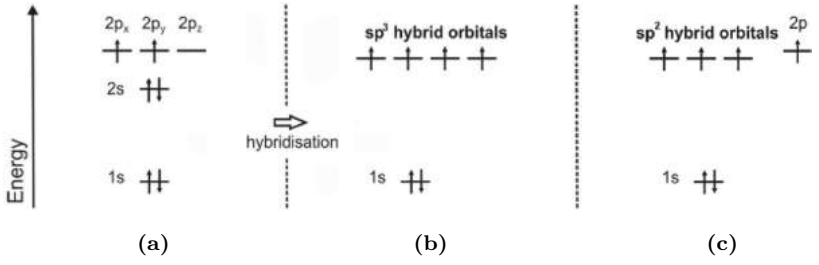

Figure 2.3: Orbital diagram of a C atom. Four electrons in the doubly occupied 2s-orbital and the half occupied 2p-orbitals participate in the chemical bonding of C. In (a), the ground state is represented. In (b), sp^3-hybridized as in diamond is shown. Finally, in (c), sp^2-hybridized as in graphite and graphene is illustrated.

energy, which explains the easy shearing of graphite along the layer plane. The lattice constant of single layers of graphite or, as mentioned before, the graphene layers, is equal to $\sqrt{3}a_0$, where a_0 is the bond-length between two C atoms and equals 1.42 Å. In figure 2.4, the graphene hexagonal lattice is illustrated, and the two possible edges, armchair (AC) and zigzag (ZZ), are highlighted in green and blue, respectively. The unit cell is also highlighted in gray.[22,23]

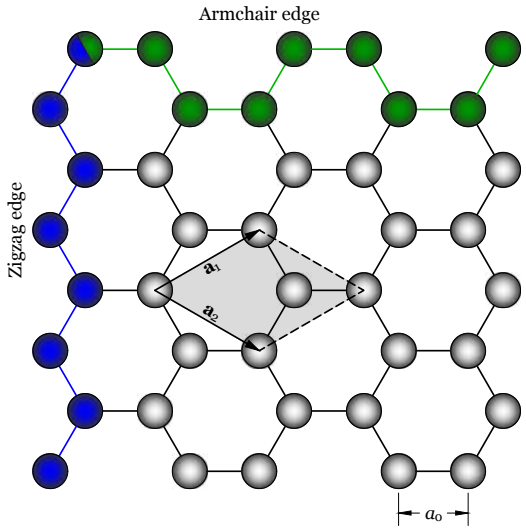

Figure 2.4: Graphene structure. Each sphere and continuous line represents a C atom and a C-C bond, respectively. The highlighted in green atoms and bonds illustrate the armchair (AC) edge of graphene while the highlighted in blue ones represent the zigzag (ZZ) edge. The arrows are the basis vectors $\mathbf{a}_1$ and $\mathbf{a}_2$ of the unit cell, which is highlighted in gray. $\mathbf{a}_1$ and $\mathbf{a}_2$ form a 60° angle at their origin. The bond length a_0 is 1.42 Å.

2.2.1 Mechanical Behavior of Graphene

A study carried out on individual graphene sheets by Lee *et al.*[3] in 2007 where mechanical properties were measured by atomic force microscope (AFM) nanoindentation, showed that a mono-layered pristine graphene can achieve a stiffness, or Young's modulus E, and a yield strength σ_Y of about 1 TPa and 130 GPa, respectively. Such results are supported by theoretical studies done by density functional theory (DFT) calculations[24–26] and molecular dynamics (MD) simulations[6,7,27–37] of graphene nanosystems that confirm the high stiffness and strength of the 2D material.

Nevertheless, E as well as σ_Y and σ_{TS} of graphene nanosystems may vary a little depending on the methodology used to make the measurements and on other factors, such as

temperature,[33] size,[30] and chirality along the uniaxial tensile load direction,[6,30–34] that is, if the load is applied throughout the AC or ZZ edges. Regarding temperature, a decrease on these characteristics is observed when it increases, as one should expect. As for the size, a slight increment on E is shown on larger systems. This increment tends to reach a constant value when the length of the graphene nanoribbon (GNR) is 15 nm or longer. Finally, graphene strained along the AC edge is stiffer than graphene strained along the ZZ edge. However, ZZ graphene is more elastic. Though, in almost all cases, E and σ_Y do not vary significantly. E stays around 1 TPa, and σ_Y does not go too far from the 130 GPa value measured by Lee *et al.*

Another interesting fact about the mechanical behavior of graphene is the form of its SSC. Initially, it does not present a linear region, as discussed in subsection 2.1.2. Instead, a curve is formed since the beginning, as shown in figure 3.8c. Consequently, the approach to estimate E of graphene is done by curve fitting and not by linear fitting to find the slope as mentioned in subsection 2.1.2. This approach will be discussed with more details in section 3.8.

Another factor that plays an important role in the mechanical behavior of graphene is the presence of defects. In the next subsection we discuss about these defects and the effect they have on the mechanical properties of graphene based on previous results.

2.2.2 Defects in Graphene

Graphene, just like any other material, can present several defects in its structure which may appear during growth or be induced by some techniques, such as electron and ion irradiation.[38,39] These defects can be either zero-dimensional, e.g., single- and multi-vacancies, pentagon-heptagon (5-7-7-5) Stone-Wales (SW) pairs, carbon and foreign adatoms, and substitutional impurities; or one-dimensional, e.g., dislocations and edge defects.[40,41] In this work, the focus is set on the vacancy and on the pentagon-heptagon SW defect types, and the role they have on the mechanical properties of graphene nanosheets and on the G-Cu heterostructure is studied.

A single vacancy (SV), which consists of a missing atom in the lattice, is the simplest defect in any material. In graphene and graphite, such imperfection could be observed by scanning tunneling microscopy (STM)[42] and transmission electron microscopy (TEM).[43,44] When a SV is created, three bonds are lost but, for geometrical reasons, a

bond can be formed causing the origination of five-membered and nine-membered rings with sp-sp^2 C-C bonds, each C atom having two or three neighbors,[45] as seen in figure 2.5a. The formation energy E_f of such defect is considerably high when compared to other materials due to the presence of an under-coordinated C atom. A value of $E_f \approx 7.5$ eV have been found from DFT calculations[46,47] and $E_f = 8$ eV from *ab initio* calculations.[48] For the situation where two neighboring atoms are missing or two SVs are coalesced, a double vacancy (DV) is created (figure 2.5b). DVs are favored over SVs due to their lower E_f per missing atom (4 eV, 8 eV in total).[46,47] In this case, two pentagons and one hectagon appear in a more coherent network when compared to SVs. Consequently, there are fewer bond length perturbations around the defect resulting in a more thermodynamically favored setting. More complex types of vacancies can appear when more than two neighboring atoms are missing in the lattice.[40]

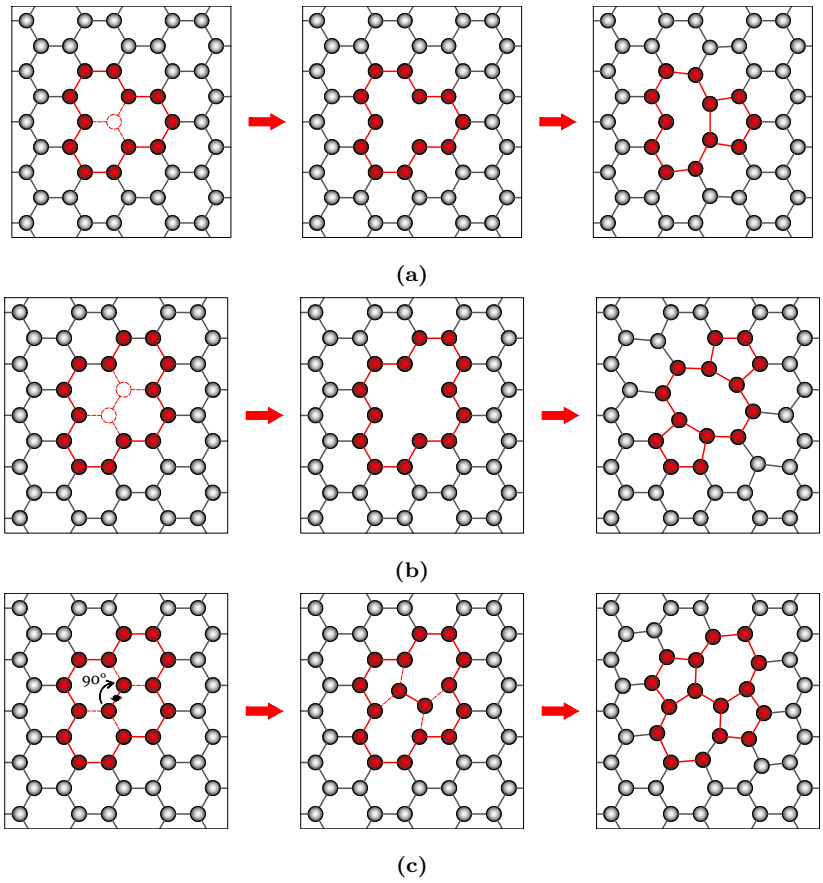

Figure 2.5: Formation scheme of (a) a SV, (b) a DV, and (c) a 5-7-7-5 SW defect.

As for the 5-7-7-5 SW pairs defect,[49] no atom removal is needed. This imperfection is among the simplest and more easily fabricated. It requires bond-breaking and bond-reform to take place, transforming sp^2 bonds and emerging through the conversion of four hexagons into two pentagons and two heptagons by a 90° rotation of one of the C-C bonds (figure 2.5c).[45,50] From *ab initio* calculations, the formation energy of such defects was found to be $E_f = 4.8$ eV. However, there is a substantial 9.2 eV energy barrier to its development, which corresponds to the 45° rotation that a C-C bond has to undergo before completing the 90° rotation and achieve the 4.8 eV minimum. The same energy barrier has to be surpassed to obtain a pristine lattice again.[48]

Such defects, as expected, will affect the mechanical properties of graphene. Different studies[6,7,33–37] on defective nanoribbons have shown a decrease in the E value of pristine systems, this decrease being more significant when vacancies are present. SW defects, on the other hand, do not affect substantially the Young's moduli of GNRs. Since no C-C bonds are technically lost during the formation of a SW defect, unlike SVs or DVs, the material is still able to support almost the same amount of load as its pristine counterpart. A decrease in σ_{TS} has also been observed when defects are present, the pattern being the same as the one of E: vacancies make the material more sensible to this change than SW defects. Also, the higher the concentration of defects, the more sensible the material is to a decrease in these parameters. Even though defects worsen to some extent the mechanical properties of graphene, the defective systems still present high performance under mechanical strain.

These good mechanical properties allows the exploration of graphene as a reinforcement in other materials, e.g. metals like Cu. The strengthening mechanism of nanolayered G-Cu nanocomposites was studied by Zhang *et al.*,[4,5] and the effect that temperature has on the mechanical properties of these nanosystems was studied by Fan *et al.*[21] In the present work, vacancies and SW defects are introduced in the graphene layer of these heterostructures and the role they play in the mechanical properties is investigated. But first, we overview the other material that composes the G-Cu nanocomposite: Cu.

2.3 Copper

One of the most common metals used in everyday life nowadays is Cu, material that stands out by unique properties that make it one of the best materials in engineering for bearing

applications: it is the material most used in telecommunication and electrical cables due to its high electrical conductivity. Other properties that make it stand out are high thermal conductivity, excellent corrosion and resistance at different environments and weather conditions, and, focusing in the mechanical properties which are the subject of research in this work, high ductility and toughness over a broad range of temperatures.

Belonging to group 11 in the periodic table, like the elements silver (Ag) and gold (Au), Cu shares many similarities with them, including the face-centered cubic (FCC) structure,[51] at which Cu atoms are arranged in an unit cell, as shown in figure 2.6. Here, the lattice parameter a is 3.62 Å and the interatomic distance is 2.553 Å.

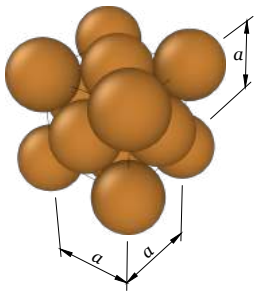

Figure 2.6: Cu FCC unit cell. Each sphere represents a Cu atom. a is the lattice parameter and equals to 3.62 Å.

2.3.1 Mechanical Behavior of Copper

The FCC structure is what provides the high ductility and toughness of Cu due to a mechanism known as slip. In this mechanism, the atoms slide past one another in groups when a force is applied. This movement occurs preferentially in any or all of three directions along a specific geometric plane of atoms within the FCC cell. There are four of such planes in such structure, and since the movement can occur in three directions, there are twelve chances of slippage to occur (see figure 2.7[52]), which is the maximum number of slip possibilities in any metal structure. Consequently, since Cu is very likely to experience substantial slip, it tends to deform rather than fracture and fail leading to excellent ductility and toughness that make it creep and resistant to fatigue. Furthermore, Cu is not affected by embrittlement at low temperatures.[53]

Experimentally, the mechanical properties of Cu nanocrystalline disks,[54] thin films,[55,56] and rods[57] have been measured through tensile testing techniques. There is some disparity between the values found for E in each case, going from 104 to 131 GPa for

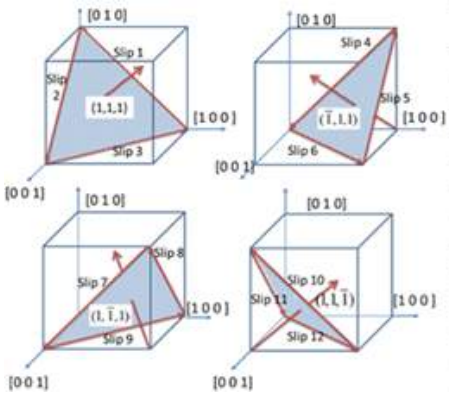

Slip system	Slip plane normal	Slip direction
1	(1,1,1)	[1, 1̄, 0]
2	(1,1,1)	[0,1, 1̄]
3	(1,1,1)	[1,0, 1̄]
4	(1̄,1,1)	[1,1,0]
5	(1̄,1,1)	[0,1, 1̄]
6	(1̄,1,1)	[1,0,1]
7	(1, 1̄,1)	[1,1,0]
8	(1, 1̄,1)	[0,1,1]
9	(1, 1̄,1)	[1,0, 1̄]
10	(1,1, 1̄)	[1, 1̄,0]
11	(1,1, 1̄)	[0,1,1]
12	(1,1, 1̄)	[1,0,1]

Figure 2.7: On the left side, a schematic illustration of the FCC slip directions and normals. On the right side, all twelve possibilities for the occurrence of slip are listed.

nanocrystalline disks and from 70.7 to 108.8 GPa for thin films. A value of 130 GPa, also for thin films, is given in Freund and Suresh's book.[58] The same authors give a value of 0.34 for the Poisson's ratio ν of Cu thin films, which is in good agreement with references 54 and 55. Though, ν values of Cu can vary depending on the crystallographic direction it is being stretched, with negative values being common along the [1 1 0] and [1 $\bar{1}$ 0] crystal orientations.[21] Disparities in the values of σ_Y and σ_{TS} are also present depending on the reference.

Theoretically, MD studies on the mechanical properties of Cu nanosystems have also been done. It was observed, through the published SSCs, that E and σ_Y of Cu nanowires (Cu-NWs) depend on temperature and the crystallographic direction in which the uniaxial tensile load is applied.[59,60] An increment on E and σ_Y is noticed at lower temperatures and, regarding the crystallographic direction, the highest E is found when the Cu-NW is stretched along the [1 1 1] direction (137.58 GPa at room temperature) and the lowest when it is strained along the [1 0 0] direction (80.04 GPa at room temperature). The dependence on the strain rate was also investigated.[60] It was observed that the faster the material is strained, the higher σ_Y is. Nonetheless, E is independent from this parameter. Another MD study showed some dependence on the thickness of Cu nanofilms deposited on substrates.[61] Thicker films presented slight lower E and σ_Y than thinner ones due to the ratio between the number of layers of Cu atoms and the rigid substrate layer. Although, according to the authors, films thicker than 10 nm are practically thickness independent and present the characteristic mechanical properties of 2D free Cu structures. The opposite

occurs when the Cu nanofilm has free surfaces though, as studied by Zhang *et al.*: thinner films present lower E and σ_Y values than thicker ones.[5]

The mechanical response of Cu nanofilms under tensile load can be enhanced by the introduction of graphene, which exceptional mechanical properties have been discussed already. We overview these G-Cu nanocomposites in the following section.

2.4 Graphene-Copper Nanocomposites

As discussed in the previous section, Cu has exceptional mechanical properties. However, there could be cases where a strengthening of the material is needed. One way to acquire that is to make Cu-composites adding stiffer materials, e.g. graphene, to the Cu matrix.

Some interest has already been shown in such composite, it being, therefore, grown experimentally,[62–65] and theoretically analyzed through MD simulations.[4,5,21]

In experiments, bulk G-Cu composites were assembled and the mechanical properties measured. In reference 62, using a double cantilever beam (DCB), the adhesion energy between graphene and Cu was measured to study the strengthening mechanism. Here, the composite was actually fabricated with graphene oxide (GO) containing 2.5 vol%. Various GO nanosheets were dispersed inside a Cu matrix. In references 63, 64, and 65, tensile tests were carried out on universal testing machines. In the first study, the authors compare the strengthening mechanism of G-Cu composites made with GO and pristine graphene (PG) at a 0.3 wt.% content also dispersed in Cu. In the second one, Cu submicron flakes coated with *in situ* catalytic grown graphene were used as blocks to fabricate a bulk G-Cu nanolaminated structure via a bottom-up assembly process. The graphene contents analyzed were 1.6 and 2.5 vol% of the total composite volume. Finally, in the third study, G-Cu composites with 0.1 to 3 wt.% of carbon phase additive were obtained from Cu powder and thermally expanded graphite (TEG). The precursors were mixed an the specimens fabricated by modified powder metallurgy technique.[66]

The results of the references mentioned above show an increment in the stiffness of Cu as well as in σ_Y when graphene is added. Composites containing a higher proportion of graphene in volume or weight are stiffer. E values of 127 and 135 GPa were reported for 1.6 and 2.5 vol% G-Cu composites, respectively, while 108 GPa was reported for unreinforced Cu.[64] On the other hand, analyzing the published SSCs, it can also be observed that, even though there is an increase in stiffness, G-Cu is less ductile than pure Cu, reaching its ε_F

at earlier values. It is also less elastic, reaching its $\varepsilon(\sigma_Y)$ also earlier.

It should be noted that in the studies carried out with MD simulations, the tendency is the same. The analysis made in sandwich-like G-Cu heterostructures where one or more graphene sheets are introduced between Cu films perpendicularly to the thickness direction also showed higher stiffness and σ_Y values as well as an embrittlement effect. The volume fraction of graphene plays an important role as well, the higher it is the more these effects are enhanced.[4,5,21] In reference 21 the temperature effect is also investigated. Higher temperatures cause a decrease in E values of the G-Cu heterostructure. Another interesting finding of these studies is that G-Cu nanocomposites present simultaneously positive Poisson's ratio (PPR) and NPR. The NPR comes as a result of surface effect in the G-Cu interface.

The surface effect originates as a consequence of the free surfaces in nanosystems. During a tensile test, if the specimen is being strained along the x-axis, for example, this effect can be seen through the stress per atom ($\boldsymbol{\sigma}^{\alpha}$) distribution along the y and z directions, which corresponds to the σ^{α}_{yy} and σ^{α}_{zz} components. The atoms that compound the free surfaces tend to present considerably higher σ^{α}_{yy} and σ^{α}_{zz} values than inner atoms. However, since the uniaxial tensile load is applied along the x-direction, the total stress along the y- and z-directions (σ_{yy} and σ_{zz}, respectively) should be near zero. Therefore, σ^{α}_{yy} and σ^{α}_{zz} values of inner atoms have to be at significantly lower levels to compensate the high σ^{α}_{yy} and σ^{α}_{zz} values of the surface atoms.

Nevertheless, when graphene is introduced between two Cu layers in the xz-plane, that is, perpendicularly to the thickness direction, Cu atoms on the graphene-Cu interface also present high σ^{α}_{yy} and σ^{α}_{zz} values. This interface can be interpreted as a new free boundary. Such stress concentration on the interface added up to the stress concentration on the outside free surfaces implies that stresses on inner atoms have to become lower for compensation. σ^{α}_{zz} even reaches negative values, which means that these atoms are under compression along the z-axis. Consequently, the compression along the z-direction induces a NPR in the y-direction as a result of a smooth branching of the transverse lattice parameters, even though the specimen is being strained along a crystallographic direction pure Cu is not auxetic ([1 0 0]).[5] This branching effect has been revealed by Ho *et al.*[67] For a better visualization of the surface effect in a Cu nanofilm and a G-Cu nanocomposite of comparable sizes, see figure 2.8, which was taken from reference 4.

The NPR effect is also found in reference 21, but here the load is applied along a

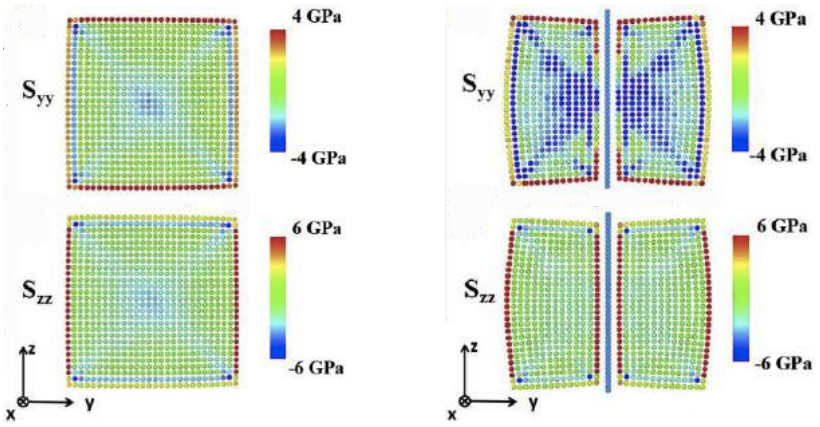

Figure 2.8: Atomic stress distribution at a selected central slice in the yz-plane and a $\varepsilon_x^s = 0.0713$ of (a) pure Cu nanofilm and (b) G-Cu nanocomposite of comparable sizes. Note that higher stresses are reached on the surfaces in both cases and how the G-Cu interface in the nanocomposite creates new free boundaries where higher stresses, specially σ_{zz}^{α}, are also reached on Cu atoms. Inner Cu atoms sustain lower stresses to compensate. In this work, S_{yy} and S_{zz} correspond to σ_{yy}^{α} and σ_{zz}^{α}, respectively.

crystallographic orientation where Cu itself is auxetic, it actually showing a lower ν value than the G-Cu composite.

Therefore, it can be concluded that graphene strengthens Cu making it stiffer and increasing its σ_Y. That could be a key feature to fabricate telecommunication cables that will be submerged deep in the ocean where extreme loads or shocks are present. The simultaneous appearance of a PPR and a NPR in G-Cu composites would also allow the dimensions of these cables to remain almost unchanged under high-pressure. Another potential application of such composite prospects in scaffold design, where tuning the magnitude and polarity of ν in tissue engineering is necessary.[5]

As far as we know, though, a study on the mechanical properties of these structures with a defective graphene layer have not been done yet. Thus, in this work we study the role that defects play in the mechanical properties of G-Cu heterostructures by introducing vacancies and SW defects in the graphene layer at different densities.

In the next chapter, we detail the MD simulation methodology as well as further information of our analysis.

Chapter 3

Methodology: Molecular Dynamics Simulation

In modern days, microscopic analysis methods are essential to generate and to study materials and their physical phenomena at a molecular or atomic level. In order to accomplish that, the use of computational simulation tools is necessary since, in a real system, there are numerous particles interacting with one another, and a simple mathematical analysis with pencil and paper becomes something infeasible.[68] One of the main computational simulation techniques is the molecular dynamics (MD) method, which is, in so many ways, very similar to real life experiments. Here, the steps taken also go from preparing a sample to the measurement of the properties of interest and their analysis.[69]

In MD the motion of the particles is computationally simulated according to Newton's equations of motion, and the interaction between these particles is governed by a potential, which is the most important part of a simulation since it must describe properly, not just the microscopic properties of the system, but also its macroscopic ones.[70]

3.1 Newton's Equation of Motion

The motion of a particle, as mentioned in the introduction of this chapter, is described by Newton's equation of motion:

$$m\ddot{\mathbf{r}} = m\mathbf{a} = \mathbf{f}, \tag{3.1}$$

where m is the particle's mass. Here $\mathbf{r}$, $\mathbf{f}$, and $\mathbf{a}$ represent a notation for the x, y, and z

components of the particle position, force, and acceleration, respectively. The force $\mathbf{f}$ on the particle is due to the ambient particles, and they interact via a potential U. Moreover, it is known, from theoretical mechanics, that $\mathbf{f}$ can be written as:[68,71]

$$\mathbf{f} = -\frac{\partial U}{\partial \mathbf{r}}. \tag{3.2}$$

It can also be noted that there will be N sets of equations similar to equation 3.1 for a system composed of N particles.

3.2 The Velocity Verlet Method

Once the interaction potential is defined, the Newton's equation of motion is solved by the implementation of an integration algorithm. One of the most commonly used method is that adopted by Verlet,[72] which is based on the particle's accelerations $\mathbf{a}(t)$ and positions $\mathbf{r}(t)$ at a time t, and the positions $\mathbf{r}(t-\delta t)$ from the previous step. δt is the time step. This method comes from the approximation of the second-order differential term in equation 3.1 to an algebraic expression using a Taylor series expansion:[68,71]

$$\mathbf{r}(t+\delta t) = \mathbf{r}(t) + \delta t\frac{d\mathbf{r}(t)}{dt} + \frac{1}{2!}\delta t^2\frac{d^2\mathbf{r}(t)}{dt^2} + \frac{1}{3!}\delta t^3\frac{d^3\mathbf{r}(t)}{dt^3} + ..., \tag{3.3}$$

where the higher-order differential terms can be neglected if $\mathbf{r}$ does not change significantly with time. Additionally, the approximation of the second-order differential term in equation 3.1 as an algebraic expression needs another form of the Taylor expansion:

$$\mathbf{r}(t-\delta t) = \mathbf{r}(t) - \delta t\frac{d\mathbf{r}(t)}{dt} + \frac{1}{2!}\delta t^2\frac{d^2\mathbf{r}(t)}{dt^2} - \frac{1}{3!}\delta t^3\frac{d^3\mathbf{r}(t)}{dt^3} + ..., \tag{3.4}$$

Thereby, with equations 3.3 and 3.4, the second-order differential term can be solved as:

$$\frac{d^2\mathbf{r}(t)}{dt^2} = \frac{\mathbf{r}(t+\delta t) - 2\mathbf{r}(t) + \mathbf{r}(t-\delta t)}{\delta t^2}, \tag{3.5}$$

and Newton's equation of motion can be rewritten as:

$$\mathbf{r}(t+\delta t) = 2\mathbf{r}(t) - \mathbf{r}(t-\delta t) + \frac{\delta t^2}{m}\mathbf{f}(t) = 2\mathbf{r}(t) - \mathbf{r}(t-\delta t) + \delta t^2\mathbf{a}(t). \tag{3.6}$$

Note that there are not velocity terms in equation 3.6 to determine the particle's position at a given step, and this is the principle of the Verlet method.[72] However, if the

velocities are required (e.g., to estimate the kinetic energy), they can be obtained from the central difference approximation as:

$$\mathbf{v}(t) = \frac{\mathbf{r}(t+\delta t) - \mathbf{r}(t-\delta t)}{2\delta t}. \tag{3.7}$$

Nonetheless, in cases where it is desirable to keep the temperature of the system constant, the simultaneous use of positions and velocities will be more appropriate. In those situations, the velocity Verlet method is the one that should be implemented. It is well known that the first- and second-order differentials of the position are the velocity and the acceleration, respectively. Thus, neglecting the differential terms higher than second-order in equation 3.3, the following expression can be obtained:

$$\mathbf{r}(t+\delta t) = \mathbf{r}(t) + \mathbf{v}(t)\delta t + \frac{\delta t^2}{2}\mathbf{a}(t), \tag{3.8}$$

and since the first-order differential of the velocity is the acceleration, it can be specified as:

$$\mathbf{v}(t+\delta t) = \mathbf{v}(t) + \mathbf{a}(t)\delta t. \tag{3.9}$$

In order to achieve more accuracy, the acceleration term in equation 3.9 can be slightly adjusted:

$$\mathbf{v}(t+\delta t) = \mathbf{v}(t) + \frac{\delta t}{2}\left(\mathbf{a}(t) + \mathbf{a}(t+\delta t)\right). \tag{3.10}$$

The velocity Verlet method conducts a MD simulation accordingly to the steps shown in figure 3.1. In this MD scheme, at every time step δt, the position and velocity of all particles are evaluated.[68]

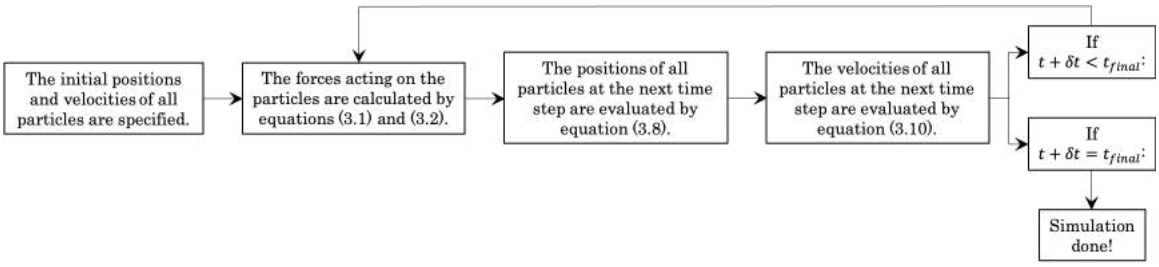

Figure 3.1: General scheme of how a MD simulation is ran.

In order to implement the velocity Verlet simulation algorithm, a simulation code is needed. In this work, the Large-scale Atomic/Molecular Massively Parallel Simulator (LAMMPS),[73,74] which is a classical MD code with a focus on condensed-matter modeling, is used. For a detailed description, see cited reference.

3.3 Temperature Control

By the implementation of a thermostat, the temperature T of a system of atoms, which is the average of the kinetic energies of all particles, can be controlled. T can be given as:

$$T = \frac{1}{N_f k_B} \sum_{i,\alpha} m^\alpha (v_i^\alpha)^2, \tag{3.11}$$

where, N_f is the total number of translational degrees of freedom of the system, k_B is the Boltzmann constant, and v_i^α is the velocity of atom α in the i direction. Depending on the dimensionality of the system, i can take 1, 2 or 3 values.

The thermostat works by scaling the velocity of particles since it is the only variable that T depends on, as shown in equation 3.11. Nevertheless, only the average value of temperature can be kept constant during a simulation as the fluctuations of velocities make it impossible to maintain the temperature at a fixed value.

In this study, the Nosé-Hoover thermostat[75,76] is applied. This thermostat modifies the equation of motion by the use of a friction factor (μ), which is defined as:

$$\frac{d\mu(t)}{dt} = \frac{N_f k_B}{Q} \left(T(t) - T_0\right) \tag{3.12}$$

where T and T_0 are the current and desired temperatures, respectively, and Q is the thermostat effective mass. Q determines the strength of the thermostat, and is represented as:

$$Q = N_f k_B T_0 \tau_T^2, \tag{3.13}$$

where τ_T is the specified time constant for temperature fluctuations and it is generally of the order of a hundred time steps to achieve smooth temperature transitions.

Thus, the modified Newton's equation of motion is:[77]

$$\mathbf{a} = \frac{\mathbf{f}(t)}{m^\alpha} - \mu(t)\mathbf{v}(t). \tag{3.14}$$

3.4 Pressure Control

In MD simulations, in order to control the pressure of a system of atoms (P_{ij}^V) a barostat must be employed. P_{ij}^V is defined as:

$$P_{ij}^V = \frac{1}{V} \sum_\alpha \left[\sum_{\beta=1}^{N} \left(r_i^\beta - r_i^\alpha \right) f_j^{\alpha\beta} + m^\alpha v_i^\alpha v_j^\alpha \right], \tag{3.15}$$

where V is the total volume of the system; i and j are the directional indices; β labels the neighboring atoms that goes from 1 to N; r_i^α and r_i^β are the positions of atoms α and β along the i direction, respectively; $f_j^{\alpha\beta}$ is the force along the j direction; and m^α and v^α are the mass and velocity of atom α, respectively. At every step where the simulation box dimensions change, the system pressure is adjusted.

The Nosé-Hoover barostat is commonly used in LAMMPS. It has a volume scaling factor (η) defined by:

$$\frac{d\eta(t)}{dt} = \frac{1}{N_f k_B T_0 \tau_P^2} V(t) \left(P(t) - P_0\right), \tag{3.16}$$

where T_0 and P_0 are instantaneous temperature and pressure, respectively; $P(t)$ is the desired pressure; and τ_P is the specified time constant for pressure fluctuations, which is generally of the order of a thousand time steps to achieve a smooth pressure fluctuation. Also, the volume of the system can be adjusted using η:[77]

$$\frac{dV(t)}{dt} = 3\eta(t)V(t). \tag{3.17}$$

3.5 Simulation Details

3.5.1 Initial Data

In MD, as shown in figure 3.1, the first step of the method is the specification of the initial positions of all particles in the system, which is, obviously, an indispensable procedure. These initial positions can be set randomly inside a simulation region, although a regular configuration, such as the lattice structure of the material under analysis, is a more straightforward manner.[68]

In this work, three different materials were studied: graphene nanosheets, which have a honeycomb lattice, in both AC and ZZ chiralities (figures 3.2a and 3.2b, respectively); a Cu nanofilm (figure 3.2c), which has a face-centered cubic (FCC) lattice; and G-Cu heterostructures, which consist of the same Cu nanofilm, but with the introduction of one of the graphene nanosheets in the middle, separating it in two symmetric nanofilms (figure 3.2d). The Cu nanofilm under analysis was the size of $47a$, $8a$, and $32a$ along the x, y, and z axes, respectively, a being the lattice parameter of Cu (a = 3.61 Å). Also, it was oriented in the [1 0 0], [0 1 0], and [0 0 1] crystallographic directions along the x, y, and z axes, respectively. The graphene nanosheets take similar dimensions to those of Cu in x and z in order for it to fit well between the upper and lower $4a$-thick Cu layers in the G-Cu

heterostructure. A system of the same size was, as well, studied by Zhang et al.[5] Also, the separation between the graphene nanosheet and both Cu layers was set as 3.225 Å, which is the size cross Lennard-Jones parameter (σ^{CCu}) for C and Cu,[78] in other words, how close two non-bonding C and Cu atoms can get (van der Waals radius).

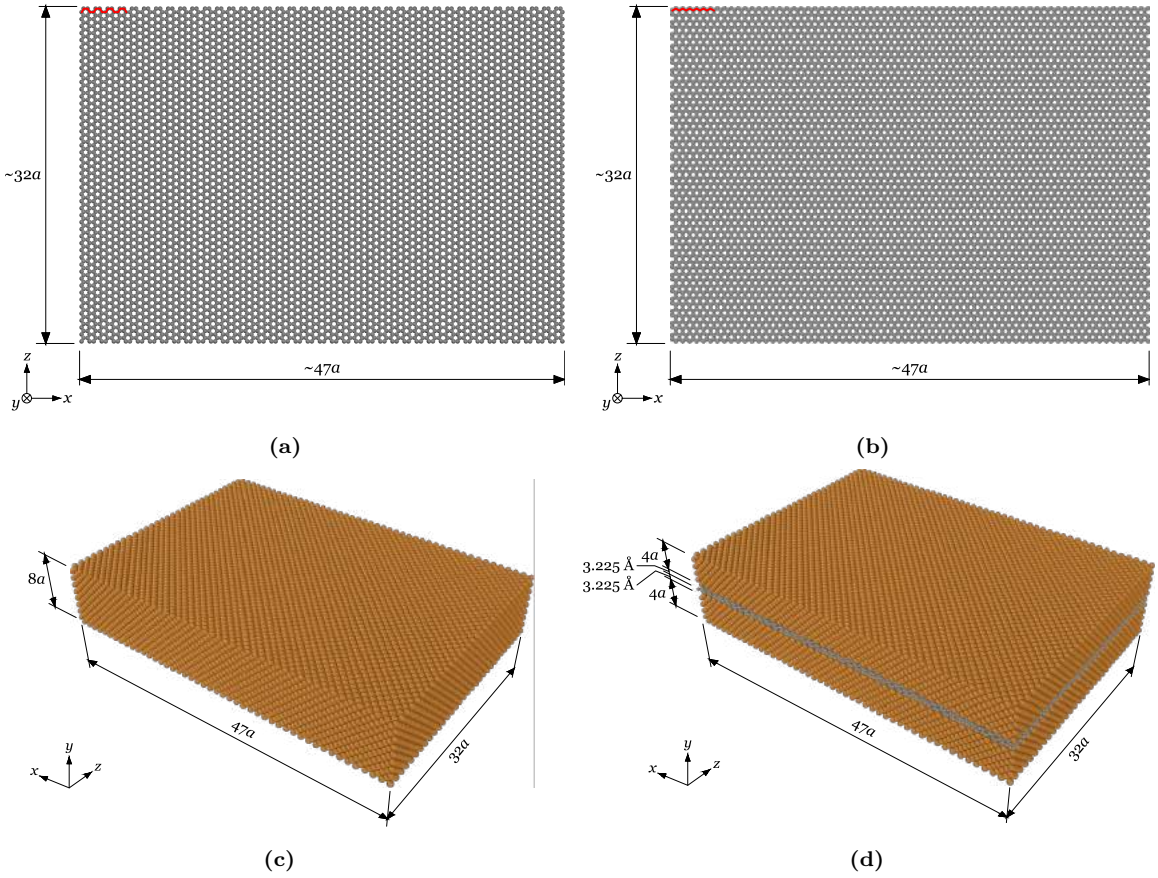

Figure 3.2: Representation of the (a) AC graphene, (b) ZZ graphene, (c) pure Cu, and (d) G-Cu nanosystems.

Moreover, vacancies and SW defects at different densities were randomly introduced in graphene to investigate the effect they have in the mechanical properties of the AC and ZZ nanosheets and G-Cu heterostructures. Both defects were analyzed separately: the defective systems had only one or another. The density of vacancies (ρ_{Vac}) and SW defects (ρ_{SW}) are defined as follows:

$$\rho_{Vac} = \frac{n_{Vac}}{n_{At} + n_{Vac}}, \qquad (3.18) \qquad\qquad \rho_{SW} = \frac{2n_{SW}}{n_{At}}, \qquad (3.19)$$

where n_{At}, n_{Vac}, and n_{SW} are the number of atoms, vacancies, and SW defects present

in graphene, respectively. The factor "2" in equation 3.19 appears because it takes two C atoms to form a SW defect when they change their position in the lattice by a 90° rotation of their bond, as described in subsection 2.2.2.

3.5.2 Boundary Conditions

In MD all the particles are positioned into a simulation box, which delimits the boundaries of the system to be studied. The conditions of these boundaries have to be set before starting a simulation. In LAMMPS, four boundary conditions can be chosen: periodic (p), non-periodic and fixed (f), non-periodic and shrink-wrapped (s), and non-periodic and shrink-wrapped with a minimum value (m).[74]

A p style means that particles interact across the boundary, and they can exit one end of the box and re-enter it through the other.[74] In other words, there is a continuity of the simulation space (figure 3.3[68]). This type of boundary conditions can be a very useful tool because it permits the simulation of infinitely extensive systems, and results that describe the behavior of a bulk material can be obtained reproducing experimental data accurately.[68] Also, surface effects can be avoided.

In the remaining boundary conditions there is no continuity of the simulation region and surface effects are captured. They differ between them in the aspect that, in

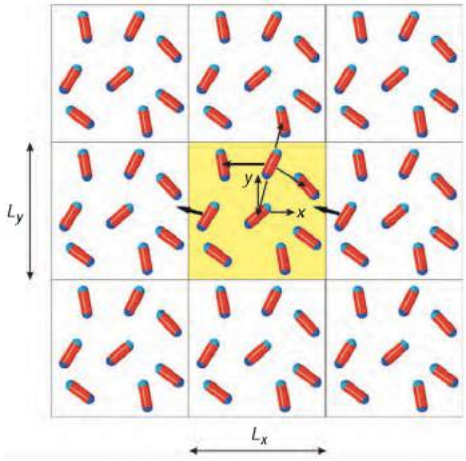

Figure 3.3: Periodic boundary condition in a two-dimensional system composed of spherocylinder particles. The central square is the simulation region, and the surrounding squares are virtual simulation boxes that replicate the main one. The center of the simulation region is the origin of the xy-coordinate system, and its dimensions are L_x and L_y. A particle exiting the left boundary and entering the right one is shown, as indicated by the thick arrows.

the *f* style, the face position is fixed, and if an atom moves outside of the box, it will be deleted, meanwhile, in the *s* style, the atoms are encompassed in the face of the direction it is set no matter how far they move, and in the *m* style, shrink-wrapping occurs, but it is bounded by an specified value in which the face will always be positioned at or above, even if the maximum extent of the particles becomes less than it.[74]

In this work, the boundary conditions were set as *p* in the direction of the uniaxial tensile load (*x*-axis), and as *s* in the perpendicular directions (*y* and *z* axes) for all analyzed systems. Such configurations emulate nanowires with rectangular cross-sectional areas.

3.5.3 Interaction Potential Implementation

The interaction potential is, perhaps, the most important part of a simulation since it has to describe in a proper way the properties of the system. As mentioned in subsection 3.5.1, two different atoms, C and Cu, make up all the nanostructures analyzed in this work. Hence, three different potentials were needed to conduct the interaction between all of them. For the interactions between C atoms in graphene, an adaptive intermolecular reactive empirical bond-order (AIREBO) potential[79] was used. The interactions between Cu atoms were governed by an embedded-atom method (EAM).[80] Finally, the interactions between C and Cu atoms were described by a Lennard-Jones (LJ) potential.[81] Brief descriptions of these potentials are given bellow.

The Adaptive Intermolecular Reactive Empirical Bond-Order Potential

This potential is based on the reactive empirical bond-order (REBO) potential developed by Brenner[82–84] with the introduction of non-bonded interactions through an adaptive treatment of the intermolecular interactions. The AIREBO potential can be described as a sum over pairwise interactions:

$$U_{AIREBO} = \frac{1}{2}\sum_{\alpha}\sum_{\alpha\neq\beta}\left(U^{\alpha\beta}_{REBO} + U^{\alpha\beta}_{LJ} + \sum_{\gamma\neq\alpha,\beta}\sum_{\delta\neq\alpha,\beta,\gamma} U^{\gamma\alpha\beta\delta}_{torsion}\right). \tag{3.20}$$

$U^{\alpha\beta}_{REBO}$ is Brenner's REBO potential, which represents interactions of two atoms separated by a distance less than a covalent-bonding cutoff of $r^{\alpha\beta}_{max}$. It is exclusively short-ranged. For C-C bonds, $r^{\alpha\beta}_{max} = 2.0$ Å. $U^{\alpha\beta}_{REBO}$ has the following form:

$$U^{\alpha\beta}_{REBO} = U^{\alpha\beta}_{R}(r^{\alpha\beta}) + b^{\alpha\beta}U^{\alpha\beta}_{A}(r^{\alpha\beta}), \tag{3.21}$$

where $U_R^{\alpha\beta}$ and $U_A^{\alpha\beta}$ are the repulsive and attractive pairwise potentials determined by atoms α and β. They depend only on the distance $r_{max}^{\alpha\beta}$. $b^{\alpha\beta}$ is a many-body term that brings a dependency on the position and chemical identity of the atoms close to the α-β bond.

Since the REBO potential describes only intramolecular interactions, it does not include any mechanism that treats intermolecular interactions. Therefore, the $U_{LJ}^{\alpha\beta}$ term is added in the AIREBO potential to solve this issue. It has the form of a 12-6 LJ potential, which will be detailed further in this subsection.

Besides the inclusion of $U_{LJ}^{\alpha\beta}$, a torsional interaction potential ($U_{torsion}^{\gamma\alpha\beta\delta}$) is also added. This last term is a 4-body potential that is dependent on dihedral angles, which permits the capture of torsional interactions about single bonds. It is implemented in the AIREBO model for all dihedral angles in the system in proportion to the bond weights that contribute to the dihedral angle ($\omega^{\alpha\beta\gamma\delta}$) shown in figure 3.4[85] as:

$$U_{torsion}^{\gamma\alpha\beta\delta} = \frac{1}{2}\sum_{\alpha}\sum_{\beta\neq\alpha}\sum_{\gamma\neq\alpha,\beta}\sum_{\delta\neq\alpha,\beta,\gamma} w^{\alpha\beta}(r^{\alpha\beta})w^{\beta\gamma}(r^{\beta\gamma})w^{\gamma\delta}(r^{\gamma\delta}) \times V_{torsion}(\omega^{\alpha\beta\gamma\delta}), \tag{3.22}$$

where $V^{torsion}(\omega^{\alpha\beta\gamma\delta})$ is the torsional potential with a single minimum.

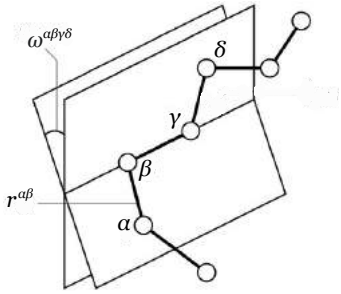

Figure 3.4: Schematic representation of the bond length $r^{\alpha\beta}$ and dihedral or torsion angle $\omega^{\alpha\beta\gamma\delta}$ of an arbitrary molecule.

The Embedded-Atom Method

In the EAM potentials,[86] the total energy U_{tot} of an elemental system is given by:

$$U_{tot} = \frac{1}{2}\sum_{\alpha\beta} V(r^{\alpha\beta}) + \sum_{\alpha} F(\bar{\rho}^{\alpha}), \tag{3.23}$$

where $V(r^{\alpha\beta})$ is a pair potential, which is a function of the distance $r^{\alpha\beta}$ between atoms α

and β. F is the embedding energy, which is a function of the atomic electron density $\bar{\rho}^{\alpha}$ that is represented as:

$$\bar{\rho}^{\alpha} = \sum_{\beta \neq \alpha} \rho(r^{\alpha\beta}). \tag{3.24}$$

Here, $\rho(r^{\alpha\beta})$ is the electron density function.

This potential was parameterized and fitted by Mishin *et al.*[80] and optimized by minimizing the weighted mean squared deviation of selected properties of Cu from their target values, which were taken from experiments or obtained by *ab initio* calculations. Thus, it was used to describe the interactions between Cu atoms in this work.

The Lennard-Jones Potential

The LJ potential[81] is a simple pair potential that works accurately when modeling weak van der Waals bonds between noble gases. It is also used to model covalent and metallic systems, but in these cases it is not as accurate because it does not include the environmental dependence of the bonding. However, it provides a qualitative understanding of all kinds of bonding due to a balance between a short-ranged repulsion and a long-ranged attraction.

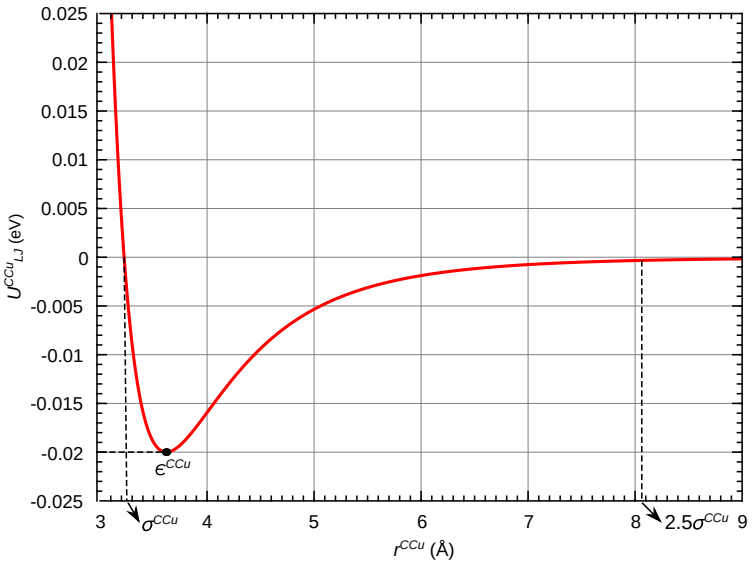

Figure 3.5: The energy U_{LJ}^{CCu} vs. distance r^{CCu} LJ potential when $\epsilon^{CCu} = 0.019996$ eV and $\sigma^{CCu} = 3.225$ Å.The cutoff radius of $2.5\sigma^{CCu}$ is also shown.

The potential has the following form:

$$U_{LJ}^{\alpha\beta} = 4\epsilon^{\alpha\beta}\left[\left(\frac{\sigma^{\alpha\beta}}{r^{\alpha\beta}}\right)^{12} - \left(\frac{\sigma^{\alpha\beta}}{r^{\alpha\beta}}\right)^{6}\right], \tag{3.25}$$

where $r^{\alpha\beta}$ is the distance between atoms α and β, $\epsilon^{\alpha\beta}$ is the well depth and a measure of how strongly the atoms α and β attract each other, and $\sigma^{\alpha\beta}$ is the distance at which the potential is zero (see figure 3.5), this being a measurement of how close the two non-bonding atoms α and β can get (van der Waals radius). $\epsilon^{\alpha\beta}$ and $\sigma^{\alpha\beta}$ are parameters determined by fitting to the known properties of the gas. In addition, the first and second terms in equation 3.25 are the repulsive and attractive ones, respectively. It can be noted that both decay with distance, the repulsive term decaying more rapidly.[87]

In this work, the $\epsilon^{\alpha\beta}$ and $\sigma^{\alpha\beta}$ parameters used to describe the interactions between C and Cu were $\epsilon^{CCu} = 0.019996$ eV and $\sigma^{CCu} = 3.225$ Å, respectively.[78] Also, the cutoff was set at $2.5\sigma^{CCu}$ (8.0625 Å), which is, as can be seen in figure 3.5, approximately where the potential converges.

3.5.4 Time Step

One of the most important parameters of a simulation is the time step (δt). An appropriate value has to be chosen in order to obtain a correct integration of Newton's equations of motion. If δt is too short, a high simulation time will be required from computing, resulting in an infeasible wait. On the other hand, if it is too long, the system dynamics will be unstable, resulting in an increment on the system energy, which then might be no longer conserved.[70] In this work, the forces are calculated and the positions and velocities of each particle are evaluated at every $\delta t = 1$ fs.

3.5.5 Structure Optimization and Relaxation

Once the positions of all particles, the boundary conditions, the interaction potentials, and the time step are defined, the next step taken in the simulations was to optimize the structures under analysis. For that, the energy of the system was minimized using the conjugate gradient technique. Here, the atoms rearrange themselves inside the simulation box to positions where a minimum energy is reached.

Subsequently, the system is relaxed to a thermal equilibrium state using the

isothermal-isobaric "NPT" (constant number of particles, pressure, and temperature) ensemble, which is a combination of the Nosé-Hoover thermostat and barostat. Here, the temperature was set at 1 K, which is the temperature at which the tensile test is carried out. Such parameter was chosen to avoid any thermal effects.[5]

3.5.6 Tensile Test

In order to determine the mechanical properties of the systems studied in this work, tensile tests were performed after the relaxation of the structure. A canonical "NVT" (constant number of particles, volume, and temperature) ensemble was used to maintain the temperature of the system at 1 K during the straining process, as well as to control the volume at each step of the stretching. The time integration is performed also using this ensemble on the Nosé-Hoover thermostat in LAMMPS.

The tensile tests were conducted by applying a strain rate of 5×10^{-4} ps^{-1} along the x-axis, the scheme is shown in figure 3.6. That means that after every picosecond, which corresponds to a hundred time steps (view subsection 3.5.4), the models are strained 0.005% of their initial x length (x_0).

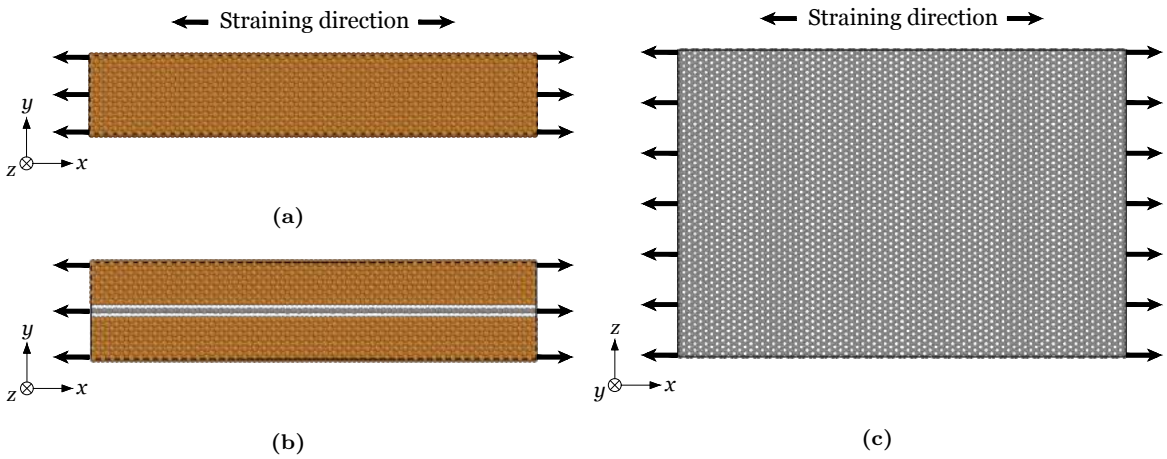

Figure 3.6: Schematic illustration of the uniaxial tensile tests performed on (a) pure Cu nanofilm (side view), (b) G-Cu heterostructures (side view), and (c) GNRs (top view). The black lines surrounding the models are the simulation box boundaries.

3.6 Stress Calculation

The stress on the atoms at a specified step of the stretching is computed from the stress tensor expression implemented by LAMMPS:[74]

$$\sigma_{ij}^{\alpha} = -\frac{1}{V^{\alpha}} \sum_{\alpha} \left(m^{\alpha} v_i^{\alpha} v_j^{\alpha} + \frac{1}{2} \sum_{\beta \neq \alpha} f_i^{\alpha\beta} r_j^{\alpha\beta} \right), \tag{3.26}$$

where i and j represent Cartesian coordinate system indices; V^{α} is the atomic volume; m^{α} is the mass of atom α; v_i^{α} and v_j^{α} are the i and j-components of the velocity of atom α, respectively; $f_i^{\alpha\beta}$ is the i-component of the force acting between atoms α and β; and $r_j^{\alpha\beta}$ is the j-component of the separation between atoms α and β.

In equation 3.26, the first term represents the kinetic contribution, and the second term is associated with the potential energy owing to the tensile deformation of the system.[4] V^{α} is calculated through the Voronoi tessellation of the atoms in the simulation box, where the set of all points closer to a specific atom than to any other forms that atom's Voronoi cell. The volume of the Voronoi cell can be computed by LAMMPS, and the sum of the volumes of all atoms' Voronoi cells gives the total volume of the system. The total stress can also be found by the sum of the stresses of all atoms, and since the uniaxial tensile load is applied along the x-axis, the x component of the stress in the system (σ_{xx}) is used to plot the stress-strain curves of the analyzed models.

3.7 Strain and Poisson's Ratio Calculation

Other outputs needed are the x, y, and z lengths of the system after specified step intervals. The lengths are needed to calculate the x, y, and z strains. The x strain, like σ_{xx}, is also used for the stress-strain curve plotting, and the y and z ones to calculate the Poisson's ratio on both perpendicular directions to the straining axis.

The x strain at a step s (ε_x^s) can simply be calculated with the x dimensions of the simulation box since it is the straining direction and the atoms on both x ends of the nanosystems move along with the x edges of the box. Therefore, we have

$$\varepsilon_x^s = \frac{x^s - x^0}{x^0} = \frac{\Delta x^s}{x^0}, \tag{3.27}$$

where x^s is the x dimension of the box at a step s and x^0 is the initial x dimension of the box, before uniaxial tensile loading, when $s = 0$.

On the other hand, a more accurate approach is needed to calculate the y and z dimensions of the system since curvatures on the faces along both directions appear during the stretching process, and the atoms do not move entirely according to the y and z boundaries of the simulation box. To compute more accurate values, the difference between the mean y coordinates of the atoms on both y end faces and the difference between the mean z coordinates of the atoms on both z end faces of the system are taken as their y and z dimensions, respectively. These atoms can be seen highlighted in figure 3.7. Thereby, firstly the mean y and z coordinates of the atoms on the higher y and z end faces at a step s ($\bar{y}_h^s$ and $\bar{z}_h^s$, respectively) are calculated as:

$$\bar{y}_h^s = \frac{1}{N_{y_h}} \sum_{\alpha=1}^{N_{y_h}} y_{\alpha_h}^s, \qquad (3.28) \qquad\qquad \bar{z}_h^s = \frac{1}{N_{z_h}} \sum_{\alpha=1}^{N_{z_h}} z_{\alpha_h}^s, \qquad (3.29)$$

where N_{y_h} and N_{z_h} are the number of atoms on the higher y and z end faces, respectively; and $y_{\alpha_h}^s$ and $z_{\alpha_h}^s$ are the y and z coordinates of the α atoms on the higher y and z end faces

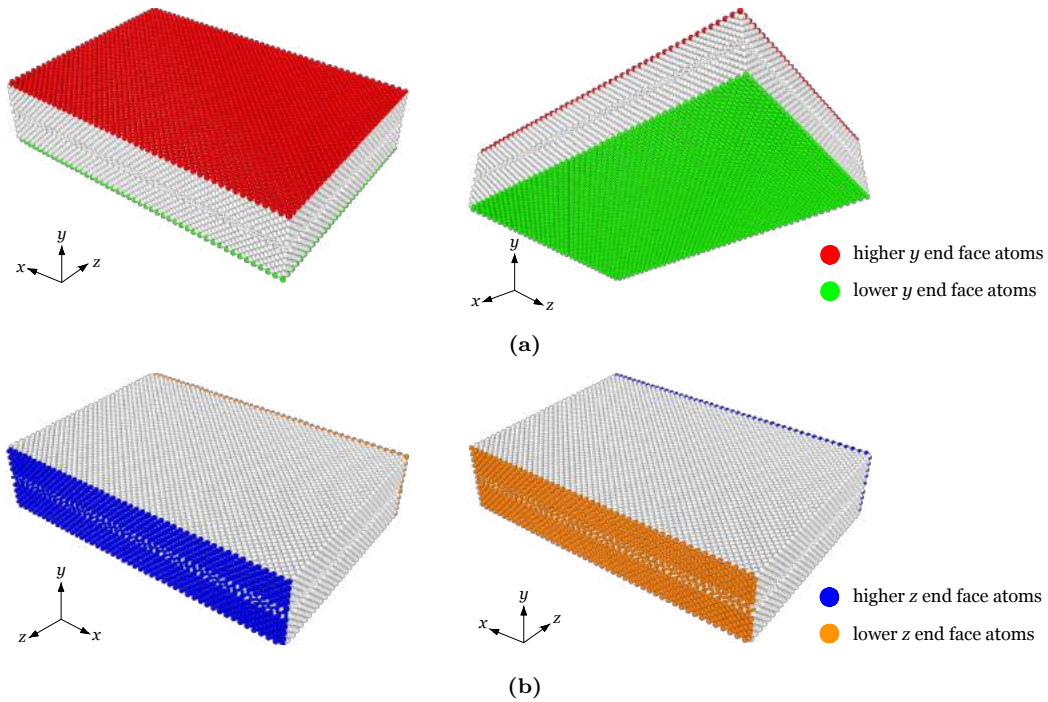

Figure 3.7: Schematic illustration of the atoms that compose the higher and lower (a) y and (b) z end faces of the systems analyzed. From (a), the mean y coordinates of the highlighted in red and green atoms were taken to calculate the y dimension at every step of the straining. From (b), the mean z coordinates of the highlighted in blue and orange atoms were taken to calculate the z dimension at every step of the straining.

at a step s, respectively. Then, the mean y and z coordinates of the atoms on the lower y and z end faces at a step s ($\bar{y}_l^s$ and $\bar{z}_l^s$, respectively) are calculated as:

$$\bar{y}_l^s = \frac{1}{N_{y_l}} \sum_{\beta=1}^{N_{y_l}} y_{\beta_l}^s, \tag{3.30}$$

$$\bar{z}_l^s = \frac{1}{N_{z_l}} \sum_{\beta=1}^{N_{z_l}} z_{\beta_l}^s, \tag{3.31}$$

where N_{y_l} and N_{z_l} are the number of atoms on the lower y and z end faces, respectively; and $y_{\beta_l}^s$ and $z_{\beta_l}^s$ are the y and z coordinates of the β atoms on the lower y and z end faces at a step s, respectively. Finally, the y and z dimensions at a step s (y^s and z^s, respectively) can be found as:

$$y^s = \bar{y}_h^s - \bar{y}_l^s, \tag{3.32}$$

$$z^s = \bar{z}_h^s - \bar{z}_l^s, \tag{3.33}$$

respectively. In the case of pure graphene, since it is two-dimensional and placed in the xz plane, only the z dimension is calculated with this approach. The y dimension is the thickness of graphene, witch is taken as the separation between two graphene layers in graphite, that is 3.4 Å.

Now, with more accurate y and z lengths, the y and z strains (ε_y^s and ε_z^s, respectively) can be calculated similarly to ε_x^s:

$$\varepsilon_y^s = \frac{y^s - y^0}{y^0} = \frac{\Delta y^s}{y^0}, \tag{3.34}$$

$$\varepsilon_z^s = \frac{z^s - z^0}{z^0} = \frac{\Delta z^s}{z^0}, \tag{3.35}$$

where y^0 and z^0 are the initial, before uniaxial tensile loading, y and z dimensions of the system, respectively.

Once ε_x^s, ε_y^s, and ε_z^s are known, and since the uniaxial tensile load is applied along the x-direction, the y- and z-direction Poisson's ratio at a specified step (ν_{xy}^s and ν_{xz}^s, respectively) can be calculated as:

$$\nu_{xy}^s = -\frac{\varepsilon_y^s}{\varepsilon_x^s}, \tag{3.36}$$

$$\nu_{xz}^s = -\frac{\varepsilon_z^s}{\varepsilon_x^s}. \tag{3.37}$$

3.8 Young's Modulus Estimation

In order to estimate the Young's modulus or modulus of elasticity (E), SSCs were obtained. E is the linear coefficient or the first derivative of the SSC elastic region, as discussed in

subsection 2.1.2. E of Cu and G-Cu systems can easily be acquired by basic linear fitting and interpolation since the elastic region of their SSCs is nearly linear, as shown in figures 3.8a and 3.8b. In these cases, E is the slope. However, the SSCs of pure graphene systems do not present a linear behavior in any section of the elastic region (see figure 3.8c), so a curve fitting approximating the dependence of the stress on the strain with a third degree polynomial was done, and the first order coefficient was taken as E.

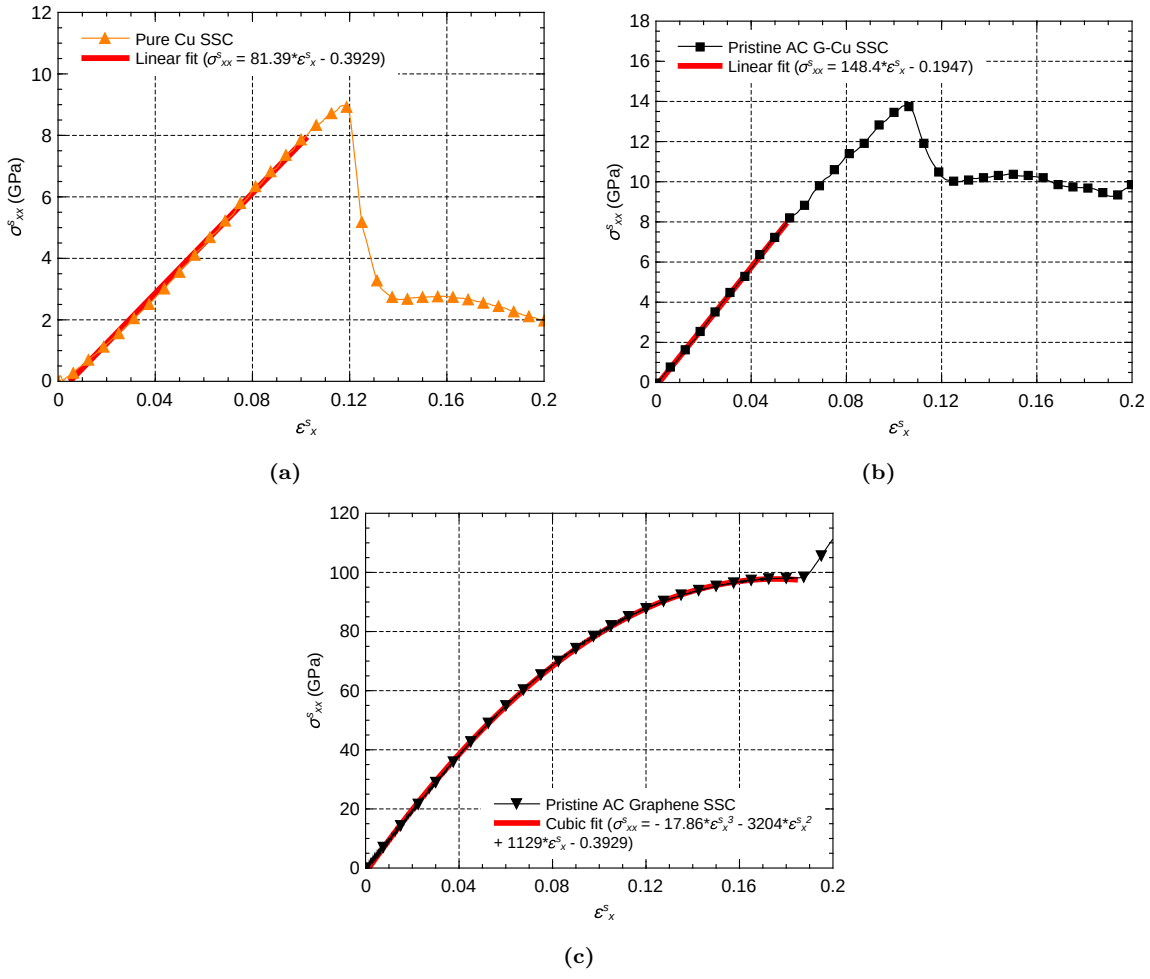

Figure 3.8: SSCs and their respective elastic region fitting: (a) pure Cu nanofilm, (b) pristine AC G-Cu heterostructure, and (c) pristine AC GNR. On the three examples displayed, estimated E values were (a) 81.39, (b) 148.4, and (c) 1129 GPa.

In the next chapter, the main results of our calculations are presented and analyzed.

Chapter 4

Results and Discussion

In order to understand the behavior of G-Cu heterostructures, results obtained from the tensile tests performed in pure graphene and Cu nanofilm are presented separately first. For all the systems, besides the atomic dynamics during the tensile test, the SSCs and the Poisson's ratio are analyzed.

4.1 Graphene Nanoribbons

In this section, results for pristine and defective AC and ZZ graphene nanoribbons are presented as a reference to understand its behavior within the composite.

4.1.1 Atomic Dynamics During the Tensile Test

In our calculations, which are performed until the systems fail, it is possible to follow their atomic structures during the process and observe how the displacements give rise to different stages which depend on chirality and defects. Thus, after a slight change of the bonding distance among atoms, structural phase transitions may occur and the fracture process turns out also to be different in each case. We first discuss the AC GNRs and then compare to the ZZ ones. In Appendix A, figures A.1, A.2, and A.3 show the snapshots of the tensile tests conducted on AC pristine and defective graphene with ρ_{Vac} and ρ_{SW} values of 0.03, respectively. It can be seen that a phase transition starts to take place at a $\varepsilon_x^s \approx 0.2370$ in each case. Such effect was also observed by Ma *et al.*[32] in pristine AC GNRs. They found that sheared regions appear at a certain strain, where the stress sustaining during tensile testing is transferred from parallel to angular bonds. That induces an inhomogeneous stress

distribution, specially near the edges, and shearing is activated and extended gradually along some preferred directions, similar to slipping in metals. Consequently, a structural phase transformation from hexagonal to orthorhombic lattices occurs. It can be noticed, from our study, that this effect is more susceptible in the pristine case. In figures A.1d, A.2d, and A.3d this is very evident. When vacancies and SW defects are present, the phase transformation occurs in a lower proportion and in a less orderly way. Moreover, this effect is a lot more perceptible in the presence of vacancies than in that of SW defects. Our hypothesis is that vacancies prevent large sheared regions to form due to a disorder at some point of the lattice where bonds are missing and the stress sustaining cannot be equally transferred from parallel to angular bonds. In SW defects, however, there are no missing bonds, one of them is just oriented in a different way, and somehow it allows larger sheared regions to form. In order to verify such hypothesis, the x-component of the stresses on each atom α (σ^{α}_{xx}) is mapped and analyzed, the result is shown in figure 4.1. Observe that, in fact, the distribution loses the uniformity in the presence of defects (figures 4.1b and 4.1c), specially vacancies. Atoms at higher and lower σ^{α}_{xx} values near the defects can be seen. This confirms that the stress cannot actually be ordinarily transferred in defective systems.

From the snapshots, it can also be observed that the fracture process in defective AC GNRs happens more gradually than in the pristine one. This effect is more noticeable at higher ρ_{Vac} and ρ_{SW} values. From figures A.1, A.2, and A.3, it can be found that the difference between the ε^{s}_{x} value where the nanoribbons have already completed their fracture process, figure (g), and the ε^{s}_{x} value where they had just began to fail, figure (f), is larger in the defective systems. In the pristine case, the difference between the ε^{s}_{x} values from figures A.1g and A.1f is $\Delta\varepsilon^{s}_{x} = 0.0190$, whereas with vacancies at $\rho_{Vac} = 0.03$, $\Delta\varepsilon^{s}_{x} = 0.0235$ from figures A.2g and A.2f. As per the AC GNR with SW defects at a $\rho_{SW} = 0.03$, from figures A.3g and A.3f, the difference is $\Delta\varepsilon^{s}_{x} = 0.0315$. This means that the fracture process takes longer in defective systems than it does in the pristine one. That happens because, when defects are present, some C-C bonds start breaking before others do. To explain this behavior, we base our hypotheses in the σ^{α}_{xx} distribution map as well (figure 4.1). It can be seen that, while it is uniform in the pristine AC GNR, thanks to its also uniform atomic distribution, in defective ones, as already mentioned, some atoms sustain higher stresses than others, which explains why bonds between these higher stress sustaining atoms break before bonds between lower stress sustaining ones. This uneven stress distribution happens because vacancies and SW defects get on the way of the load, which, due to missing bonds

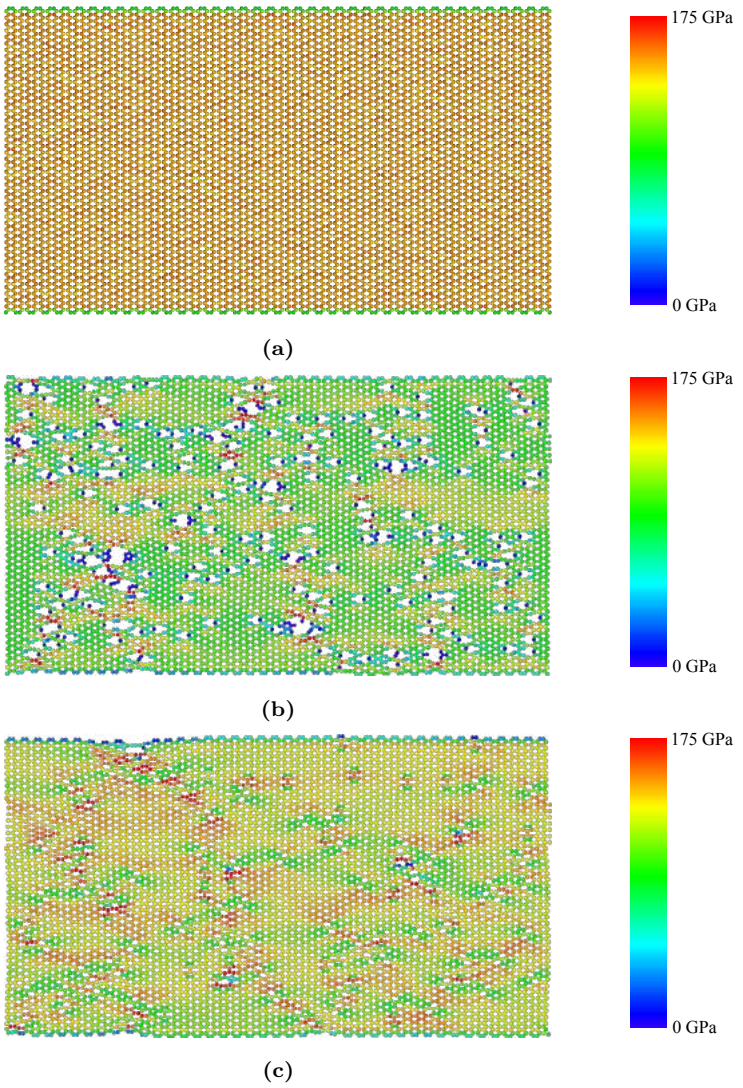

Figure 4.1: σ^{α}_{xx} distribution maps of the analyzed AC GNRs at a $\varepsilon^{s}_{x} = 0.2370$, where the phase transition starts to take place. (a) Pristine, (b) Vacancies at a $\rho_{Vac} = 0.03$, and (c) With SW defects at a $\rho_{SW} = 0.03$. Warmer colors represent higher stresses, colder colors lower ones.

or disorders in the lattice, cannot be distributed evenly throughout the AC GNR in a straightforward path during a tensile test. Therefore, zones with atoms at higher stresses form, specially between close by defects, where the load has to make its way in order to distribute the stress throughout the entire AC GNR. In other words, since there are defects or "holes" in the lattice, broken bonds cannot concentrate through a region to start a fracture. Thus, if a vertical line is drawn on a defective AC GNR, it will touch less atoms than it would on a pristine one, and that means that there are less atoms to sustain the

same amount of stress more atoms in a pristine material do. This is more evident in the presence of vacancies. It can be noticed that atoms positioned on the right or left side of these defects have a near zero or negative stress (blue color atoms), a negative stress represents compression, while the atoms above or under the defects possess higher stresses. That happens because the uniaxial tensile load is along the x (horizontal) axis, and it has to make its way over or under the defects to distribute the stress throughout the AC GNR. On the other hand, since the stress distribution is uniform in the pristine one, C-C bonds on the fracture path break pretty much at the same time, causing a more brittle failure.

Another observation made was that, after the nanoribbons break apart into two pieces and consequently the remaining slices get unloaded, the C atoms tend to rearrange themselves back to the initial honeycomb lattice (see figures A.1g, A.2g, and A.3g). It makes sense since this is the equilibrium configuration of C atoms in graphene when no external forces are acting on them.

The dynamics is slightly different when the GNRs are strained along the ZZ edge. Under this circumstance, a phase transformation at a certain ε_x^s, either in pristine or defective nanoribbons, does not occur, as shown in figures A.4, A.5, and A.6. Here, according to Ma *et al.*, the stress sustaining is mainly exerted on the angular bonds, which increase along with the angles between them, throughout the entirety of the tensile test, and the hexagonal lattices are gradually stretched into nearly rectangular ones before failure.

Moreover, the fracture process in defective ZZ GNRs, in contrast to the AC ones, happens at earlier ε_x^ss, specially at higher ρ_{Vac}s and ρ_{SW}s. What they have in common with AC GNRs is that they also break apart more gradually than their pristine counterparts, this effect being more noticeable at higher ρ_{Vac}s and ρ_{SW}s as well, and the reason is the same for both chiralities: while the σ_{xx}^{α} distribution in pristine ZZ GNRs is uniform, in defective ones some atoms sustain higher stresses than others (see figure 4.2), and bonds between the higher stress sustaining atoms break before. This uneven stress distribution occurs for the same reason it occurs in AC GNRs. Also, like in these latter cases, after the fracture process is completed, the atoms in the two remaining slices tend to return to their original lattice, with the initial bond lengths and angles, as a result of unloading after failure.

It can also be seen from the snapshots that the crack orientation in AC GNRs is perpendicular to the orientation of the tensile load while it appears diagonally at an angle of approximately $\pm$ 60° in ZZ GNRs. This effect can be seen in figures A.1g, for the AC GNR, and A.4d, for the ZZ GNR. Note the crack orientation in both cases. As discussed

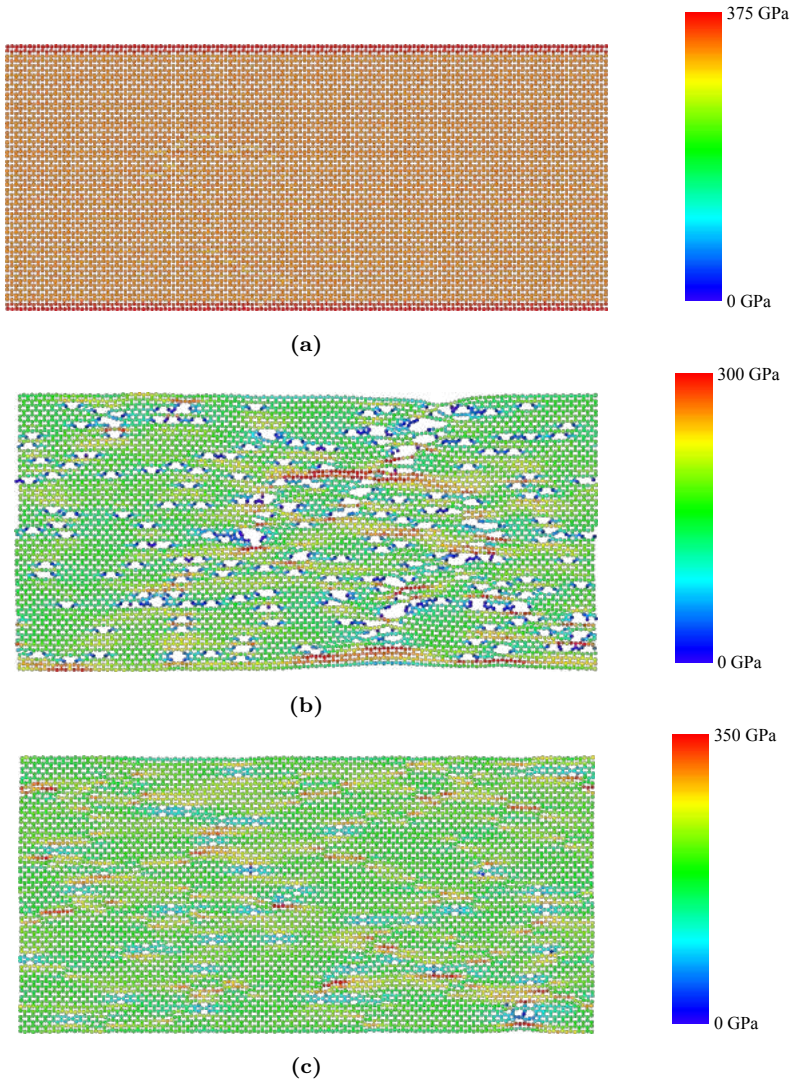

Figure 4.2: σ^{α}_{xx} distribution maps of the analyzed ZZ GNRs right before their fracture process starts to take place. (a) Pristine at a $\varepsilon^{s}_{x} = 0.4250$, (b) With vacancies at a $\rho_{Vac} = 0.03$ and $\varepsilon^{s}_{x} = 0.3805$, and (c) With SW defects at a $\rho_{SW} = 0.03$ and $\varepsilon^{s}_{x} = 0.3645$. Warmer colors represent higher stresses, colder colors lower ones.

in one of the previous paragraphs, in AC graphene the fracture is caused by shearing which is perpendicular to the direction of the load, consequently the crack orientation is also perpendicular. As for ZZ chirality, the stress is being sustained mostly by the angular bonds. At some point, the stress exceeds the strength of some of these bonds and they break. Ni *et al.*[31] explain that, once the crack front is triggered in ZZ graphene, the left bonds in the same direction will eventually sustain the external load, and that will lead to a sequencing instantaneous rupture along the same direction. Thus, a 60° crack is observed.

The atomic dynamics during the conducted tensile tests will be reflected in the SSCs of the analyzed systems, which will be discussed in the next subsection.

4.1.2 Stress-Strain Curves and Young's Modulus

Figure 4.3 shows the SSCs of all the analyzed pure graphene systems. It can be seen the response of pristine GNRs (black curves) to mechanical tensile stress and how it changes depending on the vacancy density (ρ_{Vac}) and SW (ρ_{SW}) defects (colored curves). The chirality is also analyzed: graphene behaves differently when the tensile load is parallel to the AC edge (upside down triangles) compared to when it is parallel to the ZZ edge (dots)

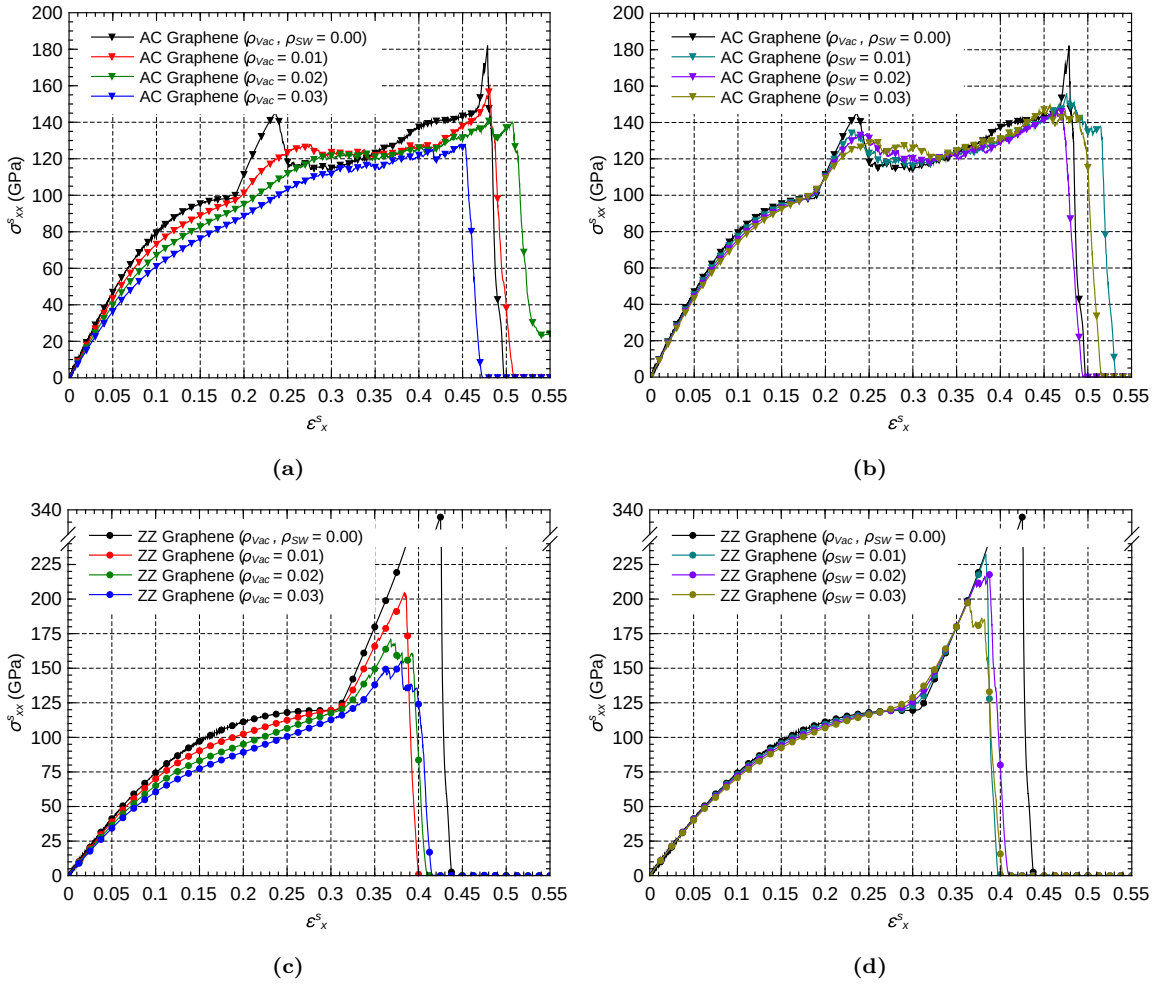

Figure 4.3: SSCs of the analyzed pure graphene systems at different densities of defects: (a) and (b) AC GNRs with vacancy and SW defects, respectively, and (c) and (d) ZZ GNRs with vacancy and SW defects, respectively.

of the nanoribbon.

In figure 4.3a, the elastic regions of the SSCs show a noticeable drop in strength of pure GNRs with the increase of ρ_{Vac}. Consequently, vacancy defects result in a less stiff material with a drop in E being observed, as shown in table 4.1 and figure 4.4. At a $\varepsilon_x^s \approx 0.1900$, a sudden increase in strength is observed, being more pronounced in pristine graphene, where a maximum of $\sigma_{xx} = 145.426$ GPa is reached at a $\varepsilon_x^s \approx 0.2362$. This is the point where the phase transition discussed in the previous subsection starts to occur. This effect diminishes with the increase in ρ_{Vac}, and it is almost absent when 3% of the sites in the lattice is occupied by vacancies. That could be a consequence of the shearing stresses not being able to be completely formed in the presence of such defects in the lattice, as mentioned in subsection 4.1.1, and less stress is being sustained to reach a certain ε_x^s. The same occurs when SW defects are present in the AC GNR, as seen in figure 4.3b, although, this vanishing effect of the first maximum in the SSC occurs in a less dramatic way.

After the first maximum is reached and the phase transition has already started to

Table 4.1: Estimated E, σ_{TS}, and ε_F values of AC and ZZ GNRs at different density of defects.

Chirality	Defect type	Density of defects	E (TPa)	σ_{TS} (GPa)	ε_F
AC	No defects	0.00	1.129	182.282	0.4786
	Vacancy	0.01	1.102	158.583	0.4810
		0.02	1.007	142.442	0.5073
		0.03	0.932	127.580	0.4528
	Stone-Wales	0.01	1.064	156.238	0.5150
		0.02	1.037	146.651	0.4708
		0.03	1.016	149.685	0.4853
ZZ	No defects	0.00	0.984	334.240	0.4251
	Vacancy	0.01	0.980	204.986	0.3841
		0.02	0.928	167.861	0.3927
		0.03	0.868	155.335	0.3979
	Stone-Wales	0.01	0.963	232.867	0.3835
		0.02	0.947	218.143	0.3877
		0.03	0.929	200.653	0.3819

take place, a drop in strength is observed in the SSC of the pristine AC GNR. Slighter drops are also observed in the SSCs of AC GNRs with SW defects and vacancies when the ρ_{Vac} = 0.01. However, when ρ_{Vac} values are 0.02 and 0.03, a maximum cannot be observed at this region. What all the SSCs of the AC systems have in common though, is that basically a stress terrace appears in the range of ε_x^ss where the phase transition is occurring. Ma *et al.*[32] found that the Schmidt factor, which is a ratio between the shear stress (τ) and σ_{xx}^s, increases significantly before the phase transition point is reached, and the honeycomb-to-orthorhombic change in the structure of the AC GNRs starts to take place. Further, σ_{xx}^s does not change the Schimidt factors in the sheared and unsheared regions by much, which implies that an increase in ε_{xx}^s is maintained through gradual lattice shearing. Consequently, the stress terraces appear in the SSCs of AC GNRs. They call this effect as "elongation of the yield point". Therefore, it is hard to tell exactly the values of σ_Y and $\varepsilon(\sigma_Y)$, since their point is elongated.

After the stress terrace, another sudden increase in strength is observed in the pristine AC GNR until it reaches the σ_{TS} point at a $\varepsilon_x^s = 0.4786$, and then a dramatic drop in the SSC appears. This indicates a brittle fracture of the material. On the other hand, when vacancies and SW defects are present, as shown in figures 4.3a and 4.3b, respectively, the increase in strength after the terrace is not as sudden as in the pristine nanoribbon, in some cases it is even nonexistent. The SSCs of defective AC GNRs, furthermore, do not show a fracture process as brittle as the one shown in the SSC of the pristine one, as

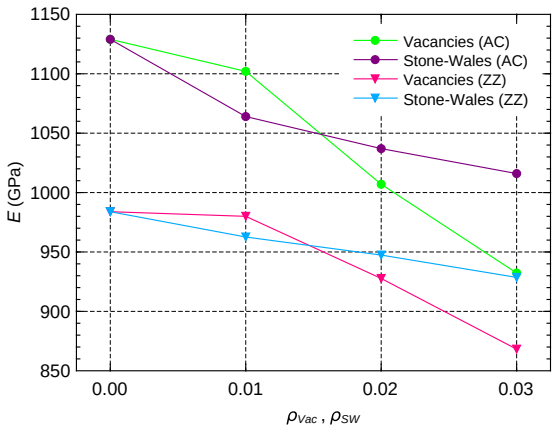

Figure 4.4: E values of AC and ZZ GNRs at different densities of defects. Note that AC GNRs are stiffer and that vacancies have a higher impact in E.

already seen in figures A.1, A.2, and A.3, and discussed in subsection 4.1.1, where the reason behind the occurrence of a less brittle fracture process in defective GNRs was discussed. Surprisingly though, defective AC GNRs for ρ_{Vac} values of 0.01 and 0.02 and ρ_{SW} of 0.01 and 0.03, the fracture happens at later ε_x^ss than that of the pristine one, they present higher ε_F values. That means that, in this range of density of defects, defective AC GNRs can be more ductile than a pristine one, which would be handy in extreme case-scenarios where a big deformation could be reached. However, while ε_F is higher at certain densities of defects, σ_{TS} does decrease with increasing ρ_{Vac}s and ρ_{SW}s. After all, although less ductile in some cases, pristine AC GNRs can still endure higher stresses before failure than the defective ones.

Figures 4.3c and 4.3d show the SSCs of ZZ GNRs with vacancies and SW defects, respectively. The SSC of pristine GNR is shown in both graphs for comparison. Taking a look at lower ε_x^ss, it can be noticed that the strength defective ZZ GNRs endure, at a certain ε_x^s, decreases with increasing ρ_{Vac} and ρ_{SW}, the pristine ZZ GNR enduring higher σ_{xx}s. This effect is significantly more noticeable when the defects are vacancies, just like in AC GNRs. Consequently, E values will be lower with higher ρ_{Vac} and ρ_{SW} values, as displayed in table 4.1 and figure 4.4.

The nature of these curves is different from those of AC GNRs at higher ε_x^ss though. Since ZZ GNRs do not present a phase transformation where shear stresses play a bigger role than tensile stresses, a stress terrace does not appear. Instead, after a sudden increase in strength, which begins to take place around a ε_x^s value of approximately 0.3100, the SSCs of ZZ GNRs reach a maximum, which is their σ_{TS} point, and the failure process begins. In the SSC of the pristine ZZ GNR, the σ_{TS} point goes as high as 334.240 GPa, and it drops substantially when defects are present, specially vacancies (see table 4.1). The fracture also happens at earlier ε_x^ss in defective ZZ GNRs, differently from the AC ones, where certain densities of defects improved the ductility of the material. On the other hand, the nature of the failure is similar in AC and ZZ GNRs, it becomes less brittle with the increase in density of defects, as already seen in figures A.4, A.5, and A.6, and discussed in subsection 4.1.1.

The results also show that AC GNRs, in general, are stiffer and tougher than ZZ ones, that is, they present higher E values (see table 4.1 and figure 4.4) and also reach their σ_{TS} point at higher ε_x^s values. However, higher stresses have to be reached in ZZ GNRs in order to break them. Thus, they are more resistant. Furthermore, vacancies have a higher

impact in the mechanical properties of GNRs and in general the effect is non linear. E values estimated in this work as well as their dependence on the chirality and defect type and density on graphene are in good agreement with previous results.[3,6,7,30–37]

4.1.3 Poisson's Ratio

Figures 4.5a and 4.5b show the calculated ν^s_{xz} of AC GNRs with vacancies and SW defects, respectively, at different ε^s_xs up to 0.2200, right before the phase transition takes place. The pristine values are also plotted for comparison. They are higher than the defective ones initially, at $\varepsilon^s_x \approx 0.0100$. However, at a certain strain, this behavior is switched and

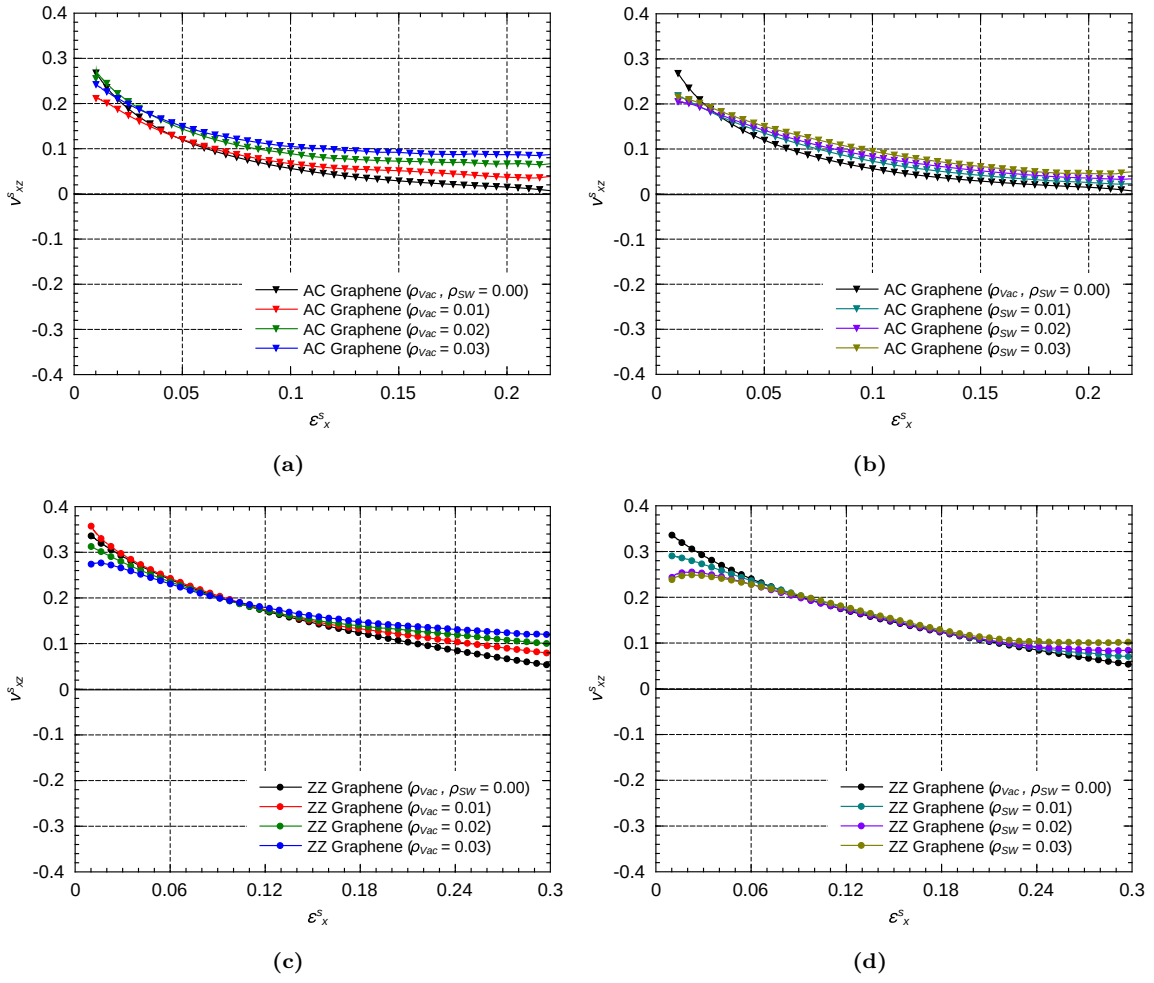

Figure 4.5: ν^s_{xz} as a function of ε^s_x for the analyzed pure graphene systems at different densities of defects: (a) and (b) AC GNRs with vacancy and SW defects, respectively, and (c) and (d) ZZ GNRs with vacancy and SW defects, respectively. Pristine cases are included for comparison.

defective GNRs start presenting higher ν_{xz}^s values. Note that, in the ε_x^s range that begins approximately at 0.045 (0.03), when vacancies (SW) are present, the higher ρ_{Vac} and ρ_{SW} are, the higher ν_{xz}^s is as well, specially when the defects are vacancies. It can also be noted from the curves that, at small ε_x^ss, there is a considerable decrease in ν_{xz}^s, which starts at approximately 0.26 in the pristine GNR and at slightly lower values in defective GNRs. Nonetheless, at larger ε_x^ss they stay almost constant between 0.0 and 0.1, depending on the defect type and its density. These results agree well with previous ones.[3,26,27,30,32]

Figures 4.5c and 4.5d show ν_{xz}^s of ZZ GNRs with vacancies and SW defects, respectively, at ε_x^s up to 0.3000, right before the strengthening process begins. The pristine GNR ν_{xz}^s values are also shown. The behavior here is similar to that of AC GNRs: there is a somehow substantial decrease in ν_{xz}^s at small ε_x^s, but it is almost constant at larger ones. Also, the pristine shows high ν_{xz}^s values at earlier ε_x^ss than those of defective ZZ GNRs, but lower at higher values, except when the nanoribbon has vacancies at a $\rho_{Vac} = 0.02$. It can also be noticed that ν_{xz}^s of defective GNRs are almost equal to those of the pristine in the range of ε_x^ss ≈ 0.0700 to 0.1100 when the defects are vacancies and ≈ 0.0700 to 0.2200 when they are 5-7-7-5 SW pairs. This range is noticeably higher in the latter case. It was already discussed how vacancies have a greater impact in the mechanical properties of graphene and it is clear that it also applies for the Poisson's ratio. Moreover, ZZ GNRs present higher ν_{xz}^s values than AC GNRs. They begin at around 0.35 at a $\varepsilon_x^s = 0.0100$ and remain in a range that goes from approximately 0.05 to 0.25 at higher ε_x^ss in all cases. This can be explained by the fact that, according to Ma *et al.*,[32] when GNRs are stretched along the AC edge the parallel bonds are the ones that noticeably increase in length while the angular ones and the angle between them do not change considerably. However, when they are stretched along the ZZ edge, the angular bonds and the angles between them, are the ones that see a higher increase. Consequently, the perpendicular dimension to the direction of the load is more affected, and the Poisson's ratio is higher.

It is important to mention that the Poisson's ratio does not become negative in any case. Therefore, for the chosen conditions, the GNRs do not show an auxetic behavior.

4.2 Copper Nanofilm

In this section, results for a pure Cu nanofilm are presented also as a reference to understand its behavior when a graphene layer is introduced inside the film.

4.2.1 Atomic Dynamics During the Tensile Test

Similarly to the GNRs, Figure B.1 shows the evolution of the pure Cu nanofilm under tensile testing. It can be observed that dislocations appear on the surface of the material once its plastic deformation starts (see figure B.1c). In inner layers, dislocations can also be seen, as shown in figure 4.6, where a dislocation analysis (DXA) is done with the Open Visualization Tool (OVITO),.[88] It can be observed that they originate right in the geometric center of the nanofilm and are extended to the borders forming an "X'. Such symmetry in the formation of early deformations could be a consequence of the also symmetrical distribution of the x-component of atomic stresses (σ^{α}_{xx}) during elastic deformation, as observed in figure 4.8a. Once the first dislocations are formed, the stress is not symmetrically distributed anymore (see figure 4.8b) and, throughout the tensile test, atoms in these dislocations can recrystallize back to an FCC configuration, and new ones can be formed at new sites, as portrayed in figure 4.7 where the Cu nanofilm is at a higher ε^{s}_{x}.

It can also be noted from figure 4.8b, that, at dislocations, atoms present very low σ^{α}_{xx} values, which makes sense because, since these atoms are losing bonds to form the observed dislocations, they are losing their capacity to transfer and sustain load. This behavior is a consequence of the slip mechanism mentioned in subsection 2.3.1, which provides

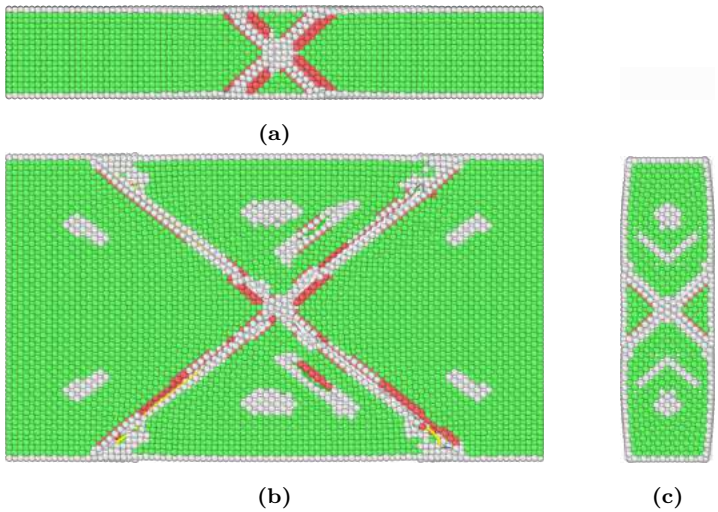

Figure 4.6: Pure Cu nanofilm at $\varepsilon^{s}_{x} = 0.1220$, where initial dislocations at selected central slices in the (a) xy-, (b) xz-, and (c) yz-planes can be seen. Green atoms are arranged in the original FCC structure of Cu, red atoms in the hexagonal close packed (HCP), and the white atoms in other types of lattices. White atoms also represent those located at the free surfaces.

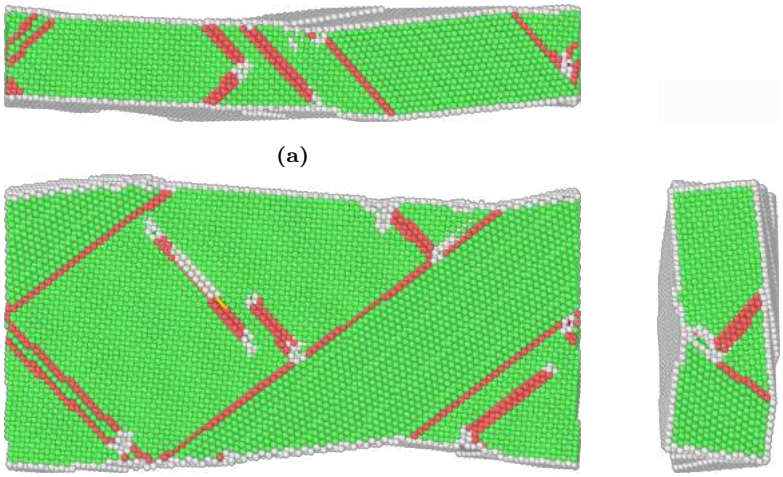

Figure 4.7: Pure Cu nanofilm at $\varepsilon_x^s = 0.2000$ at selected central slices in the (a) xy-, (b) xz-, and (c) yz-planes. New dislocations are observed compared to those shown at figure 4.6. Green atoms are arranged in the original FCC structure of Cu, red atoms in the HCP, and the white atoms in other types of lattices. White atoms also represent those located at the free surfaces.

the excellent ductility and toughness in Cu structures. Such ductility could be observed in the simulation conducted in this work, where the time steps set were not enough for the Cu nanofilm to reach its fracture point. Necking, which is a type of plastic deformation observed in ductile materials under tensile stress, could be observed though. This deformation occurs when a localized reduction in the cross-sectional area is observed.

The surface effect mentioned in section 2.4 can also be observed using OVITO.

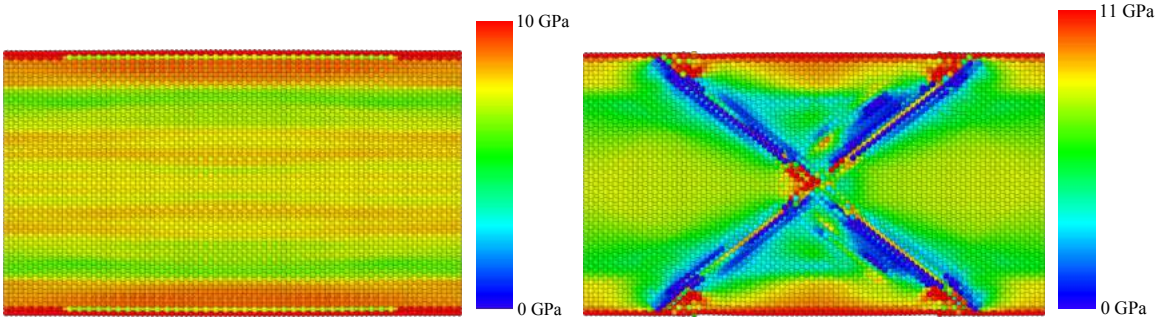

Figure 4.8: σ_{xx}^{α} distribution maps at a selected central slice in the xz-plane of the analyzed pure Cu nanofilm at a (a) $\varepsilon_x^s = 0.1165$, right before the σ_Y point, and at a (b) $\varepsilon_x^s = 0.1220$, where first dislocations appear at the beginning of plastic deformation.

The result is shown in figure 4.9. Here, it can be seen that the atoms that compound the free y and z surfaces have considerably higher σ^{α}_{yy} and σ^{α}_{zz} values than the inner atoms. As already discussed, since the tensile load is being applied along the x-direction, the total y and z components of the stress should be near zero, and due to the fact that surface atoms present high σ^{α}_{yy} and σ^{α}_{zz} values, the stress at the inner atoms have to be substantially lower to compensate. In the pure Cu nanofilm analyzed in this work, the stress distributions along the y- and z-directions are homogeneous, symmetrical, and countervailing, which is favorable for the stability of the material. These results are in good agreement with previous ones.[4,5]

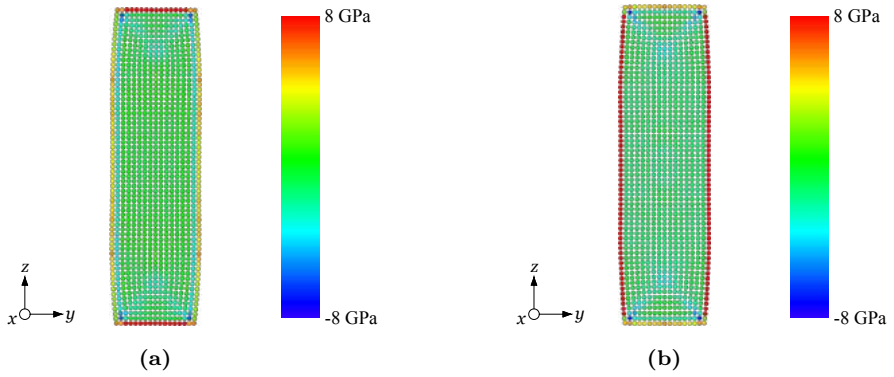

Figure 4.9: (a) σ^{α}_{yy} and (b) σ^{α}_{zz} distribution maps of the analyzed Cu nanofilm at a selected central slice in the yz-plane. The deformation is $\varepsilon^{s}_{x} = 0.1165$, right before the specimen reaches its σ_Y point.

4.2.2 Stress-Strain Curve and Young's Modulus

Figure 4.10 shows the SSC of the analyzed pure Cu nanofilm. Initially, the relation between the stress σ_{xx} and strain ε^{s}_{x} is nearly linear, which is characteristic of most materials. The proportional limit goes up to σ_{xx} and ϵ^{s}_{x} values of approximately 7.8 GPa and 0.1000, respectively. At $\varepsilon^{s}_{x} = 0.1169$, the yield strength σ_Y point is found at a $\sigma_{xx} = 9.211$ GPa. Figure B.1b illustrates the Cu nanofilm right before this point is reached. After the σ_Y point, the material enters the plastic region, and dislocations start to form as a consequence of the slip mechanism. Here, a significant drop in the SSC is observed. The lower-yield point is reached at $\varepsilon^{s}_{x} = 0.1419$ and $\sigma_{xx} = 2.592$ GPa: a much lower load is now needed to keep stretching the nanofilm. A representation of the Cu nanofilm at this point can be seen in figure B.1c. After an almost unnoticeable increase in the endured σ_{xx} subsequent to this point, there is a slight drop in the SSC until a σ_{xx} value of 1.851 GPa is reached at $\varepsilon^{s}_{x} =$

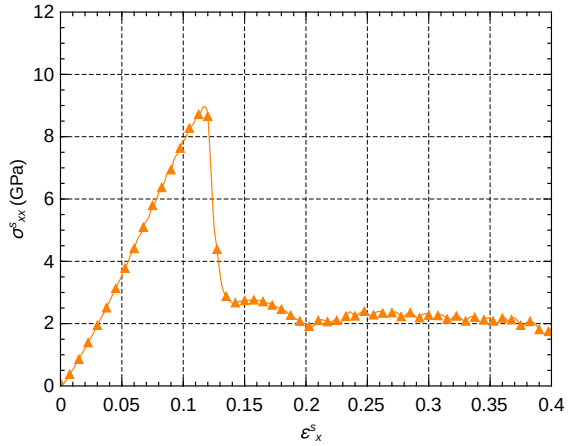

Figure 4.10: SSC of the analyzed pure Cu nanofilm.

0.2060. An illustration of the pure Cu nanofilm at this point can be seen in figure B.1d. Here, necking deformation has also already began to occur. After that, a plateau, where σ_{xx} values stay around 2.25 GPa, can be observed. Also, the neck in the Cu nanofilm becomes more and more evident (see figure B.1e). Due to the high ductility of Cu, the σ_{TS} point was not reached in the range of ε^s_x values taken into account in our simulation.

Differently from graphene, Cu presents a nearly linear elastic region, as mentioned previously. Therefore, E here can be estimated as the slope through interpolation and linear fitting. The estimated value for the analyzed Cu nanofilm was 81.39 GPa, which is in good agreement with previous results where Cu nanosystems were also studied experimentally,[56] where E values between 70.7 and 102.1 GPa were reported, and through MD simulations,,[59–61] where E values between $\approx$ 80 and 100 GPa were estimated.

4.2.3 Poisson's Ratio

Figure 4.11 shows ν^s_{xy} and ν^s_{xz} values of the analyzed pure Cu nanofilm at an earlier stage of ε^s_x values. In the thickness direction (y-direction), the initial value found, at $\varepsilon^s_x = 0.0100$, is approximately 0.3. This is in good agreement with previous results.[5,58] Later on, ν^s_{xy} values drop slightly throughout the tensile test, but remain positive throughout the entirety of elastic deformation. Around the ε^s_x where the SSC of the pure Cu nanofilm reaches its lower-yield point, ν^s_{xy} values become negative. This behavior was also observed in reference 5, where a thin Cu nanofilm with the same dimensions as the one analyzed in this work

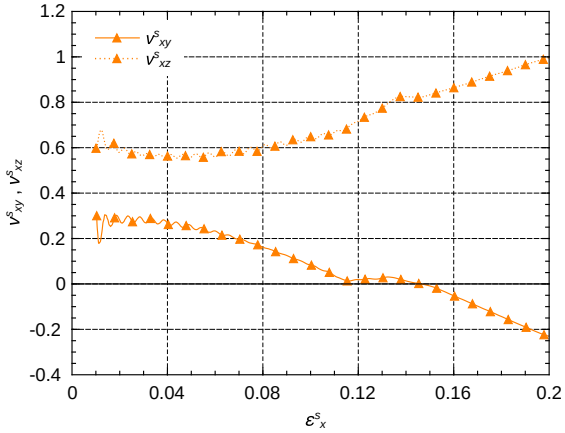

Figure 4.11: ν^s_{xy} and ν^s_{xz} values of the analyzed pure Cu nanofilm.

presented NPR at a high strain during plastic deformation.

As for ν^s_{xz} values, the behavior is opposite to the one observed in the thickness direction. A value of around 0.6 was computed at a $\varepsilon^s_x \approx 0.0100$, and after that, a slight increase is observed instead of a slight decrease, almost mirroring the curve of ν^s_{xy} values. This is a result of the branching effect mentioned in section 2.4, which has been revealed in reference 67. Furthermore, branching is also a result of the surface effect, where compressive values compound one of the transverse components of atomic stresses in inner atoms of thin nanofilms and induce a reduction in the Poisson's ratio of the other transverse direction in a 3D system, negative values being possible to be obtained.

4.3 Graphene-Copper Heterostructures

Finally, in this section we present the results obtained for the G-Cu heterostructures. The dependency of the mechanical properties on the chirality of the graphene layer, defect type and density of defects is analyzed.

4.3.1 Atomic Dynamics During the Tensile Test

Figure C.1 shows the front and top views of the pristine AC G-Cu heterostructure at different ε^s_x values during the tensile test. It can be seen that the deformation mechanism of the Cu layers in the nanocomposite is similar to that of the pure Cu nanofilm: dislocations are formed during plastic deformation as a consequence of slippage. In figure 4.12, these

dislocations are shown at central slices in different planes a few steps after the material enters the plastic region. In the pure Cu nanofilm, as discussed in subsection 4.2.1, it was observed that the origin of dislocations is located right in the center of the nanofilm, and that they were symmetric in the first steps of plastic deformation. However, in the pristine AC G-Cu heterostructure, dislocations do not originate right in the center, and they are not symmetric not even in the first steps of plastic deformation. That might be due to the distribution of the x-component of the atomic stress (σ^{α}_{xx}), which is symmetrical within the pure Cu nanofilm during elastic deformation, as it was shown in figure 4.8a. However, this symmetry is not observed in the Cu layers of the pristine AC G-Cu heterostructure, which can be seen in figure 4.13, as might be expected of a composite made of materials with cubic and hexagonal symmetries. Furthermore, as it can be seen in figures 4.12a and 4.12c, dislocations begin to form in the upper Cu layer earlier than in the lower one, even though the heterostructure is symmetric. Eventually, dislocations also start to appear in the lower Cu layer throughout the tensile test.

Looking at the heterostructure as a whole in figures C.1a and C.1b, it can be noted an increase in length along the thickness direction, which corresponds to the y-direction and is shown vertically in the front views. This direction is perpendicular to the horizontal

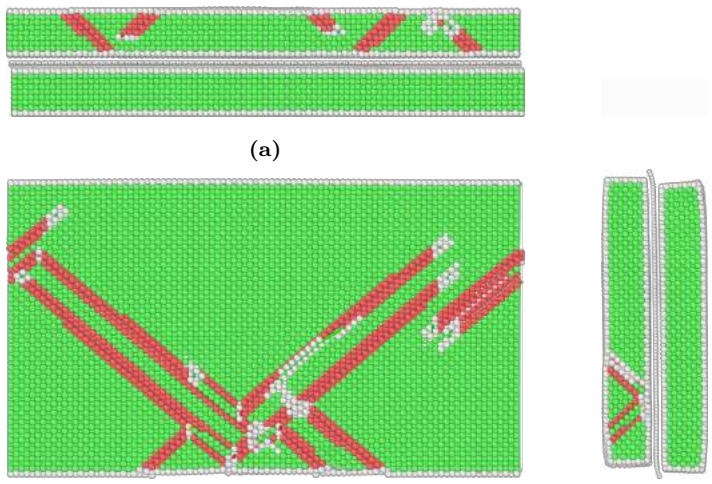

Figure 4.12: Pristine AC G-Cu heterostructure at $\varepsilon^{s}_{x} = 0.1070$, where initial dislocations in the (a) xy-, (b) xz-, and (c) yz-planes can be seen. In (a) and (c), selected central slices of the overall heterostructure are shown. In (b), a selected central slice in the upper Cu layer is shown. Green atoms are arranged in the original FCC structure of Cu, red atoms in the hexagonal close packed (HCP), and the white atoms in other types of lattices. White atoms also represent those located at the free surfaces.

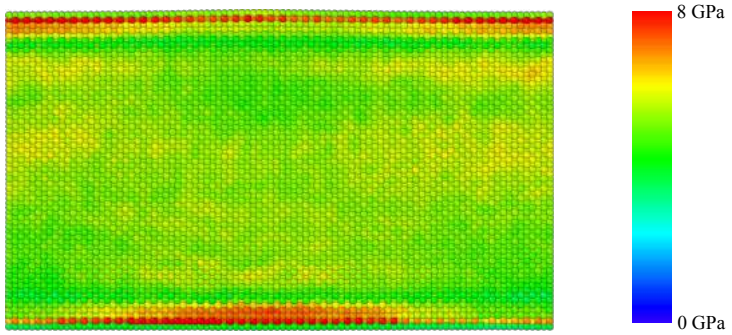

Figure 4.13: σ^{α}_{xx} distribution map at a selected central slice in the xz-plane of the upper Cu layer in the pristine AC G-Cu heterostructure. $\varepsilon^{s}_{x} = 0.1050$, right before the σ_Y point is reached.

direction, where the uniaxial tensile load is applied. These figures (all in scale) correlate with the beginning and the end of elastic deformation. During plastic deformation, as seen in figures C.1c to C.1f, this expansion along the thickness axis keeps occurring. That causes a NPR in the pristine AC G-Cu heterostructure. As it was already discussed in section 2.4, the NPR is a consequence of the surface effect, which was also detected in the pristine AC G-Cu heterostructure analyzed in this work (see figure 4.14). In the same section, it was also mentioned how the G-Cu interface creates new free boundaries, where the Cu atoms that are adjacent to graphene present high stress values and inner atoms present significantly lower ones for compensation. That can also be seen in figure 4.14. In the σ^{α}_{zz} distribution map (figure 4.14b), it can even be seen how almost all the inner Cu atoms present negative values, which means that they are under compression along the z-axis. As mentioned in section 2.4, the compression in the z-direction induces a NPR in the y-direction as a result

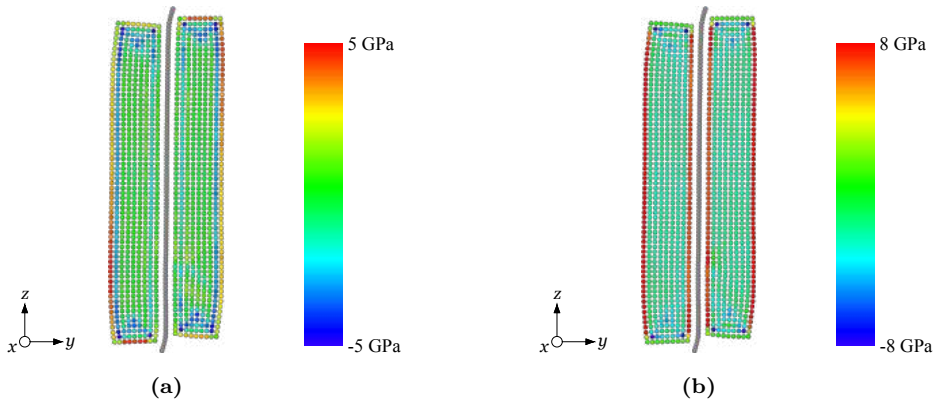

Figure 4.14: (a) σ^{α}_{yy} and (b) σ^{α}_{zz} distribution maps of the analyzed pristine AC G-Cu heterostructure at a selected central slice in the yz-plane. The maps were determined at a $\varepsilon^{s}_{x} = 0.1050$, where the specimen reaches its σ_Y point.

of branching. The Poisson's ratio values will be presented in subsection 4.3.3.

On the other hand, in the xz-plane the material behaves as a conventional material, that is, the z-dimension decreases while the x-dimension, the dimension along which the uniaxial tensile load is applied, increases. Moreover, necking is observed in the Cu layers (see figures C.1c and C.1d). It is noticeable, due to the high ductility of Cu, how these layers decrease much more in z-length compared to the graphene layer, which gets uncovered near the boundaries with the advance of stretching. The exposed graphene, due to LJ attractive interactions between C and Cu atoms, begins to wrap one of the Cu layers at higher ϵ_x^ss, as shown in figures C.1e and C.1f. At this point though, graphene is already experiencing failure (see figures C.2e and C.2f).

Figure C.2 displays only the graphene layer in the pristine AC G-Cu heterostructure. Here, Cu atoms were removed for a better observation of the nanocomposite's C atoms throughout the tensile test. It can be noted that the phase transformation discussed in subsection 4.1.1 also occurs when graphene is between two Cu films in a sandwich-like structure. However, the transition from a honeycomb to an orthorhombic lattice does not occur entirely like in a pure AC GNR under tensile stress. In the heterostructure, it is limited to a small portion of the graphene layer until the failure process starts (see figure C.2e). The interaction of the pristine AC graphene layer with the upper and lower Cu layers apparently affect the formation of larger shearing regions and, therefore, the phase transition is restricted. Nevertheless, after the fracture process starts in the heterostructure's AC graphene layer and these C atoms get practically unloaded, the atoms in the sheared region tend to go back to their original honeycomb lattice, like in the pure AC GNRs.

Regarding figures C.3 and C.5, the front and top views of the AC G-Cu heterostructure with vacancies and SW defects in the graphene layer are shown, respectively, at densities $\rho_{Vac} = \rho_{SW} = 0.03$ and different ε_x^ss during the tensile test. The atomic dynamics of defective G-Cu heterostructures is highly similar to the one of their pristine counterpart: dislocations form in the Cu layers during plastic deformation (see figures 4.15 and 4.16), also appearing firstly in the upper Cu layer. The thickness dimension expands resulting in a NPR as a consequence of the surface effect that can be seen in figures 4.17 and 4.18. The other transverse dimension does actually shrink exposing then part of the graphene layer, which begins to wrap the sides of the Cu layers due to LJ attractive interactions between C and Cu atoms.

Also, Cu atoms were removed for a better observation of the graphene layer in

defective G-Cu heterostructures during the tensile test. These snapshots are shown in figures

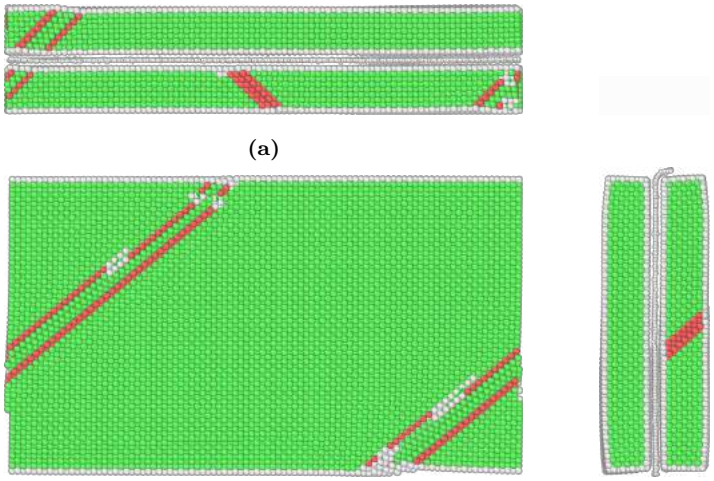

Figure 4.15: AC G-Cu heterostructure with vacancy density $\rho_{Vac} = 0.03$ in the graphene layer, at $\varepsilon_x^s = 0.1025$. Initial dislocations in the (a) xy-, (b) xz-, and (c) yz-planes can be seen. In (a) and (c), selected central slices of the overall heterostructure are shown. In (b), a selected central slice in the upper Cu layer is shown. Green atoms are arranged in the original FCC structure of Cu, red atoms in the hexagonal close packed (HCP), and the white atoms in other types of lattices. White atoms also represent those located at the free surfaces.

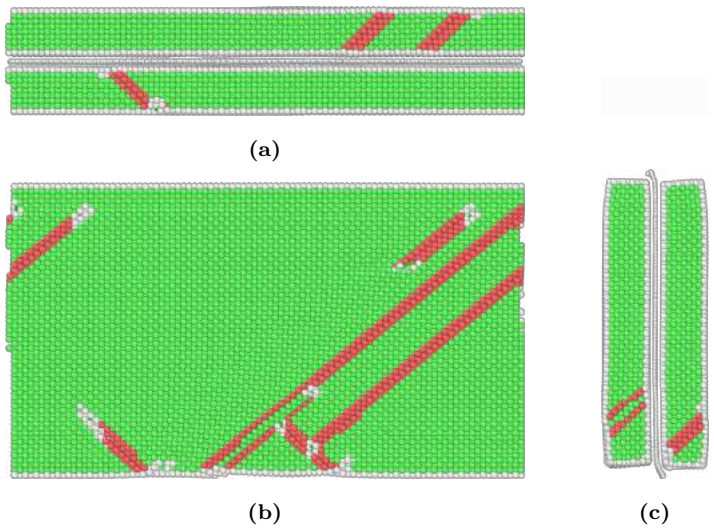

Figure 4.16: AC G-Cu heterostructure with SW density $\rho_{SW} = 0.03$ at $\varepsilon_x^s = 0.1070$. Initial dislocations in the (a) xy-, (b) xz-, and (c) yz-planes can be seen. In (a) and (c), selected central slices of the overall heterostructure are shown. In (b), a selected central slice in the upper Cu layer is shown. Green atoms are arranged in the original FCC structure of Cu, red atoms in the hexagonal close packed (HCP), and the white atoms in other types of lattices. White atoms also represent those located at the free surfaces.

C.4 and C.6. Here, the difference from the pristine graphene layer in the nanocomposite is that a phase transition does not occur at any point of the stretching in any region of the defective graphene layer. The hypothesis explaining why it is more difficult for the phase transition to take place in highly defective AC GNRs, specially when the defects are vacancies, was already discussed in subsection 4.1.1. Moreover, it can be noticed that the fracture of the AC graphene layer occurs completely only in the pristine case. When vacancies are present, two threads made up of C atoms, one on the top and one on the bottom, keep holding the two parts of the AC graphene layer with vacancies together, as shown in figure C.4f. When SW defects are present, more bonds along the fracture region

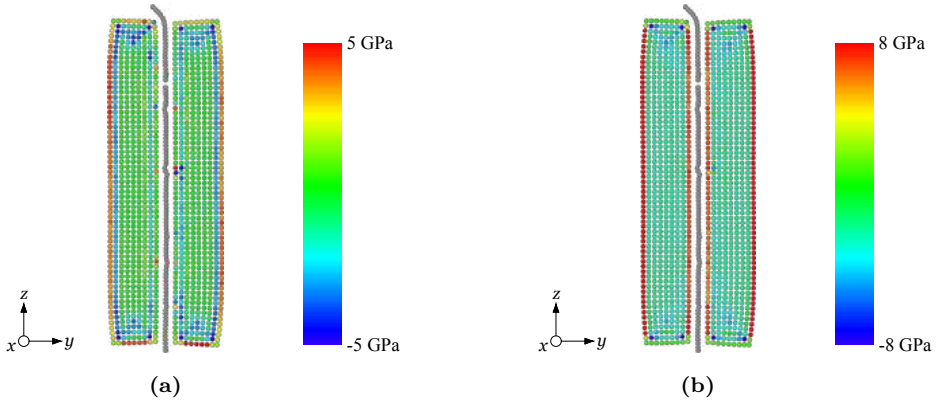

Figure 4.17: (a) σ^{α}_{yy} and (b) σ^{α}_{zz} distribution maps of the analyzed AC G-Cu heterostructure with vacancy density $\rho_{Vac} = 0.03$ in the graphene layer, at a selected central slice in the yz-plane. The maps were reproduced at a $\varepsilon^{s}_{x} = 0.1005$, right before the specimen reaches its σ_Y point.

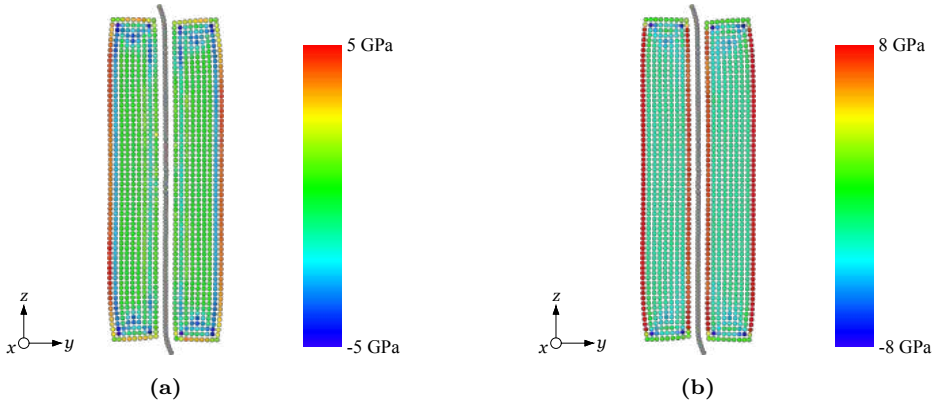

Figure 4.18: (a) σ^{α}_{yy} and (b) σ^{α}_{zz} distribution maps of the analyzed AC G-Cu heterostructure with SW density $\rho_{SW} = 0.03$ in the graphene layer, at a selected central slice in the yz-plane. The maps were reproduced at a $\varepsilon^{s}_{x} = 0.1050$, right before the specimen reaches its σ_Y point.

keep both pieces united (see figure C.6f). It was already shown in section 4.1 that defective graphene strained along the AC edge can be less brittle and, in some cases, even more ductile than its pristine counterpart.

Now, moving on to the G-Cu heterostructures where the graphene layer is strained along the ZZ edge, the snapshots of the tensile test performed with the pristine material are shown in figure C.7. Again, the atomic dynamics in the Cu layers is very similar to the one seen in the AC heterostructure: dislocations are formed during plastic deformation in a non-symmetric way, as portrayed in figure 4.19, also due to a non-symmetric σ^{α}_{xx} distribution during elastic deformation (see figure 4.20). Also, they appear firstly in the upper Cu layer, as it can be observed in figures 4.19a and 4.19c. The lower layer gets dislocations just a few steps after they begin to form in the upper one.

Furthermore, an expansion in thickness, or in the y-direction, is also observed. Just like in the pristine AC G-Cu system, the surface effect also occurs in the pristine ZZ one, as displayed in figure 4.21. Note that the σ^{α}_{yy} and σ^{α}_{zz} distributions in this case are very similar to the distributions of the pristine AC one. It can be seen that inner Cu atoms are mostly under compression along the z-axis, and that, as already discussed, induces a NPR along the y-axis.

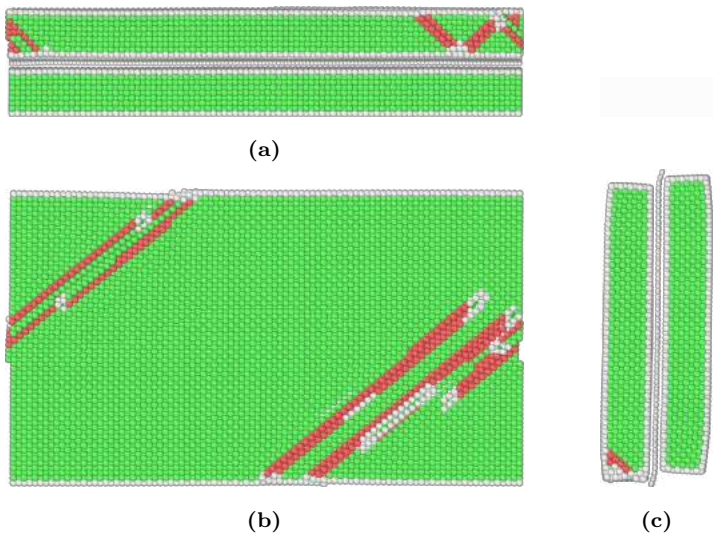

Figure 4.19: Pristine ZZ G-Cu heterostructure at $\varepsilon^{s}_{x} = 0.1125$, where initial dislocations in the (a) xy-, (b) xz-, and (c) yz-planes can be seen. In (a) and (c), selected central slices of the overall heterostructure are shown. In (b), a selected central slice in the upper Cu layer is shown. Green atoms are arranged in the original FCC structure of Cu, red atoms in the hexagonal close packed (HCP), and the white atoms in other types of lattices. White atoms also represent those located at the free surfaces.

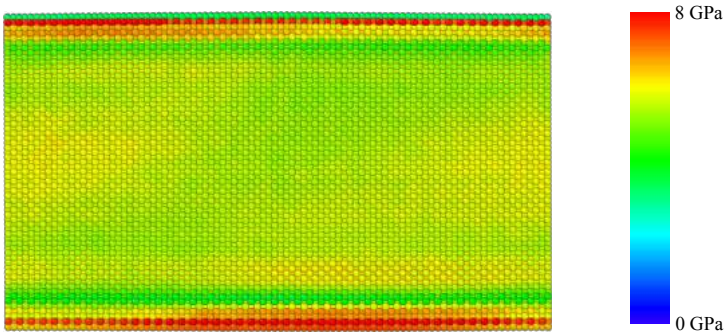

Figure 4.20: σ^{α}_{xx} distribution map at a selected central slice in the xz-plane of the upper Cu layer, in the pristine ZZ G-Cu heterostructure at a $\varepsilon^{s}_{x} = 0.1100$, right before the σ_Y point is reached.

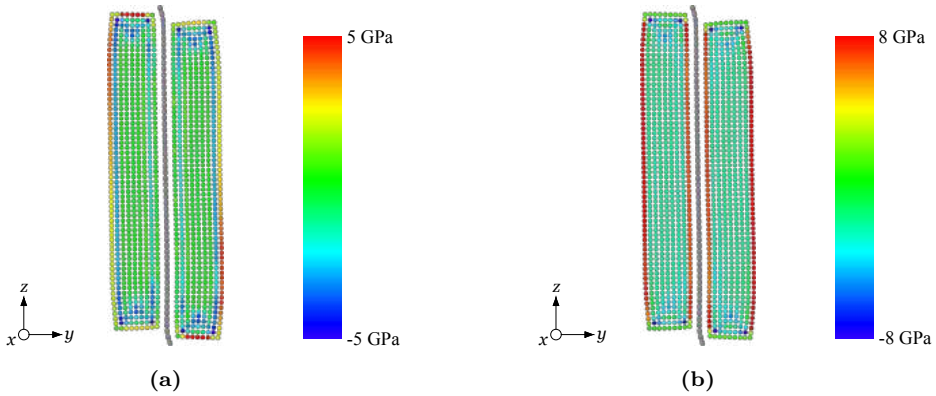

Figure 4.21: (a) σ^{α}_{yy} and (b) σ^{α}_{zz} distribution maps of the analyzed pristine ZZ G-Cu heterostructure at a selected central slice in the yz-plane. The maps were reproduced at $\varepsilon^{s}_{x} = 0.1100$, near the deformation where the specimen reaches its σ_Y point.

On the other hand, like the pristine AC G-Cu case, the z-dimension does shrink when this pristine ZZ heterostructure is being strained along the x-axis, as shown in figure C.7. Another similarity is the faster decrease of the z-dimension of the Cu layers compared to graphene layer. As a consequence, the graphene parts near the z borders also get exposed and start wrapping the sides of the Cu layers due to LJ attractive interactions between C and Cu atoms.

The evolution of the pristine ZZ graphene layer during the tensile test can be seen in figure C.8, where the Cu atoms were removed. ZZ graphene, as discussed in subsection 4.1.1, does not present a phase transformation when stretched to certain strain values. Also, compared to the graphene layer in the pristine AC G-Cu heterostructure, the layer in the pristine ZZ G-Cu begins fracturing at a larger ε^{s}_{x} value. This behavior will be reflected in the SSCs of the nanocomposites, which will be further discussed in the following subsection.

In Appendix C, the snapshots of the tensile tests performed in the ZZ G-Cu heterostructures, with vacancies and SW defects in the graphene layer at densities $\rho_{Vac} = \rho_{SW}$

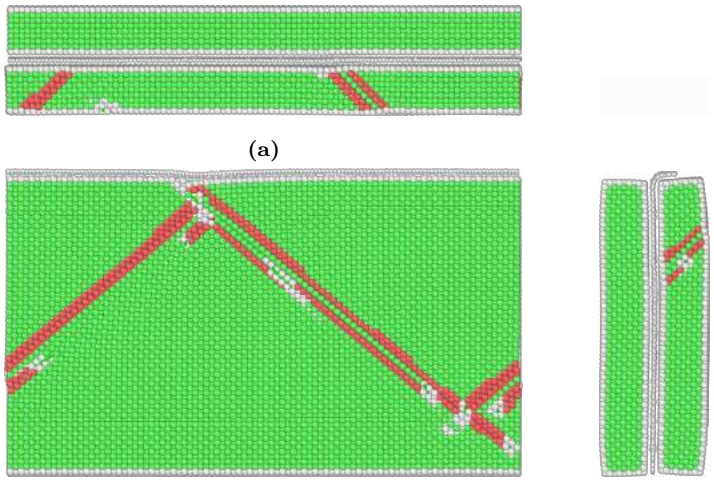

Figure 4.22: ZZ G-Cu heterostructure with vacancy density $\rho_{Vac} = 0.03$ in the graphene layer, at $\varepsilon_x^s = 0.1025$ where initial dislocations in the (a) xy-, (b) xz-, and (c) yz-planes can be seen. In (a) and (c), selected central slices of the overall heterostructure are shown. In (b), a selected central slice in the upper Cu layer is shown. Green atoms are arranged in the original FCC structure of Cu, red atoms in the hexagonal close packed (HCP), and the white atoms in other types of lattices. White atoms also represent those located at the free surfaces.

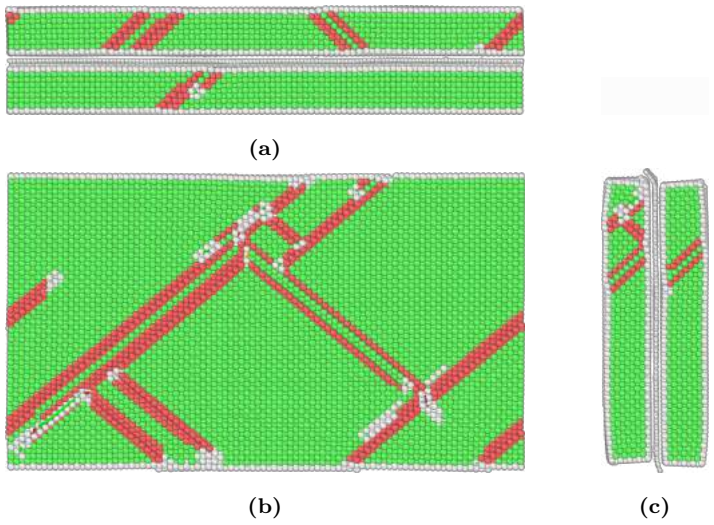

Figure 4.23: ZZ G-Cu heterostructure with SW density $\rho_{SW} = 0.03$, at $\varepsilon_x^s = 0.1090$ where initial dislocations in the (a) xy-, (b) xz-, and (c) yz-planes can be seen. In (a) and (c), selected central slices of the overall heterostructure are shown. In (b), a selected central slice in the upper Cu layer is shown. Green atoms are arranged in the original FCC structure of Cu, red atoms in the hexagonal close packed (HCP), and the white atoms in other types of lattices. White atoms also represent those located at the free surfaces.

= 0.03, are shown in figures C.9 and C.11. Again, the atomic dynamics here do not differ significantly from the above discussed cases: non-symmetrical dislocations still form in the Cu layers during plastic deformation (see figures 4.22 and 4.23), appearing firstly in one of the Cu layers, and after a couple of steps in the other one; an increase in the y-dimension also happens due to a surface effect that, as already mentioned, induces Cu atoms on the free surfaces, as well as the ones adjacent to the graphene layer, to have high σ^{α}_{yy} and σ^{α}_{zz} values, while the inner Cu atoms present significantly lower stresses for compensation, specially the z component where negative values are reached (see figures 4.24 and 4.25), which means that these atoms are under compression along the z-axis, and, as a consequence, a NPR is observed along the y-axis. In contrast, the z-dimension decreases throughout the

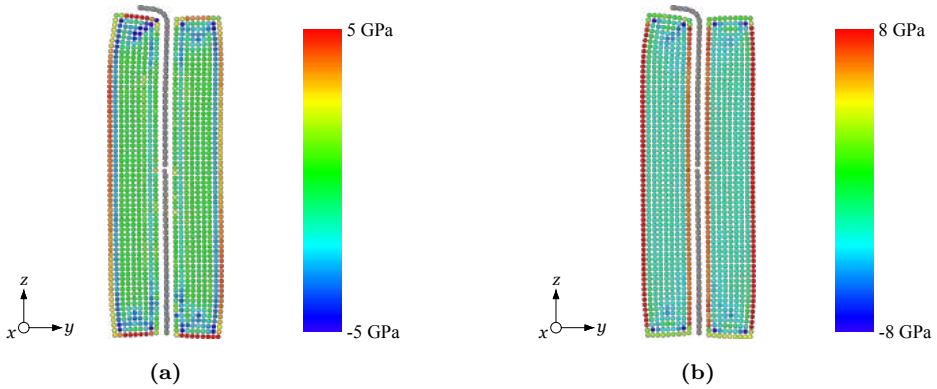

Figure 4.24: (a) σ^{α}_{yy} and (b) σ^{α}_{zz} distribution maps of the analyzed ZZ G-Cu heterostructure with vacancy density $\rho_{Vac} = 0.03$ in the graphene layer, at a selected central slice in the yz-plane. The maps were reproduced at $\varepsilon^{s}_{x} = 0.1005$, right before the specimen reaches its σ_Y point.

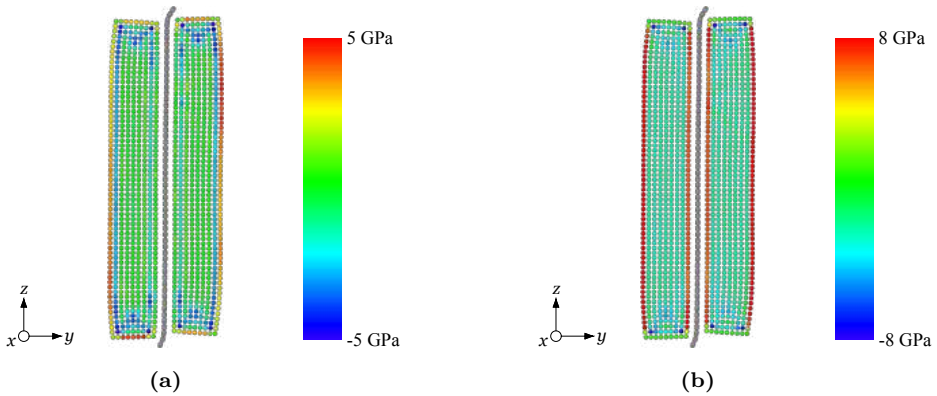

Figure 4.25: (a) σ^{α}_{yy} and (b) σ^{α}_{zz} distribution maps of the analyzed ZZ G-Cu heterostructure with SW density $\rho_{SW} = 0.03$ in the graphene layer, at a selected central slice in the yz-plane. The maps were reproduced at $\varepsilon^{s}_{x} = 0.1050$, right before the specimen reaches its σ_Y point.

tensile test with a more rapid decrease being observed in the Cu layers and, consequently, parts of the graphene layer get exposed near the z-boundaries. These exposed parts begin to wrap the sides of the Cu layers due to attractive LJ interactions between C and Cu atoms, as mentioned before.

For a better visualization of the graphene layers with the given defects density, see figures C.10 and C.12. There, the Cu atoms were removed. When compared to the graphene layer in the pristine structure (figure C.8), it can be noted that the fracture is more advanced in the defective cases at $\varepsilon_x^s = 0.4000$, specially in the presence of SW defects. In this case, only a few bonds in the fracture region are holding the two pieces of the graphene layer together. The opposite was observed in the pristine and defective AC G-Cu heterostructures. There, the defective graphene layers still had a few bonds holding its two parts together at a ε_x^s value of 0.3700 while, at this point, the pristine AC graphene layer was already broken apart.

In the following subsection, we discuss how all the results mentioned above are reflected in the SSCs of all the analyzed G-Cu heterostructures.

4.3.2 Stress-Strain Curve and Young's Modulus

Figure 4.26 shows the SSCs of all the G-Cu nanosystems analyzed in this work. Curves with squares were obtained for the AC systems (figures 4.26a and 4.26b), while the ones with diamonds for the ZZ ones (figures 4.26c and 4.26d). Also, all the black curves correspond to pristine systems, whereas the colored ones to the defective cases. The SSC of the analyzed pure Cu nanofilm, which is the orange curve with triangles, is included in all graphs for comparison.

First, the SSC of the pristine AC G-Cu heterostructure and those with vacancies at different ρ_{Vac} values are compared in figure 4.26a. In the elastic region, it can be seen that the pristine system, as expected, is able to sustain higher σ_{xx}^s at given ε_x^s values, and the higher ρ_{Vac}, the lesser the load the material handles during elastic deformation. That will induce a decrease in E: the more vacancies the AC graphene layer has, the lower the modulus will be. Furthermore, the pristine system has the highest σ_Y value, which decreases with increasing ρ_{Vac}. In other words, the less vacancies the graphene layer in AC G-Cu heterostructures has, the more stress the system can sustain before its SSC enters the plastic region. Moreover, the elastic to plastic deformation transition strain, that is, $\varepsilon(\sigma_Y)$

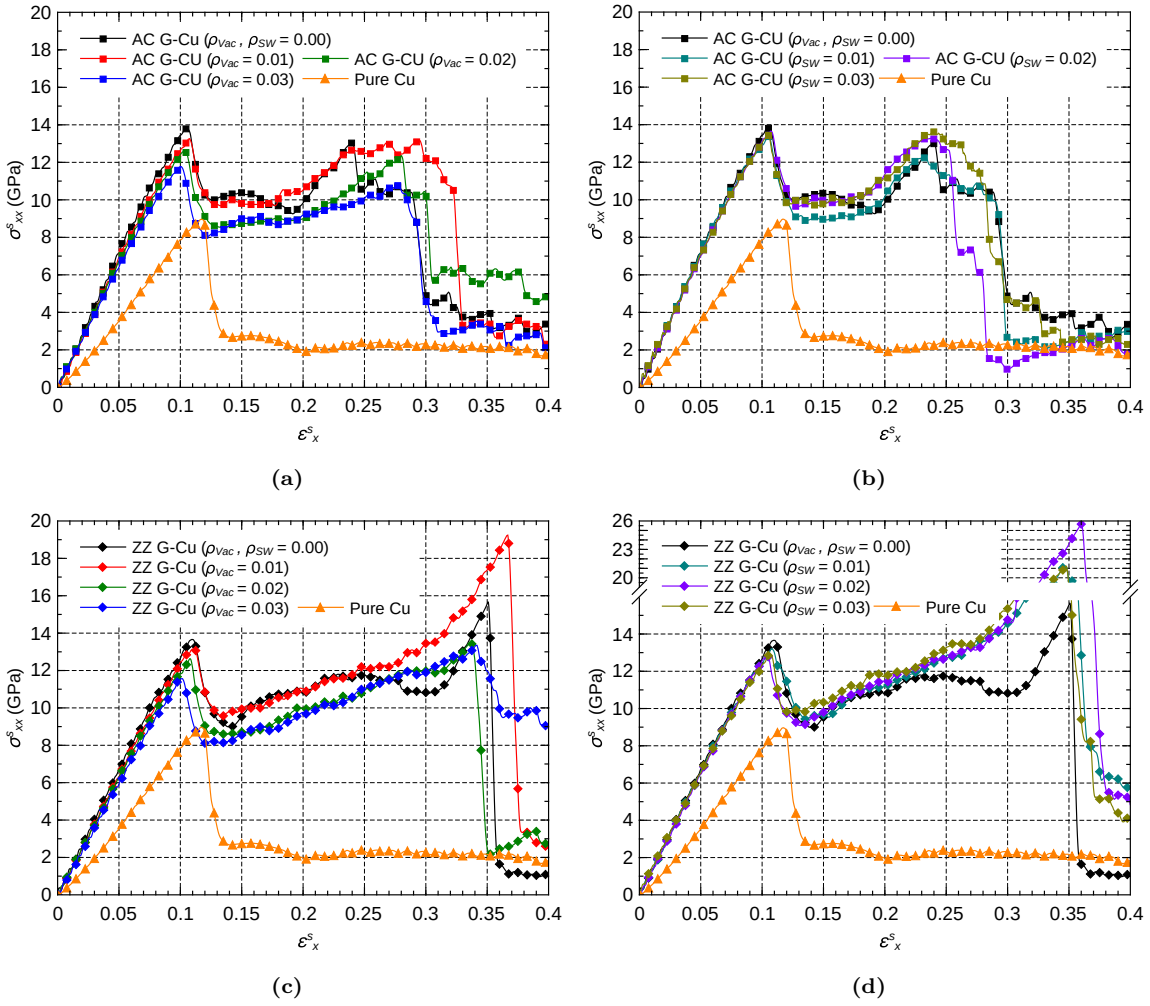

Figure 4.26: SSCs of the analyzed G-Cu nanocomposites: (a) and (b) AC G-Cu heterostructure at different densities of vacancy and SW defects in the graphene layer, respectively, (c) and (d) same for ZZ G-Cu heterostructure, respectively.

of the defective systems is also lower than that of the pristine system, with the exception of the AC G-Cu heterostructure with vacancy density $\rho_{Vac} = 0.01$, which presents a slightly higher $\varepsilon(\sigma_Y)$ value and, consequently, is more elastic. E, σ_Y, and $\varepsilon(\sigma_Y)$ values are displayed in table 4.2.

In the plastic region, the lower-yield points also happen to be at lower σ^s_{xx} values for larger ρ_{Vac}s. They are found at lower ε^s_x values as well. In average, during plastic deformation AC G-Cu heterostructures with vacancies in the graphene layer sustain lower σ^s_{xx} than the pristine one. However and surprisingly, the σ_{TS} points of the defective systems

are at higher ε_x^s than the pristine one, the system with $\rho_{Vac} = 0.01$ being found at the highest strain. As for ε_F, that is, the strain at which the material fails, has also higher values than that of the pristine system. It implies that vacancies at such densities in the graphene layer of an AC G-Cu heterostructure make this material more ductile. Nevertheless, the σ_{TS} point of the pristine system is at higher σ_{xx}^s than those with vacancies at ρ_{Vac} values of 0.02 and 0.03. The system with $\rho_{Vac} = 0.01$ presents a slightly higher σ_{TS} than the pristine one. Thus, it can be concluded that an AC G-Cu heterostructure with vacancy density $\rho_{Vac} = 0.01$ is the toughest and more ductile of all, including the pristine one. In other words, it presents the best mechanical behavior during plastic deformation. σ_{TS} and ε_F for all analyzed systems are also displayed in table 4.2, where a general trend can be observed, except for the above mentioned cases indicating that a different regime might occur around those densities.

The behavior mentioned above was also observed in the analyzed pure AC GNRs

Table 4.2: Estimated E, σ_Y, $\varepsilon(\sigma_Y)$, σ_{TS}, and ε_F values of AC and ZZ G-Cu heterostructures at different defect densities.

Chirality	Defect type	Density of defects	E (GPa)	σ_Y (GPa)	$\varepsilon(\sigma_Y)$	σ_{TS} (GPa)	ε_F
AC	No defects	0.00	148.4	13.882	0.1050	13.063	0.2889
	Vacancy	0.01	140.3	13.382	0.1083	13.253	0.3230
		0.02	132.8	12.683	0.1045	12.491	0.2998
		0.03	128.0	11.802	0.1003	10.824	0.2843
	Stone-Wales	0.01	144.1	13.372	0.1052	12.310	0.2910
		0.02	140.8	13.718	0.1075	13.317	0.2529
		0.03	138.6	13.452	0.1051	13.511	0.2768
ZZ	No defects	0.00	134.2	13.721	0.1103	15.846	0.3518
	Vacancy	0.01	130.2	13.194	0.1123	19.371	0.3676
		0.02	126.9	12.818	0.1079	13.572	0.3371
		0.03	120.3	11.640	0.1015	13.440	0.3422
	Stone-Wales	0.01	132.2	13.280	0.1076	21.367	0.3465
		0.02	131.9	12.915	0.1042	25.826	0.3609
		0.03	129.6	12.933	0.1071	21.474	0.3486

(subsection 4.1.2), where some of the defective systems also presented improved ductility. Thus, this effect is seen reflected in the heterostructure, although more evidently.

The SSCs of the AC G-Cu heterostructures with SW defects in the graphene layer at different ρ_{SW} are shown in figure 4.26b. The SSC of the pristine system is also included for comparison. During elastic deformation, it can be seen that the defective systems sustain less load than the pristine one at same ε_x^s values, like the AC G-Cu heterostructures with vacancies, as discussed above. Therefore, it is also expected a decrease in E with an increase in ρ_{SW}. However, SW defects do not affect the elastic deformation of the AC G-Cu heterostructures as much as vacancies do, as it can be noted in the SSCs. Also, as shown in table 4.2, E values are more affected by the presence of vacancies than by SW defects. The same behavior was observed in pure AC GNRs, as mentioned in subsection 4.1.2. Furthermore, a slight decrease in σ_Y was found in defective systems, $\rho_{SW} = 0.01$ having the lowest one (see table 4.2). $\varepsilon(\sigma_Y)$ of the defective systems were all slightly higher than for the pristine system, which means that SW defects make the AC heterostructures slightly more elastic than the pristine one.

In the plastic region of the SSCs shown in figure 4.26b, it can also be seen that the AC G-Cu heterostructures with SW defects present their lowest yield point at lower σ_{xx}^s than the pristine one. Interestingly, the σ_{TS} value obtained in this case, at ρ_{SW} values of 0.02 and 0.03, were slightly higher than the one of the pristine system. They also appear around the same ε_x^s as in the pristine. In other words, the defective systems with SW defects at the mentioned ρ_{SW} values are actually tougher than the pristine one. On the other hand, the heterostructure with $\rho_{SW} = 0.01$ presented the lowest σ_{TS}. That is, at this ρ_{SW} the defective system is indeed less tough than the pristine one. In addition, differently from the result observed in AC G-Cu heterostructures with vacancies, for SW defects ε_F is reached at lower ε_x^s values compared to the pristine system except for $\rho_{SW} = 0.01$. In this case, ε_F is comparable to that of the pristine system. From there, the more SW defects the AC graphene layer has, the lower ε_F is. Therefore, here the defective systems did not turn out to be more ductile than the pristine one, in contrast to the case of vacancies.

Now, for both ZZ and AC G-Cu heterostructures the same behavior is observed in the elastic region of their SSCs. In figure 4.26c, the curve of the ZZ pristine system is compared with those of the ZZ systems with vacancies at different densities ρ_{Vac}. The defective systems again sustain less load than the pristine one at same ε_x^s values, and the higher ρ_{Vac} is, a lower σ_{xx}^ss are sustained. As already mentioned, this induces a decrease

in E, and, consequently, the material's stiffness is affected. Their values, as well as other calculated parameters, can be seen in table 4.2. A decrease in σ_Y is also observed as ρ_{Vac} increases. Moreover, the σ_Y values are very similar to those of the AC system, being just slightly smaller in most cases. Only σ_Y turned out to be slightly higher than that of the AC G-Cu heterostructure at the same $\rho_{Vac} = 0.02$. Nonetheless, the σ_Y point of both pristine and vacancy defective ZZ G-Cu nanocomposites are positioned at higher ε_x^s than their AC counterparts, that is, they show higher $\varepsilon(\sigma_Y)$. Consequently, the ZZ pristine systems are more elastic than the AC ones. In other words, they can be stretched more before they begin to deform plastically.

In the plastic region, it can be noticed from picture 4.26c that the defective ZZ systems with vacancies at $\rho_{Vac} = 0.02$ and 0.03 sustain lower σ_{xx}^s values than the pristine in almost all ε_x^s values between the σ_Y and σ_{TS} points. Only in a small range, between approximately 0.2750 and 0.0325, they sustain more load than the pristine system. However, the heterostructure at a $\rho_{Vac} = 0.01$, sustains more or less the same amount of load than the pristine nanocomposite at pretty much the entire range of ε_x^s during plastic deformation. Moreover, and surprisingly, it can also sustain more load than the pristine system before fracture, having a σ_{TS} value considerably higher than all the other analyzed systems at higher ρ_{Vac}s. It also presents the highest ε_F, fracturing at a higher deformation. Therefore, the system with SW defects at a $\rho_{Vac} = 0.01$ is more ductile and tougher than the pristine one as well as the other ones with vacancies. The parameters mentioned above are displayed in table 4.2.

Furthermore, as it can be seen in figure 4.26d, when the defects are 5-7-7-5 SW pairs, the same observation about the elastic region of the SSCs can be made: the higher ρ_{SW} is, the lower the E. In other words, the pristine ZZ G-Cu heterostructure is stiffer than those they have, the less stiff they are. Also, a decrease in σ_Y can be observed, except for $\rho_{SW} = 0.03$, where it is slightly higher than at $\rho_{SW} = 0.02$. For this chirality, the systems with SW defects tend to be more elastic than their AC counterparts (see $\varepsilon(\sigma_Y)$ values in table 4.2). Only at $\rho_{SW} = 0.02$, they posses a lower $\varepsilon(\sigma_Y)$ at the same ρ_{SW}. It can also be noted that SW defects do not affect the elastic behavior as much as vacancies do.

On the other hand, in the plastic region these heterostructures surprisingly sustain more load than the pristine one after their lower-yield point is reached, the one with SW density $\rho_{SW} = 0.03$ in fact sustaining the highest σ_{xx}^s, followed by the ones with ρ_{SW} values of 0.02 and 0.01. In the interval of ε_x^s between approximately 0.1200 and 0.2300,

the difference between the sustained stresses is not so large. Later, however, this difference begins to increase significantly, and all of the defective systems reach their σ_{TS} point at a much higher σ^s_{xx} than the pristine one. The defective system at $\rho_{SW} = 0.02$ is the one with the highest σ_{TS}, which is more than 10 GPa higher than the one found for the pristine nanocomposite. It also presents the highest ε_F. In conclusion, it can be said that the ZZ G-Cu heterostructures with SW defects in the graphene layer are tougher than the pristine system since they can bare more load before fracturing. Also, the composite with SW density $\rho_{SW} = 0.02$ is the toughest and more ductile since it possesses the highest ε_F. The values of these parameters can be seen in table 4.2 as well.

After the analysis of all heterostructures, it can be concluded that the pristine AC system is the stiffest one, presenting the highest E value as it can be seen in figure 4.27. It also presents the highest σ_Y (see table 4.2). Nonetheless, the ZZ system with SW defects in the graphene layer at $\rho_{SW} = 0.02$ is the toughest and the most ductile. In general, AC systems, including the pristine and defective ones, are stiffer than the ZZ ones. On the other hand, ZZ systems are more elastic, ductile and tougher than the AC ones.

Furthermore, in figure 4.27 it can also be observed how E decreases accordingly to the type, density of defects and the chirality of the graphene layer. The presented graph supports the fact that vacancies in the graphene layer affect the stiffness of G-Cu heterostructures more than SW defects. Higher stiffness of the AC G-Cu nanocomposites can also be noted. The same observations were made in the analyzed pure GNRs (subsection 4.1.2), and thus it is reflected in the G-Cu heterostructures.

Moreover, from the snapshots of the tensile tests performed in all the G-Cu heterostructures and their graphene layers shown in Appendix C (figures from C.1 to C.12), it can be observed that the fracture process begins in the graphene layers first. Due to the high ductility of Cu, the layers compound by this element do not reach their failure point in the range of ε^s_x values set in the MD simulations realized in this work. That is reflected in the SSCs presented in this subsection. In almost all curves, when the ε_F point is reached (which is around where the graphene layer starts fracturing), a sudden and substantial drop in σ^s_{xx} values is observed, although null values are never reached. Instead, the curves drop to a minimum and a plateau that stays approximately around 1 to 6 GPa σ^s_{xx} values, depending on the chirality, defect type, and density of defects. Here, since the graphene layers have already reached the maximum stress values they can sustain after they begin to fail, only the Cu layers are now absorbing all the load. It was already shown in subsections

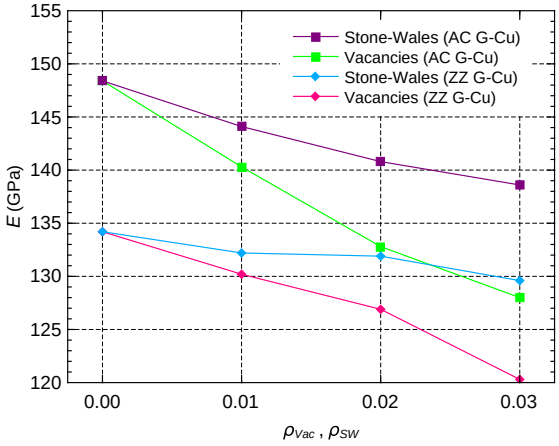

Figure 4.27: E values of AC and ZZ G-Cu heterostructures at different densities of defects. Note that AC systems are stiffer and that vacancies have a bigger impact in E.

4.1.2 and 4.2.2 that graphene can handle much higher tensile stresses than Cu. Therefore, in a G-Cu heterostructure the graphene layer is the one that bares most of the applied uniaxial tensile load, and once it is broken and the Cu layers are the only ones handling all the load, the stress sustained drops significantly. Also, the fact that the graphene layer sustains much of the stress in G-Cu nanocomposites explains the higher stiffness of AC systems compared to the ZZ ones, as well as the higher effect vacancies have than the SW defects in the mechanical properties of such materials, because the exact same behavior is observed in pure graphene, as discussed in subsection 4.1.2.

Note that the SSC of the analyzed pure Cu nanofilm was also included in the graphs shown in figure 4.26 for a better comparison with the SSCs of the G-Cu heterostructures. It can be observed that, no matter the chirality and the density of defects used in this work, a pure Cu nanofilm of comparable dimensions to the dimensions of the nanocomposite never reaches the same σ_Y and σ_{TS} values of the G-Cu heterostructures. Here, the strengthening mechanism is confirmed. The nanocomposites can sustain higher σ^s_{xx} before they begin to deform plastically and before their fracture process starts to take place. Moreover, stiffness is also improved in the G-Cu heterostructures. All the estimated E values were higher than that of the pure Cu nanofilm, which, as mentioned in subsection 4.2.2, was 81.39 GPa. The minimum value estimated for the G-Cu systems, found for the ZZ chirality at $\rho_{Vac} = 0.03$, was significantly higher, at 120.3 GPa. However, the pure Cu nanofilm turned out to be more elastic than the heterostructures, with a $\varepsilon(\sigma_Y) = 0.1169$, while the maximum found

for the nanocomposite was 0.1123 in the ZZ G-Cu heterostructure with vacancies at ρ_{Vac} = 0.01. It can also be said that pure Cu is more ductile than the nanocomposites since, after the graphene layer within them brakes, Cu itself is the component sustaining all the load at higher ε_x^s values.

In the next subsection, the results regarding the Poisson's ratio of the analyzed G-Cu heterostructures are presented and discussed. A comparison with the pure Cu nanofilm is done.

4.3.3 Poisson's Ratio

In figure 4.28, the calculated ν_{xy}^s values at ε_x^s between 0.0100 and 0.2000 for all the analyzed G-Cu heterostructures are shown. Black curves represent the results found for the pristine systems while colored ones the defective systems at different ρ_{Vac}s and ρ_{SW}s. Also, curves with squares (diamonds) represent the results obtained for the nanocomposites where the graphene layer is strained along the AC (ZZ) edge. The ratios obtained for the pure Cu nanofilm are also included in all graphs for comparison. They are represented by the orange curve with triangles.

The dependence of AC heterostructures ν_{xy}^s on ρ_{Vac} can be observed in figure 4.28a. It can be seen that in the beginning of the tensile test, at earlier ε_x^ss, the defective systems present higher ν_{xy}^s than the pristine one. Note that at the first steps of stretching the more vacancies the graphene layer in AC G-Cu heterostructures has, the higher ν_{xy}^s is. At $\varepsilon_x^s \approx 0.0550$, the difference between ν_{xy}^s becomes minimal,for the pristine and defective AC systems. This behavior continues until $\varepsilon_x^s \approx 0.0950$. From this point, the pristine now presents the highest ν_{xy}^s. Furthermore, a NPR is observed after a $\varepsilon_x^s \approx 0.0900$, which, as it can be seen in figure 4.26a, is located in the elastic region of the SSCs. Therefore, the pristine AC G-Cu heterostructure, as well as the ones with vacancies in the graphene layer, present a NPR along the y-axis before the material begins to deform plastically.

Similarly, when the defects are 5-7-7-5 SW pairs, the systems show higher ν_{xy}^s values than the pristine at earlier ε_x^s, as it can be observed in figure 4.28b. The difference becomes less and less until the range of ε_x^s between 0.0700 and 0.0950 is reached, where all the ν_{xy}^s values of the pristine and defective AC G-Cu heterostructures at different densities are similar. This range is shorter than the one found for vacancies. Past this range, the behavior switches, such that the pristine presents the highest ν_{xy}^s. Also, NPR is observed

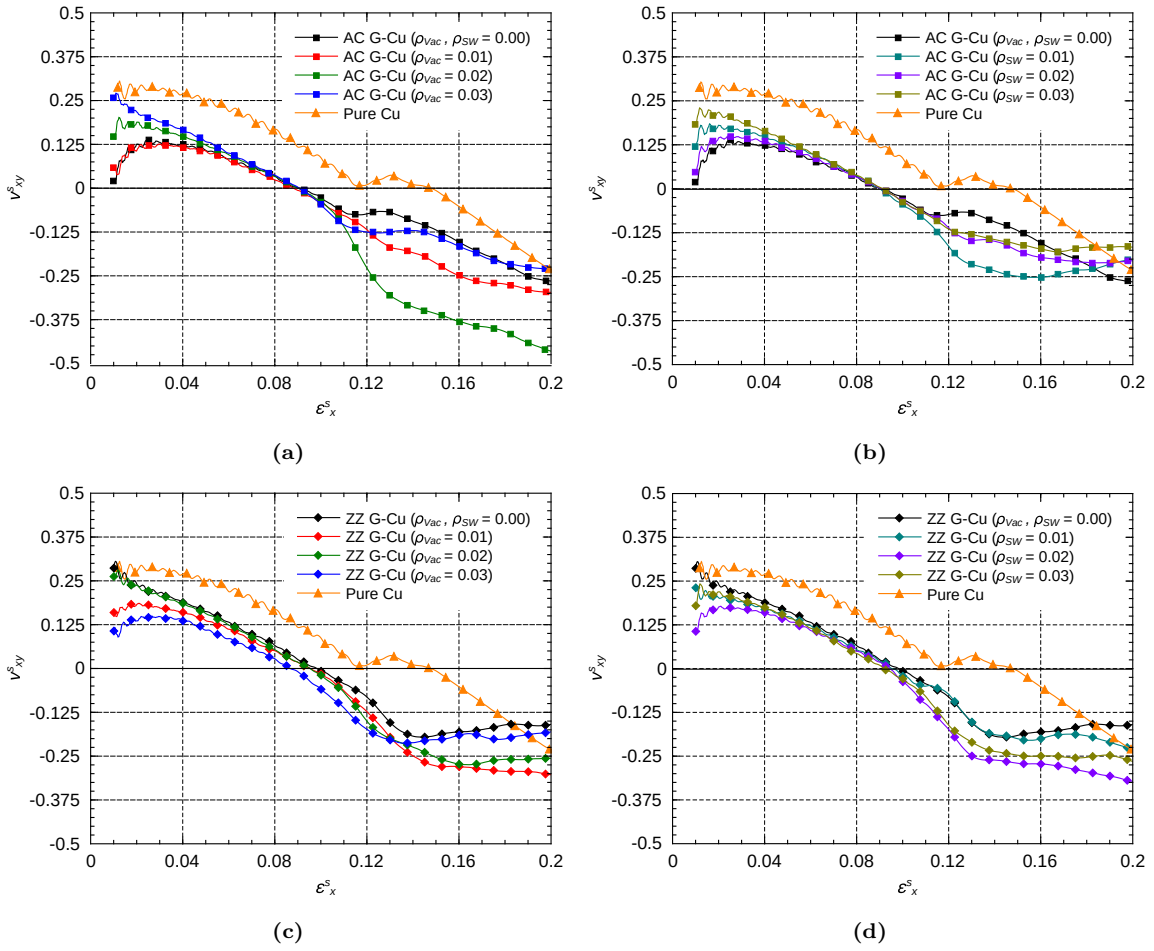

Figure 4.28: ν^s_{xy} at different ε^s_xs of the analyzed G-Cu nanocomposites: (a) and (b) AC G-Cu heterostructure at different densities of vacancy and SW defects in the graphene layer, respectively, and (c) and (d) same for ZZ G-Cu heterostructure.

in these curves while the material is still deforming elastically (see figure 4.26b). Here, the PPR to NPR transition point also occurs at a $\varepsilon^s_x \approx 0.0900$.

Now, for the ZZ chirality, the behavior of the $\nu^s_{xy} \times \varepsilon^s_x$ curves is slightly different. It can be seen, from figure 4.28c, that when vacancies are present, no matter the density, ν^s_{xy} values are lower than, or very close to, those of the pristine system in pretty much all ε^s_x range considered here. There is not a significant region where they take higher values, as it occurs with the AC G-Cu heterostructures. The same happens for 5-7-7-5 SW pairs (see figure 4.28d). Also, the pristine system begin to present a NPR at a higher ε^s_x value than the defective ones. ν^s_{xy} becomes negative at approximately 0.0950 when there are no

defects, and the higher ρ_{Vac} and ρ_{SW} are, earlier the ZZ G-Cu heterostructure presents a NPR. This is more evident in the presence of vacancies at $\rho_{Vac} = 0.03$. As mentioned above, all the analyzed AC G-Cu nanocomposites present a NPR around the same ε_x^s.

It can be observed that, on the contrary of what is seen in all the analyzed G-Cu heterostructures, in the pure Cu nanofilm a NPR along the y-axis is reached when the material is already deep into plastic deformation (compare pictures 4.10 and 4.11). As it was already discussed, the addition of a graphene sheet inside a Cu nanofilm creates what can be considered two new surfaces. Moreover, the Cu layers in the heterostructures are thinner than the pure Cu nanofilm. The movement of Cu atoms in a G-Cu system is more easily driven by the surface atoms with high tensile stresses since the influence of surface effect on the Poisson's ratio can be more significant the thinner Cu films get.[5,67]

The NPR found in the G-Cu nanocomposites is also a consequence of the above discussed surface effect, which can be observed in figures 4.14, 4.17, 4.18, 4.21, 4.24, and 4.25. To understand the differences on ν_{xy}^s values between the pristine and defective AC systems, the stress distribution in the Cu surface adjacent to the graphene layer, where Cu atoms present high tensile stresses along the z-axis, is analyzed. In figure 4.29, σ_{yy}^{α} and σ_{zz}^{α} distribution maps of the Cu atoms adjacent to the graphene layer of pristine and defective AC systems are shown. Note that the σ_{yy}^{α} distribution is very uniform in the pristine AC systems (see figure 4.29a), and most Cu atoms at the G-Cu interface have $\sigma_{yy}^{\alpha} \approx 0$. However, when the graphene layer has vacancies (figure 4.29c), many individual Cu atoms around the defects present higher or lower stresses. The same effect, although noticeably less apparent, is also observed in the presence of SW defects (see figure 4.29e). On the other hand, the σ_{zz}^{α} distribution is not as affected as the σ_{yy}^{α} one, as it can be seen in figures 4.29b, 4.29d, and 4.29f. However, a higher uniformity can still be seen in the pristine AC G-Cu heterostructure.

As it can be observed in figure 4.30, the σ_{yy}^{α} and σ_{zz}^{α} distributions in the pristine ZZ system is basically affected in the same way the AC system is by vacancies and SW defects. In the pristine ZZ system, uniformity in the σ_{yy}^{α} and σ_{zz}^{α} distributions is also observed in figures 4.30a and 4.30b, respectively. On the other hand, this uniformity is compromised in the ZZ systems with vacancies (see figures 4.30c and 4.30d) and SW defects (see figures 4.30e and 4.30f).

Since the Poisson's ratio is correlated to the surface effect, and the latter one related to the distribution of the y- and z-components of the atomic stresses, when that

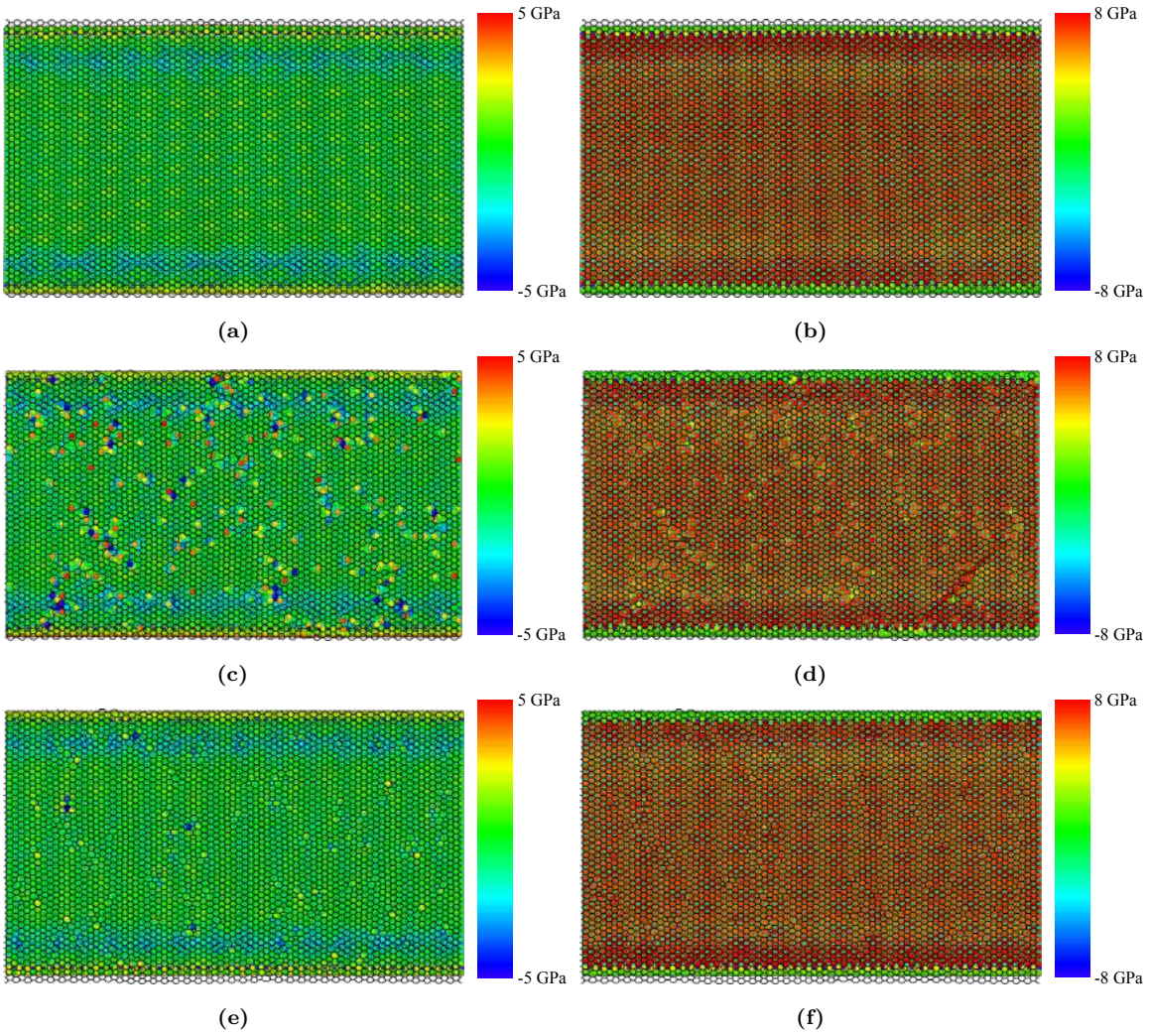

Figure 4.29: Stress distribution maps for the AC G-Cu heterostructures. (a) σ^{α}_{yy} and (b) σ^{α}_{zz} distribution maps of Cu atoms adjacent to the graphene layer in the pristine case at $\varepsilon^{s}_{x} = 0.1050$. (c) and (d) idem for Cu atoms adjacent to the graphene layer with vacancy density $\rho_{Vac} = 0.03$ at $\varepsilon^{s}_{x} = 0.1005$. (e) and (f) idem for Cu atoms adjacent to the graphene layer with SW defects with density $\rho_{SW} = 0.03$ at $\varepsilon^{s}_{x} = 0.1050$. The C-C bonds in the graphene layer are shown in all figures to locate the defects, when they are present. Also, all the pictures shown were taken around the σ_Y point of the material.

configuration is changed from an uniform to a more complex distribution, the Poisson's ratio will be affected by, for example, defects. The result is shown in figure 4.28, where the pristine and defective G-Cu systems present different ν^{s}_{xy} values depending on ε^{s}_{x}. It can also be noted that vacancies affect ν^{s}_{xy} more than SW defects. That is reflected in the distribution maps of the y- and z-components of the stress (figures 4.29 and 4.30), where it is noticeable the way vacancies affect much more the uniformity of the distribution.

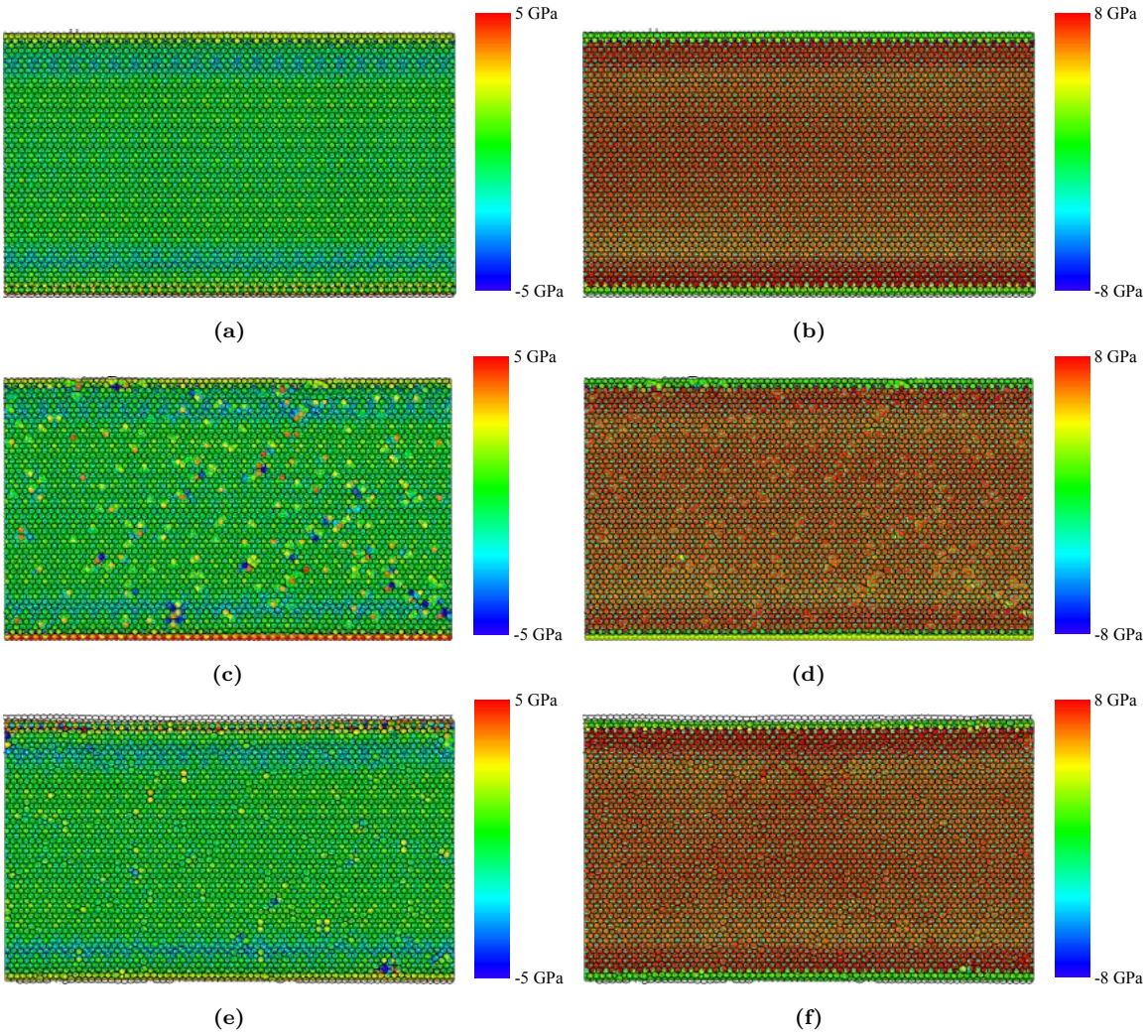

Figure 4.30: Stress distribution maps for the ZZ G-Cu heterostructures. (a) σ^{α}_{yy} and (b) σ^{α}_{zz} distribution maps of Cu atoms adjacent to the graphene layer in the pristine case at $\varepsilon^{s}_{x} = 0.1100$. (c) and (d) idem for Cu atoms adjacent to the graphene layer with vacancy density $\rho_{Vac} = 0.03$ at $\varepsilon^{s}_{x} = 0.1005$. (e) and (f) idem for Cu atoms adjacent to the graphene layer with SW defects with density $\rho_{SW} = 0.03$ at $\varepsilon^{s}_{x} = 0.1070$. The C-C bonds in the graphene layer are shown in all figures to locate the defects, when they are present. Also, all the pictures shown were taken around the σ_Y point of the material.

To finalize, the results for the Poisson's ratio along the z-direction, that is, the ν^{s}_{xz} values, are presented in figure 4.31. Here, the color and line symbol scheme used is the same as before, but dotted lines are used instead. Also, ν^{s}_{xz} curves of pure Cu nanofilm are also included in all graphs for comparison. Note that, along the z-direction, the nanocomposites behave as conventional materials, that is, they do not present a NPR at any ε^{s}_{x} range. If all the graphs in this figure are compared to their correlative ones in figure 4.28, at which

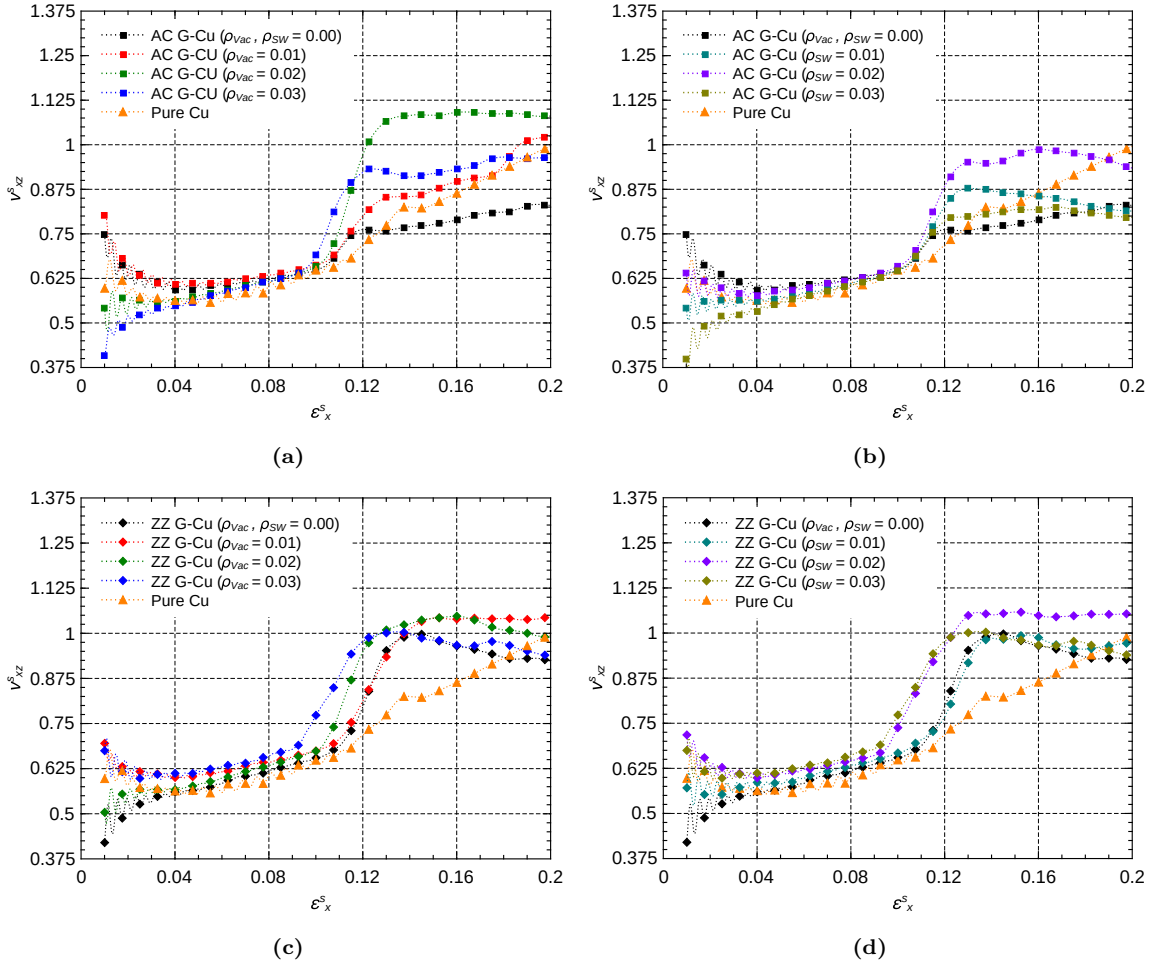

Figure 4.31: ν^s_{xz} values at different ε^s_xs of the analyzed pure G-Cu nanocomposites: (a) and (b) AC at different densities of vacancy and SW densities, respectively, (c) and (d) similar for the ZZ chirality.

ν^s_{xy} values of all the G-Cu heterostructure are displayed, it can be said that ν^s_{xz} basically mirrors ν^s_{xy}. Therefore, similarly to the pure Cu nanofilm, branching is also observed in all nanocomposites, regardless the chirality or density of defects. In conclusion, the increased surface effect in sandwich-like G-Cu systems plays a key role on the occurrence of a NPR along the thickness direction, which is along the y-axis, as well as branching on the other transverse direction, which corresponds to the z-axis.

With that, all the results obtained from the MD simulations conducted in this work are already shown and discussed. In the next chapter, we present the conclusions of our study.

Chapter 5

Conclusions

Molecular dynamics simulations of tensile tests were performed to study the role defects play, particularly vacancies and Stone-Wales in graphene, on the mechanical properties of sandwich-like graphene-copper heterostructures at the nanoscale. The stress-strain curves at different densities of defects were obtained. Both defect types were studied separately. Chirality respect to the direction of the uniaxial tensile load was considered: parallel to the graphene armchair (zigzag) edge. Young's modulus and the Poisson's ratio were estimated. Furthermore, a pure copper nanofilm as well as pristine and defective graphene nanoribbons were separately analyzed, to better understand their role in the nanocomposite. In general, most of the mechanical properties of graphene-copper heterostructures are guided by the way graphene itself behaves mechanically. A summary of main results and future work are presented.

- Elasticity. Vacancy and Stone-Wales defects in the graphene layer do not affect considerably the elasticity of the pristine heterostructures. In some cases, defective systems even showed a slight improvement.

  Nevertheless, elasticity depends on the chirality. Along the zigzag edge, in general systems are more elastic than their armchair counterparts with the same type and density of defects. Similar observation was made in pure graphene nanoribbons, thus they determine the response, whereas pure copper nanofilm still has the highest elasticity.

- Stiffness. In general, defective systems presented lower stiffness, that is, lower yield strengths and Young's moduli. The bigger impact was caused by vacancies than by

Stone-Wales defects, since bonds are missing (rotated) in the former (latter) case and less (more) energy is needed to deform the system. Armchair systems presented higher stiffness at the same type and density of defects. The behavior of composites is also determined by graphene, since the latter one sustains most of the tensile load.

Although pure copper is more elastic than all the heterostructures, these were considerably stiffer than copper itself. Significantly higher stresses are needed to start plastic deformation in the composite systems, even with some degree of defects, confirming that graphene strengthens copper.

- Toughness. During plastic deformation, defects had a surprisingly good effect on the toughness in several cases, depending on the chirality, type and density of the defect. In the armchair systems, for example, the nanocomposite with vacancies (Stone-Wales) at a density of 0.01 (0.02, 0.03) presented slight higher ultimate tensile stresses than the pristine one. All the zigzag systems with Stone-Wales defects turned out to be tougher than the pristine one reaching a value of over 10 GPa higher when the density was 0.02. Zigzag systems are considerably tougher than armchair ones as well. As before, the trend is dictated by graphene.

- Ductility. Improved ductility was found in some of the defective systems with higher fracture strain values at some densities, zigzag systems having higher ductility than the armchair ones. A bigger impact of the chirality rather than the type and density of defects is observed.

  The nanocomposites never break entirely in the analyzed range of strains. The graphene layers always reach their fracture point before copper. Therefore, the stress sustained by the specimens never goes to zero even though a dramatic drop is observed. That is due to the high ductility of the copper nanofilms and that they endure considerably lower stresses than graphene. In other words, in a graphene-copper heterostructure the graphene layer is responsible to sustain most of the applied tensile stress.

- Poisson's Ratio. It was calculated in both transverse directions to the direction of the uniaxial tensile load and their variation throughout the tensile tests. Positive and negative Poisson's ratios were found along the thickness direction for all graphene-copper heterostructures. They presented initially positive values which decreased

softly. At a critical strain, around a deformation of 0.09 in all cases, the Poisson's ratio becomes negative preserving the auxetic property at higher strains. Specific values depend on the chirality, type and density of the defects, but the behavior of all the curves was basically the same presenting negative Poisson's ratio during elastic deformation, several steps before their yield points were reached.

Along the width direction, the behavior was the opposite. The Poisson's ratio never became negative. Instead, the values increased alongside with the advance of the tensile tests, almost mirroring the results along the thickness direction. This is caused by branching of the lateral lattice parameters as a consequence of the surface effect reported before in these structures.

The same behavior was also observed in the analyzed pure copper nanofilm. However, here a negative value along the thickness direction is obtained at a much higher strain, while plastic deformation is already quite advanced in the pure copper nanofilm.

The mentioned surface effect is reinforced in the heterostructures, since the interfaces between the graphene and the copper layers behave as new free surfaces. Such effect causes compressive stresses in inner atoms along the width direction inducing a negative Poisson's ratio along the thickness direction as a result of branching.

5.1 Suggestions for Future Work

The development of this thesis opened up new research possibilities. One of them would be to analyzed the structural dynamics of the processes or the effect the temperature has. Another study could also be done on bigger specimens with thicker copper layers. The introduction of more defective graphene and copper layers could be explored as well as other types of defects, such as substitutional impurities, interstitial atoms, and dislocations. Also the combination of 2D materials with other metals could be investigated.

Furthermore, in this work the surface effect was the main topic used to explain the auxetic behavior of the material. However, such effect takes place only when the material has free surfaces, and for that free boundaries have to be set in the simulations. Nonetheless, it would be interesting to figure out what happens to the mechanical properties of graphene-copper heterostructures when all the boundaries are set as periodic, in order to avoid surface effects and simulate bulk systems.

Appendix A

Tensile Tests of Graphene Nanoribbons: Snapshots

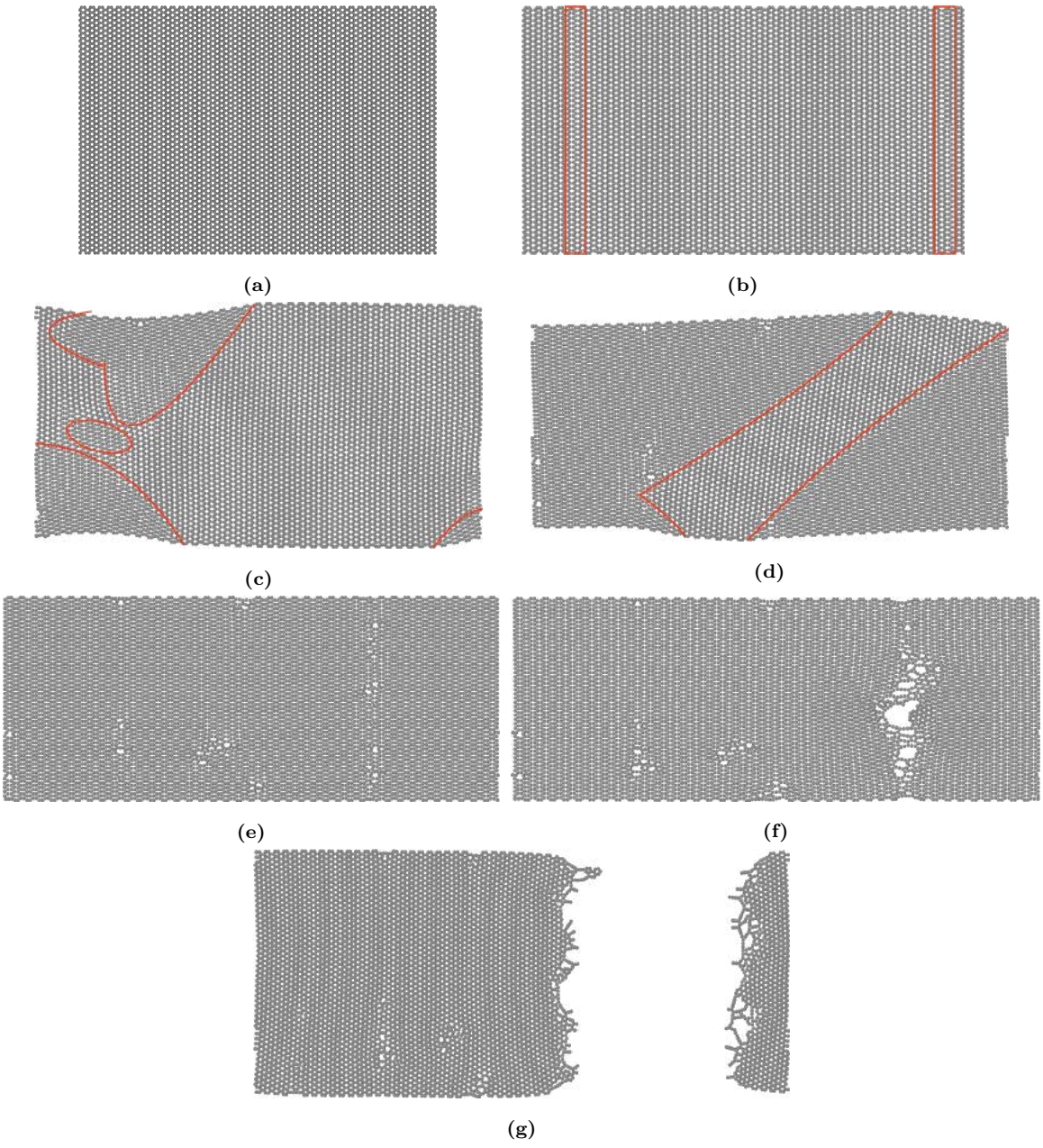

Figure A.1: Snapshots (top view) of the tensile test conducted in the pristine AC GNR at different ε_x^s. (a) $\varepsilon_x^s = 0.0000$. Before straining. (b) $\varepsilon_x^s = 0.2370$. At this ε_x^s the phase transition starts in the zones inside the red rectangles. (c) $\varepsilon_x^s = 0.2510$. Larger zones where the orthorhombic phase have already appeared can be seen inside the drawn red boundaries. These are the sheared regions. (d) $\varepsilon_x^s = 0.3340$. Here, most of the top left and bottom right zones are composed by atoms arranged in the orthorhombic phase. Only the atoms at a diagonal non-sheared region extending from the top right corner to the bottom remain arranged at a honeycomb phase. (e) $\varepsilon_x^s = 0.3895$. All the atoms are now arranged in an orthorhombic lattice and a few C-C bonds have already been broken. (f) $\varepsilon_x^s = 0.4795$. The pristine AC GNR starts fracturing vertically in its middle-right part. (g) $\varepsilon_x^s = 0.4985$. The fracture process has been completed. Note that the atoms return to their hexagonal configuration and some defects were formed on both remaining slices of nanoribbon.

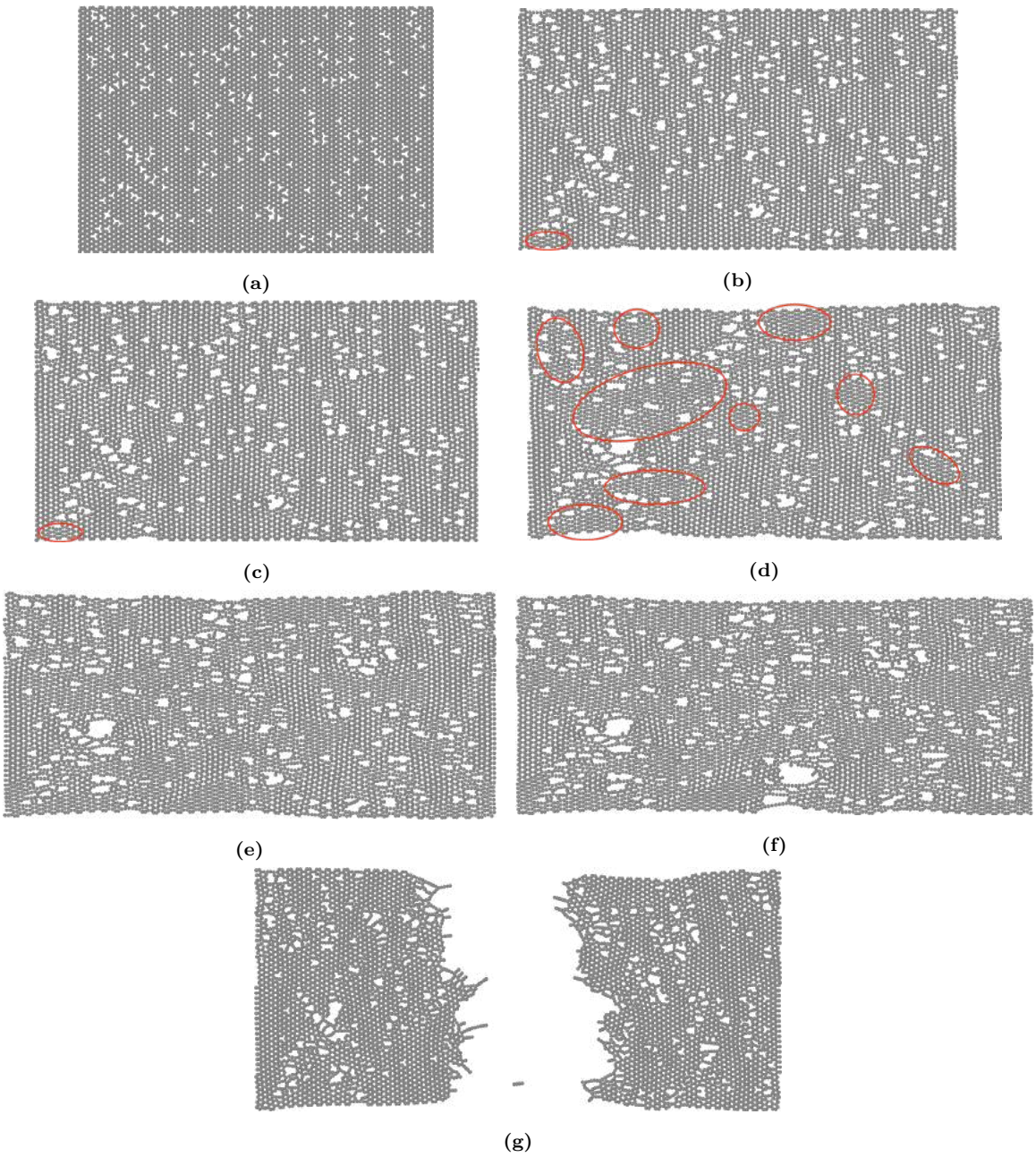

Figure A.2: Snapshots (top view) of the tensile test conducted in the AC GNR with vacancies at $\rho_{Vac} = 0.03$ and different ε_x^s. (a) $\varepsilon_x^s = 0.0000$. Before straining. (b) $\varepsilon_x^s = 0.2370$. The phase transition appears only inside the red ellipse. (c) $\varepsilon_x^s = 0.2510$. Here, while larger sheared regions where the orthorhombic phase have already appeared in several regions of the pristine AC GNR, with vacancies this phase is still present just inside the red ellipse. (d) $\varepsilon_x^s = 0.3340$. Differently from the pristine case, the atoms arranged in the orthorhombic phase appear in smaller scattered sheared regions. (e) $\varepsilon_x^s = 0.3895$. There is still a few hexagonal lattices remaining while in the pristine case, all the atoms already arranged at an orthorhombic lattice. (f) $\varepsilon_x^s = 0.4495$. The AC GNR with vacancies starts fracturing. (g) $\varepsilon_x^s = 0.4730$. The fracture process has been completed. Similar to the pristine case, the atoms in both remaining slices of the GNR with vacancies tend to return to their hexagonal configuration. However, multi-vacancies are formed.

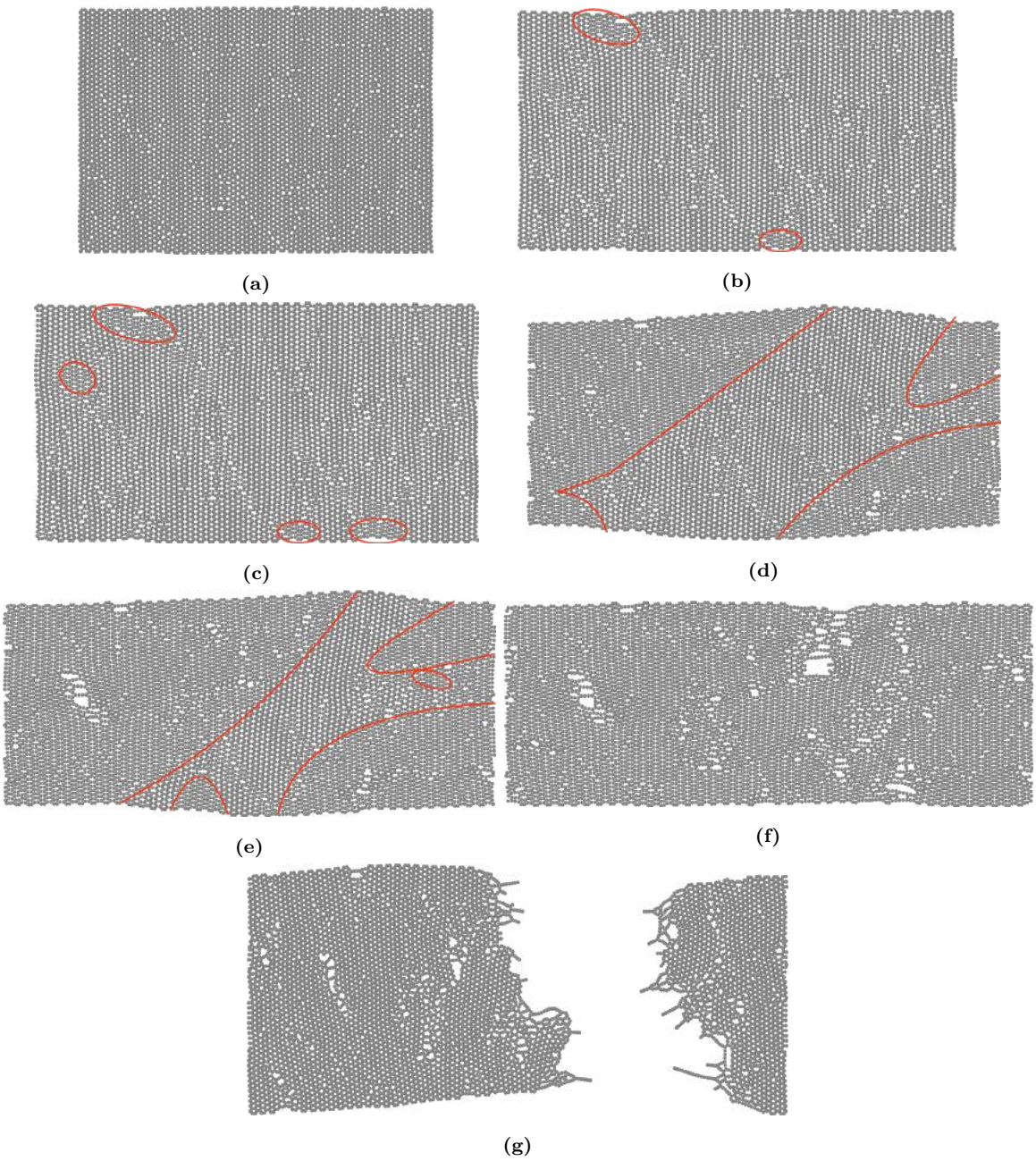

Figure A.3: Snapshots (top view) of the tensile test conducted in the AC GNR with SW defects at $\rho_{SW} = 0.03$ and different ε_x^s. (a) $\varepsilon_x^s = 0.0000$. Before straining. (b) $\varepsilon_x^s = 0.2370$. The phase transition takes place only inside the red ellipses. (c) $\varepsilon_x^s = 0.2510$. While larger sheared regions where the orthorhombic phase appears in the pristine AC GNR, here they are present just in the small zones inside the red ellipses. (d) $\varepsilon_x^s = 0.3340$. More sheared regions with better defined borders appear, in contrast to the vacancy case where this happens in scattered zones. (e) $\varepsilon_x^s = 0.3895$. There is still a few hexagonal zones remaining. In the pristine AC GNR, all the atoms were already arranged in an orthorhombic lattice at this point. (f) $\varepsilon_x^s = 0.4850$. Fracture starts. Here, neglecting the defects, all atoms are now arranged in an orthorhombic lattice. (g) $\varepsilon_x^s = 0.5165$. The fracture process has completed. Like in the pristine and vacancy defective, the atoms in both remaining slices of the AC GNR with SW defects also tend to return to their hexagonal configuration, however with the formation of more complex defects.

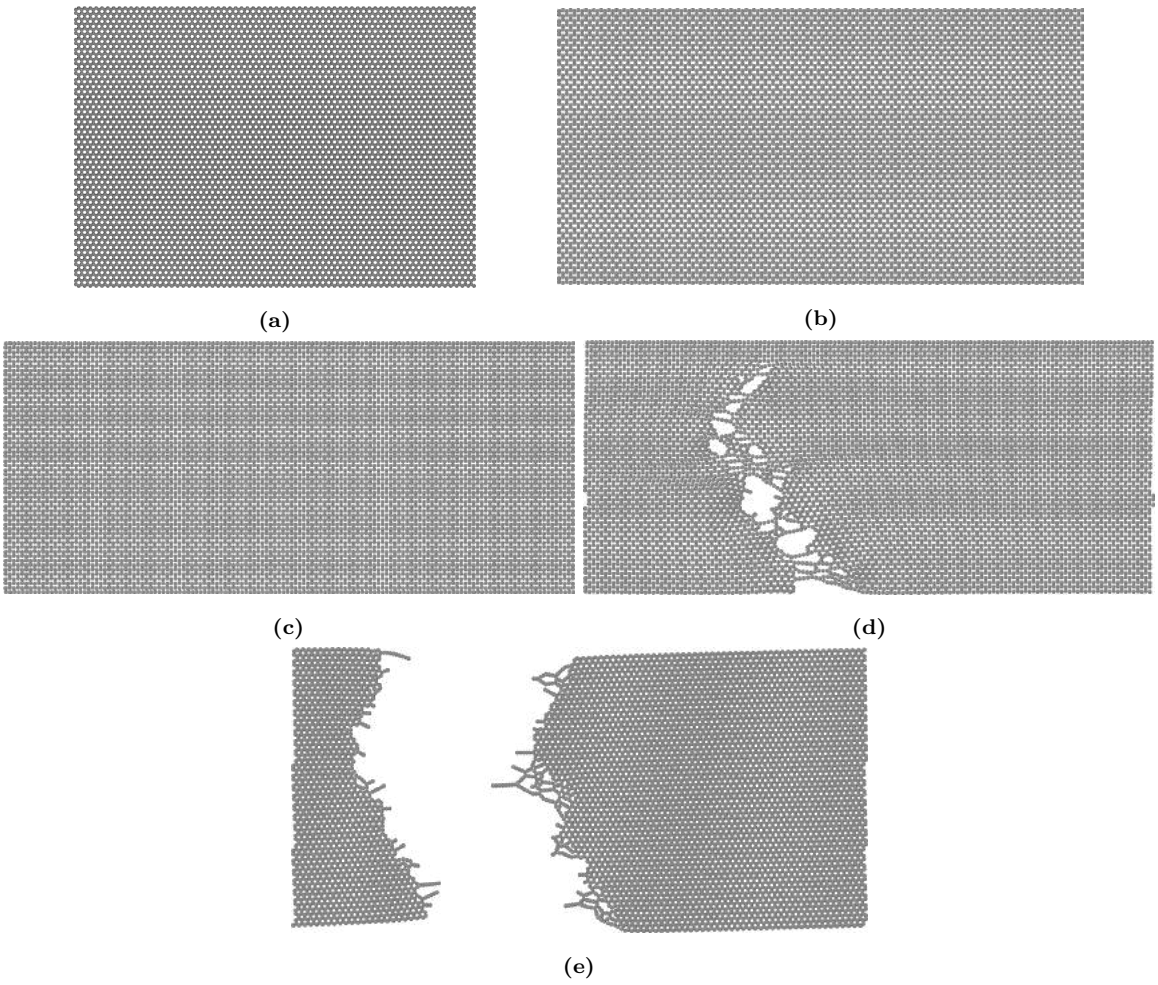

Figure A.4: Snapshots (top view) of the tensile test conducted in the pristine ZZ GNR at different ε_x^s. (a) $\varepsilon_x^s = 0.0000$. Before straining. (b) $\varepsilon_x^s = 0.3120$. Point where a sudden increase in the SSC begins. (c) $\varepsilon_x^s = 0.4250$. Point right before the SSC reaches its σ_{TS}. (d) $\varepsilon_x^s = 0.4260$. Fracture starts to take place diagonally right after σ_{TS} is reached. (e) $\varepsilon_x^s = 0.4375$. The fracture process has been completed, and the atoms in the remaining two slices of the pristine ZZ GNR rearrange themselves back to the original honeycomb lattice.

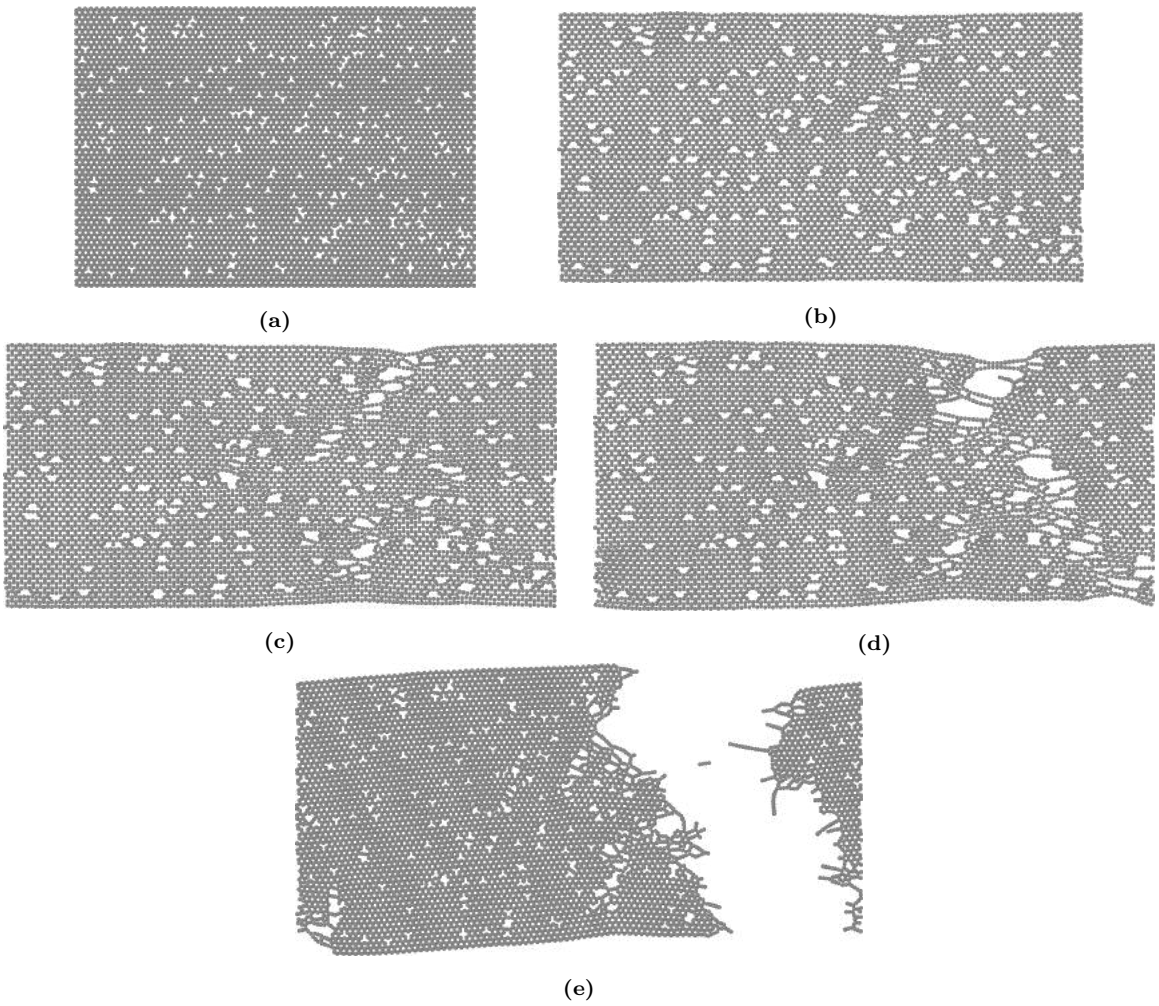

Figure A.5: Snapshots (top view) of the tensile test conducted in the ZZ GNR with vacancies at $\rho_{Vac} = 0.03$ and different ε_x^s. (a) $\varepsilon_x^s = 0.0000$. Before straining. (b) $\varepsilon_x^s = 0.3120$. Point where a sudden increase in the SSC begins. (c) $\varepsilon_x^s = 0.3805$. Point right before the SSC reaches its σ_{TS}. (d) $\varepsilon_x^s = 0.4005$. Fracture starts to take place right after σ_{TS} is reached. (e) $\varepsilon_x^s = 0.4160$. The fracture process has been completed, and the atoms in the remaining two slices of the ZZ GNR with vacancies rearrange themselves back to the original honeycomb lattice. However, many of the previous vacancies are still present and some new ones, including a few more complex defects, are created.

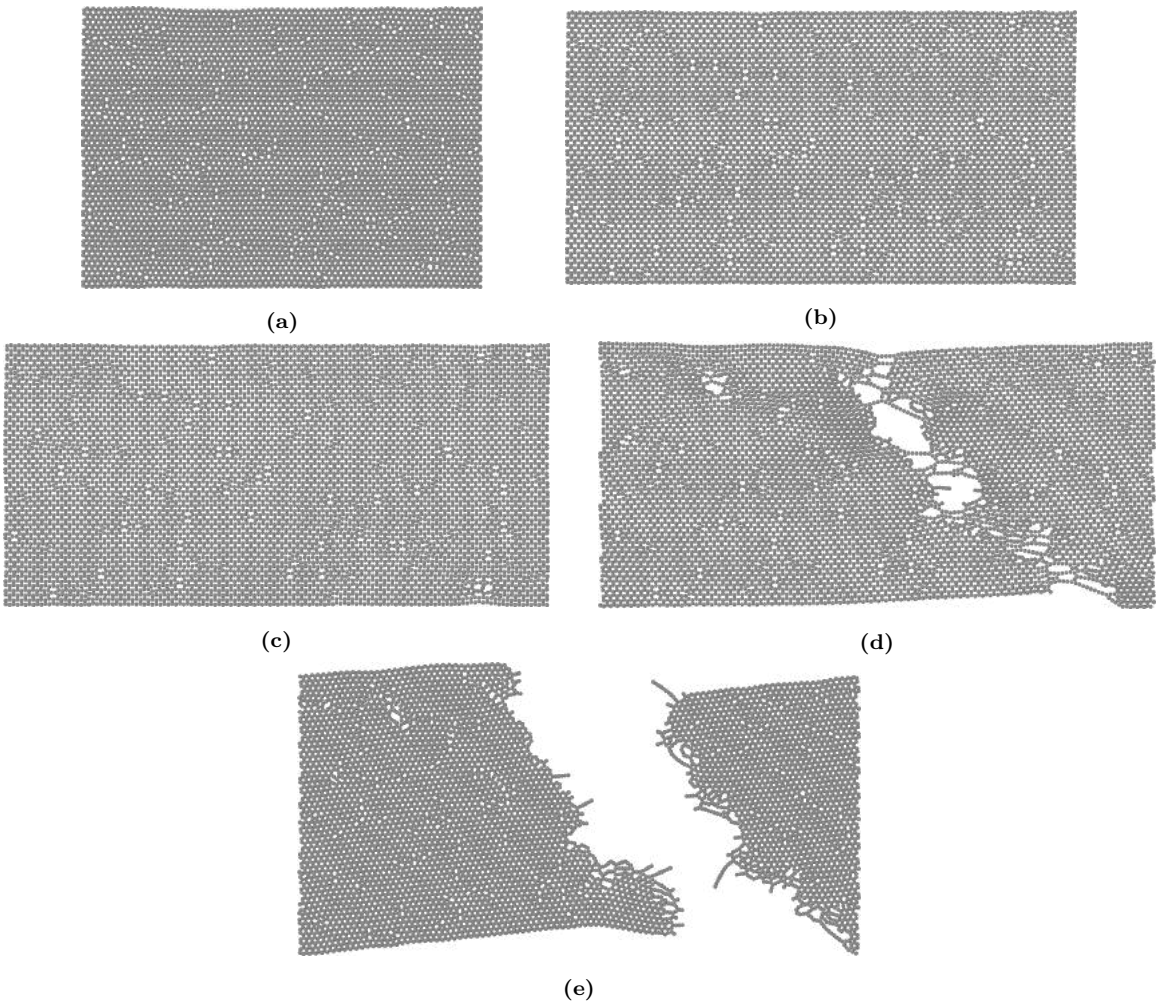

Figure A.6: Snapshots (top view) of the tensile test conducted in the ZZ GNR with SW defects at $\rho_{SW} = 0.03$ and different ε_x^s. (a) $\varepsilon_x^s = 0.0000$. Before straining. (b) $\varepsilon_x^s = 0.2750$. Point where a sudden increase in the SSC begins. (c) $\varepsilon_x^s = 0.3645$. Point right before the SSC reaches its σ_{TS}. (d) $\varepsilon_x^s = 0.3880$. Fracture starts to take place right after σ_{TS} is reached. (e) $\varepsilon_x^s = 0.4050$. The fracture process has been completed, and the atoms in the remaining two slices of the ZZ GNR with SW defects rearrange themselves back to the original honeycomb lattice. However, 5-7-7-5 SW pairs are still present, as well as a few more complex defects.

Appendix B

Tensile Test of the Copper Nanofilm: Snapshots

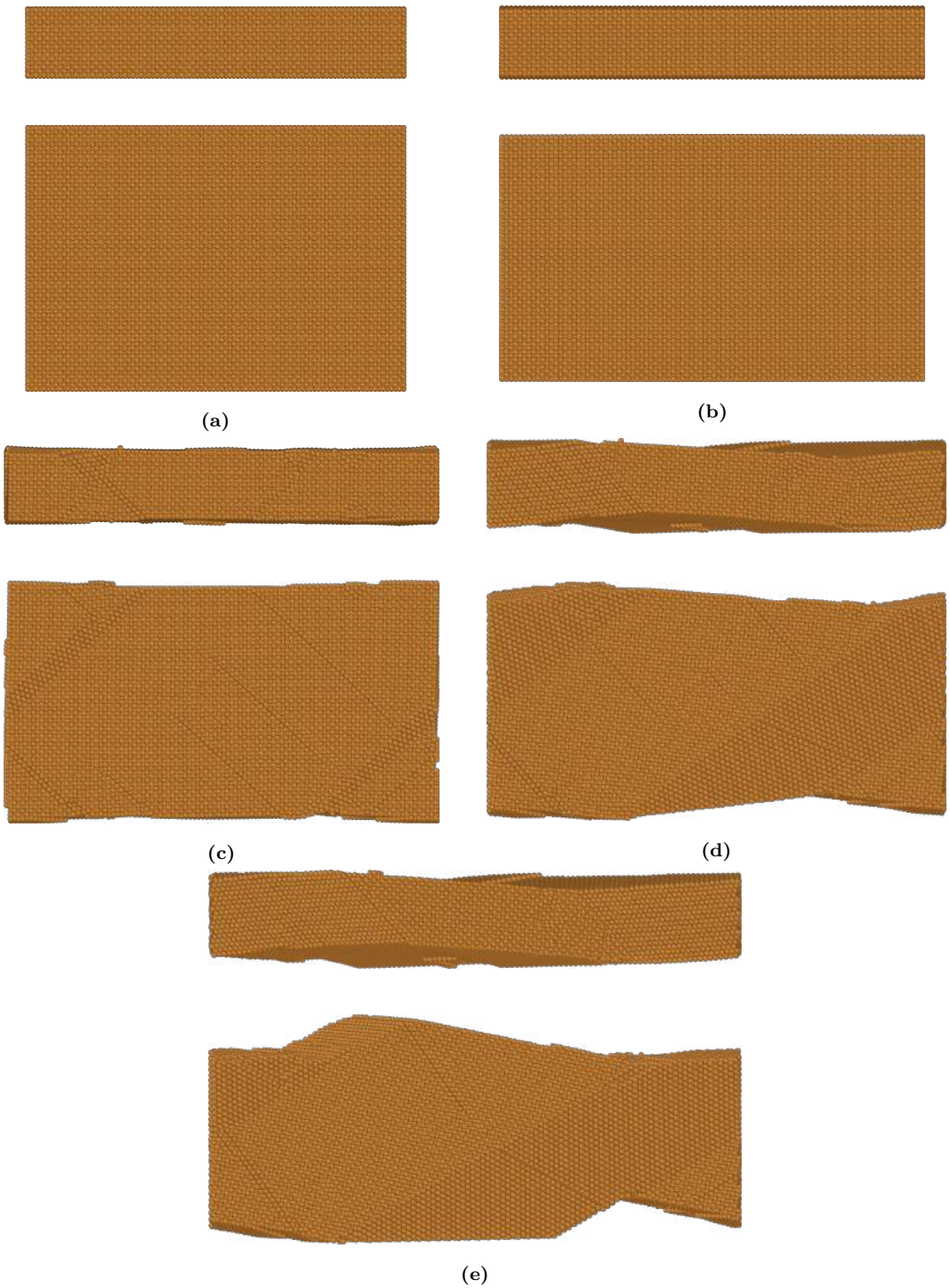

Figure B.1: Snapshots (front and top views) of the tensile test conducted in the pure Cu nanofilm. (a) $\varepsilon_x^s = 0.0000$. Before straining. (b) $\varepsilon_x^s = 0.1165$. Point right before dislocations begin to form, around the σ_Y point in the SSC. (c) $\varepsilon_x^s = 0.1420$. Lower-yield point in the SSC. (d) $\varepsilon_x^s = 0.2060$. Point before a plateau in the SSC appears. Necking can already been observed. (e) $\varepsilon_x^s = 0.4000$. Advanced plastic deformation. Many dislocations have already been formed and necking is more evident.

Appendix C

Tensile Tests of Graphene-Copper Heterostructures: Snapshots

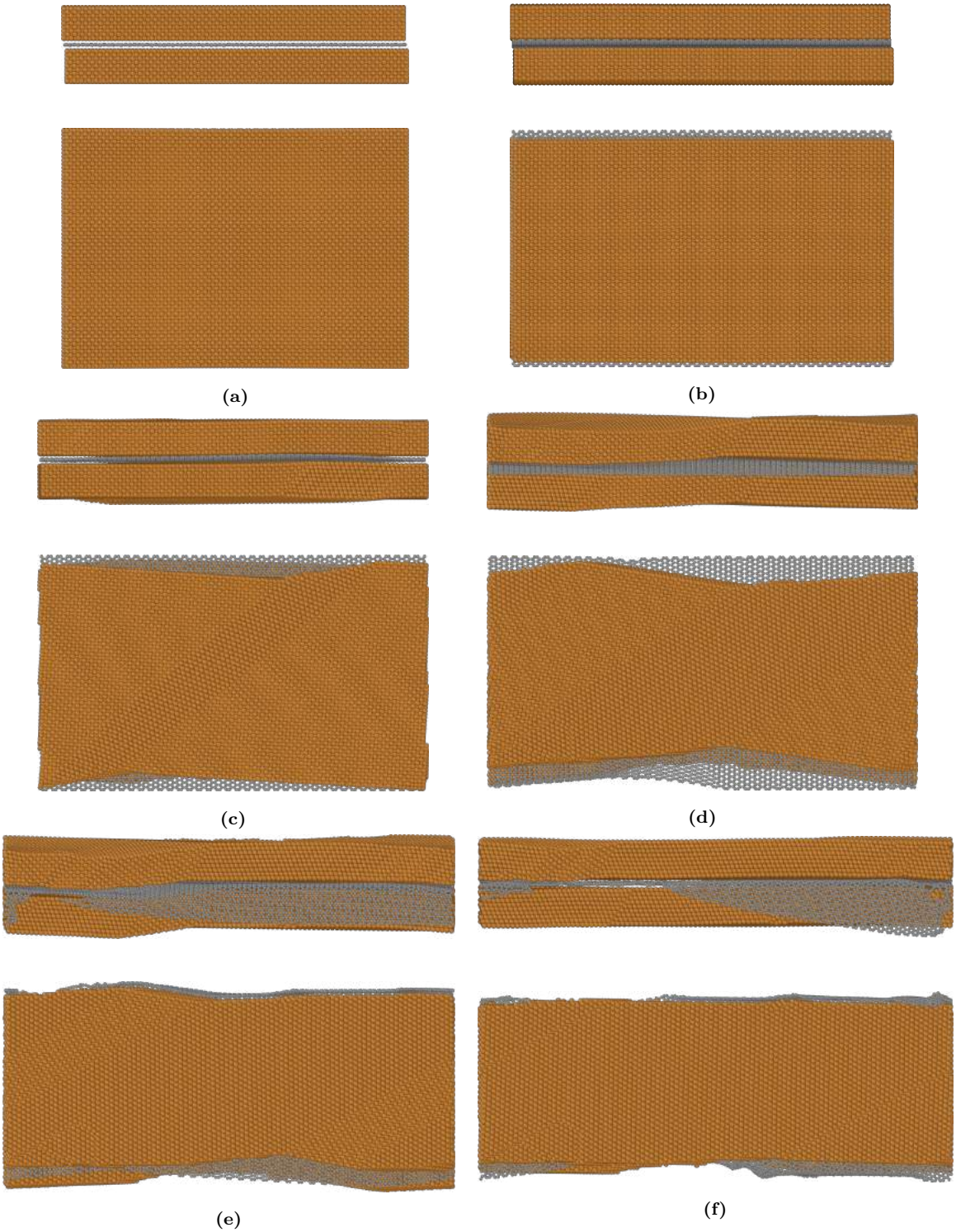

Figure C.1: Snapshots (front and top views) of the tensile test conducted in the pristine AC G-Cu heterostructure at different ε_x^s. (a) $\varepsilon_x^s = 0.0000$. Nanocomposite before straining. (b) $\varepsilon_x^s = 0.1050$, σ_Y point. (c) $\varepsilon_x^s = 0.1270$, near to the lower-yield point. (d) $\varepsilon_x^s = 0.2405$, near the σ_{TS} point. (e) $\varepsilon_x^s = 0.3040$. Minimum point reached in the SSC right after ε_F. (f) $\varepsilon_x^s = 0.3700$. Here, advanced failure in the graphene layer has occurred (see figure C.2).

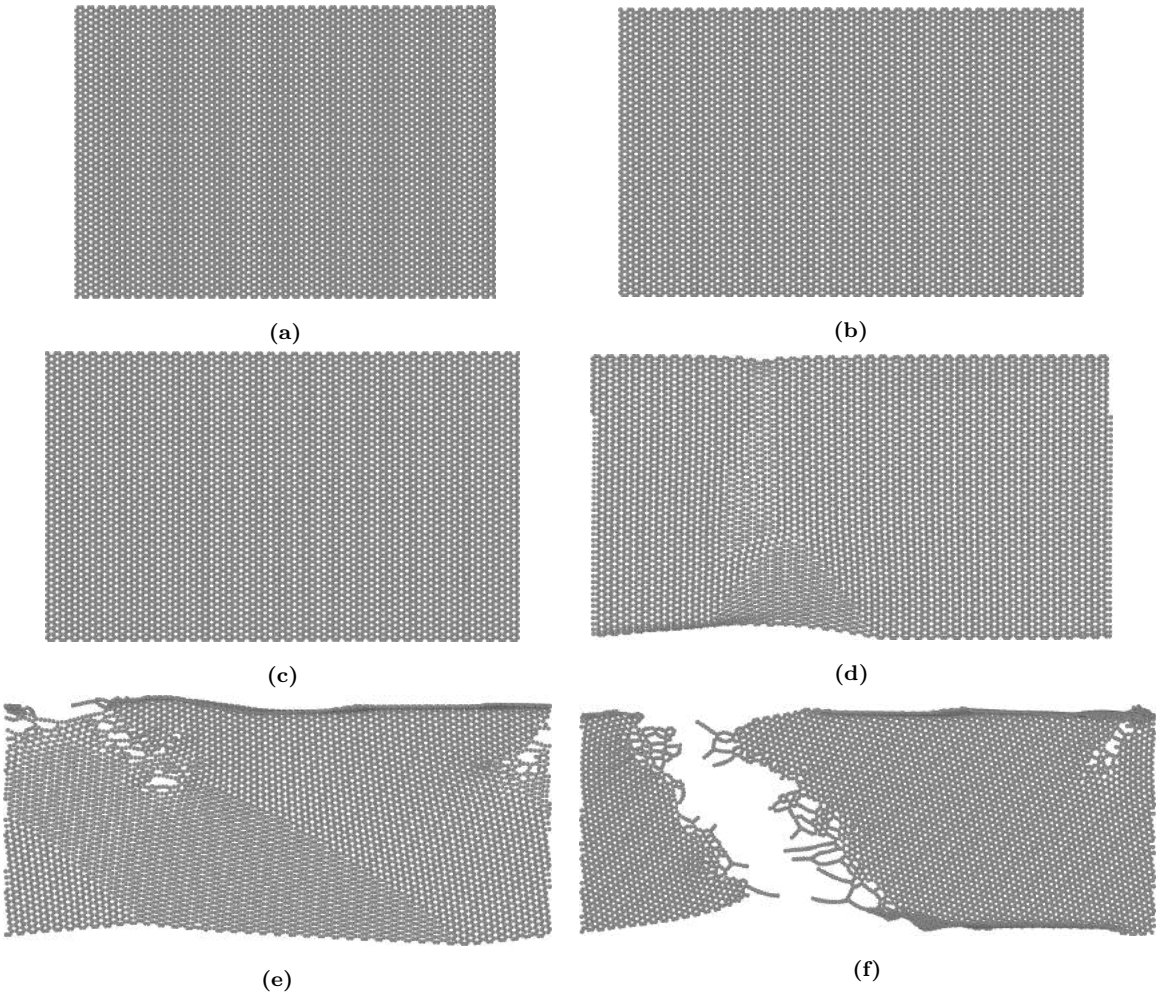

Figure C.2: Snapshots (top view) of the graphene layer in the pristine AC G-Cu heterostructure at different ε_x^s values. (a) $\varepsilon_x^s = 0.0000$. Pristine AC graphene layer before straining. (b) $\varepsilon_x^s = 0.1050$, σ_Y point. (c) $\varepsilon_x^s = 0.1270$, around the lower-yield point. (d) $\varepsilon_x^s = 0.2405$, around the σ_{TS} point. (e) $\varepsilon_x^s = 0.3040$. Minimum point reached in the SSC right after ε_F. (f) $\varepsilon_x^s = 0.3700$. Here, advanced failure in the graphene layer has occurred.

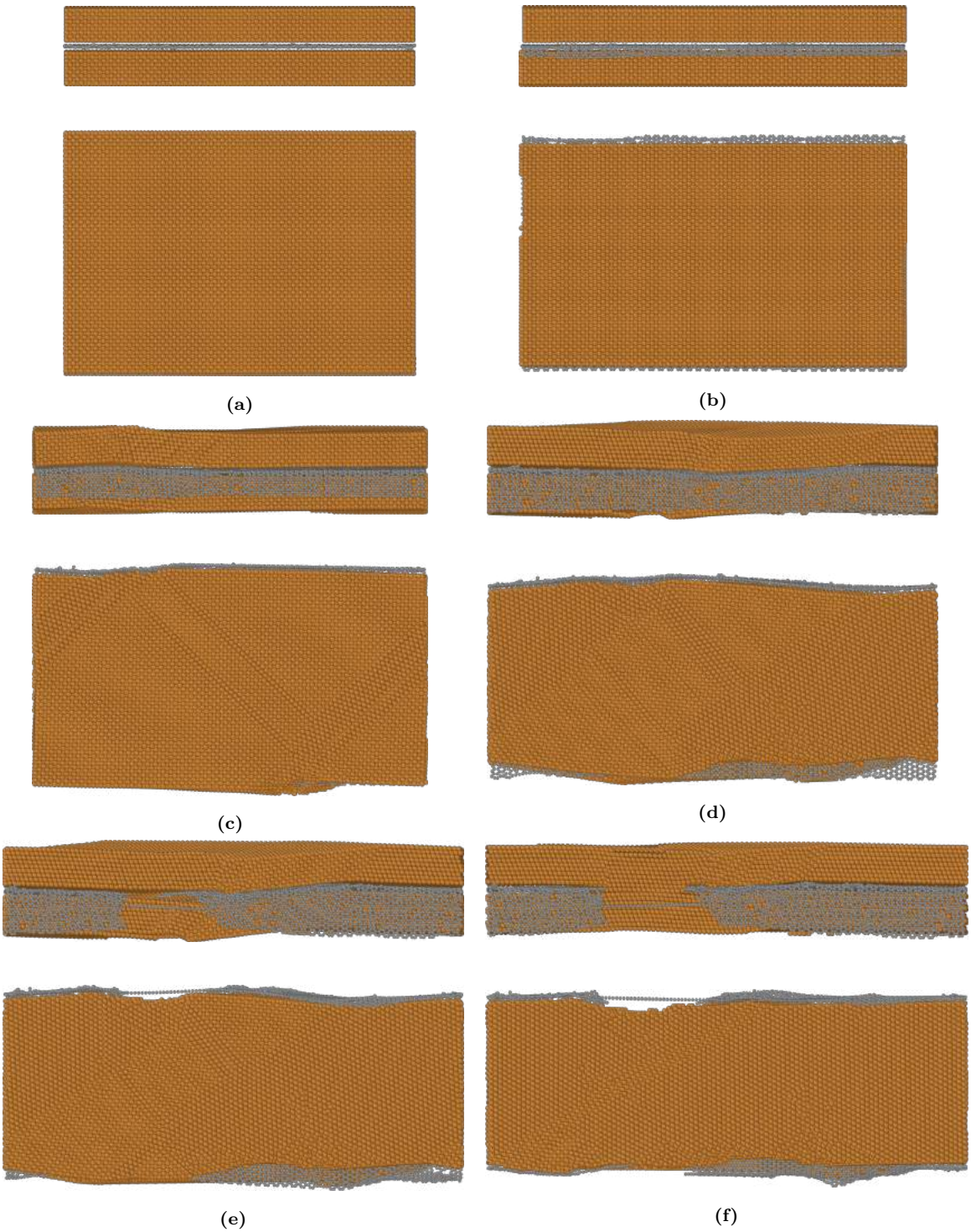

Figure C.3: Snapshots (front and top views) of the tensile test conducted in the AC G-Cu heterostructure with vacancies in the graphene layer, at $\rho_{Vac} = 0.03$ and different ε_x^s. (a) $\varepsilon_x^s = 0.0000$. Nanocomposite before straining. (b) $\varepsilon_x^s = 0.1005$, near to the σ_Y point. (c) $\varepsilon_x^s = 0.1225$, neart to the lower-yield point. (d) $\varepsilon_x^s = 0.2785$, near to the σ_{TS} point. (e) $\varepsilon_x^s = 0.3100$. Minimum point reached in the SSC right after ε_F. (f) $\varepsilon_x^s = 0.3700$. Here, advanced failure in the graphene layer has occurred (see figure C.4).

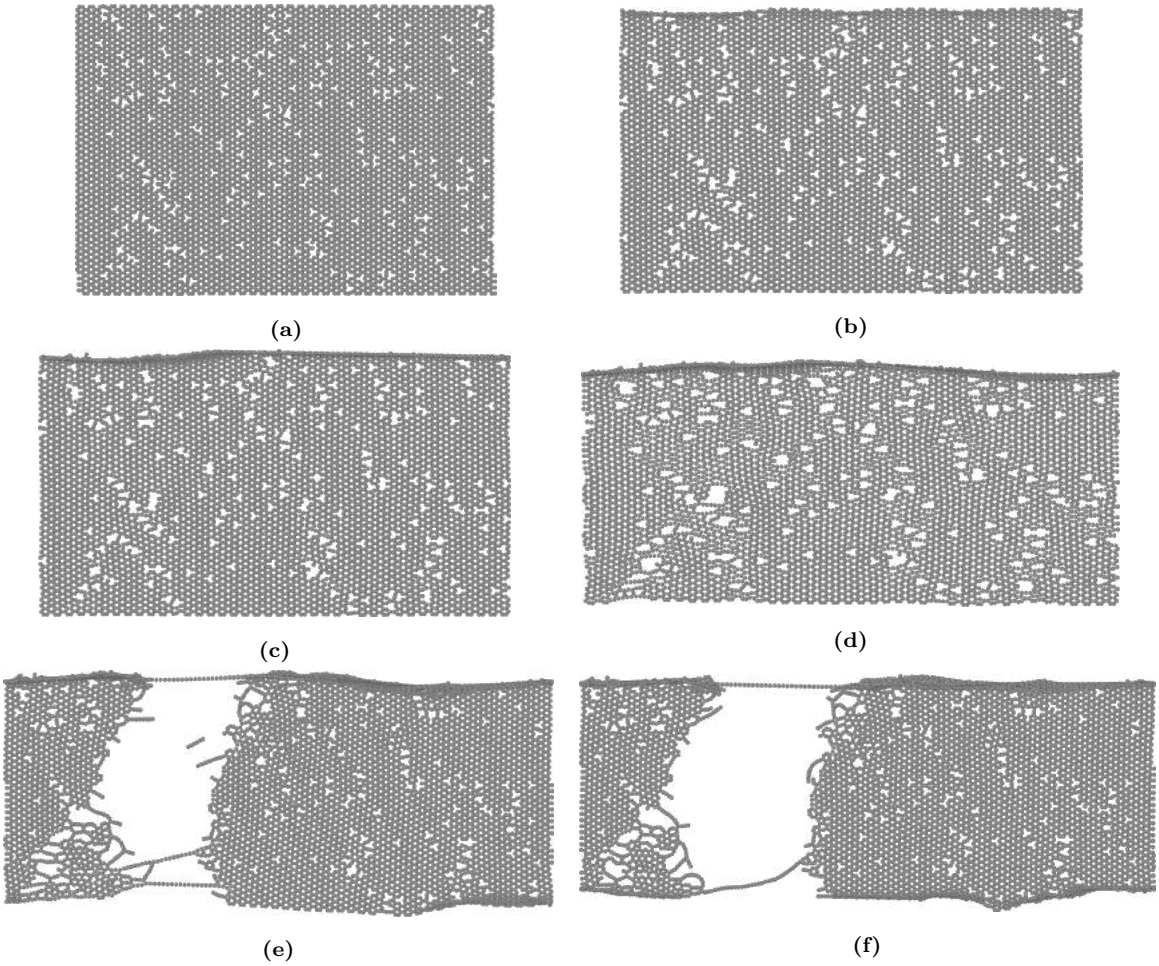

Figure C.4: Snapshots (top view) of the graphene layer with vacancies in the AC G-Cu heterostructure at $\rho_{Vac} = 0.03$ and different ε_x^s. (a) $\varepsilon_x^s = 0.0000$. Before straining. (b) $\varepsilon_x^s = 0.1005$, near to the σ_Y point. (c) $\varepsilon_x^s = 0.1225$, near to the lower-yield point. (d) $\varepsilon_x^s = 0.2785$, near to the σ_{TS} point. (e) $\varepsilon_x^s = 0.3100$. Minimum point reached in the SSC right after ε_F. (f) $\varepsilon_x^s = 0.3700$. Here, advanced failure in the graphene layer has occurred.

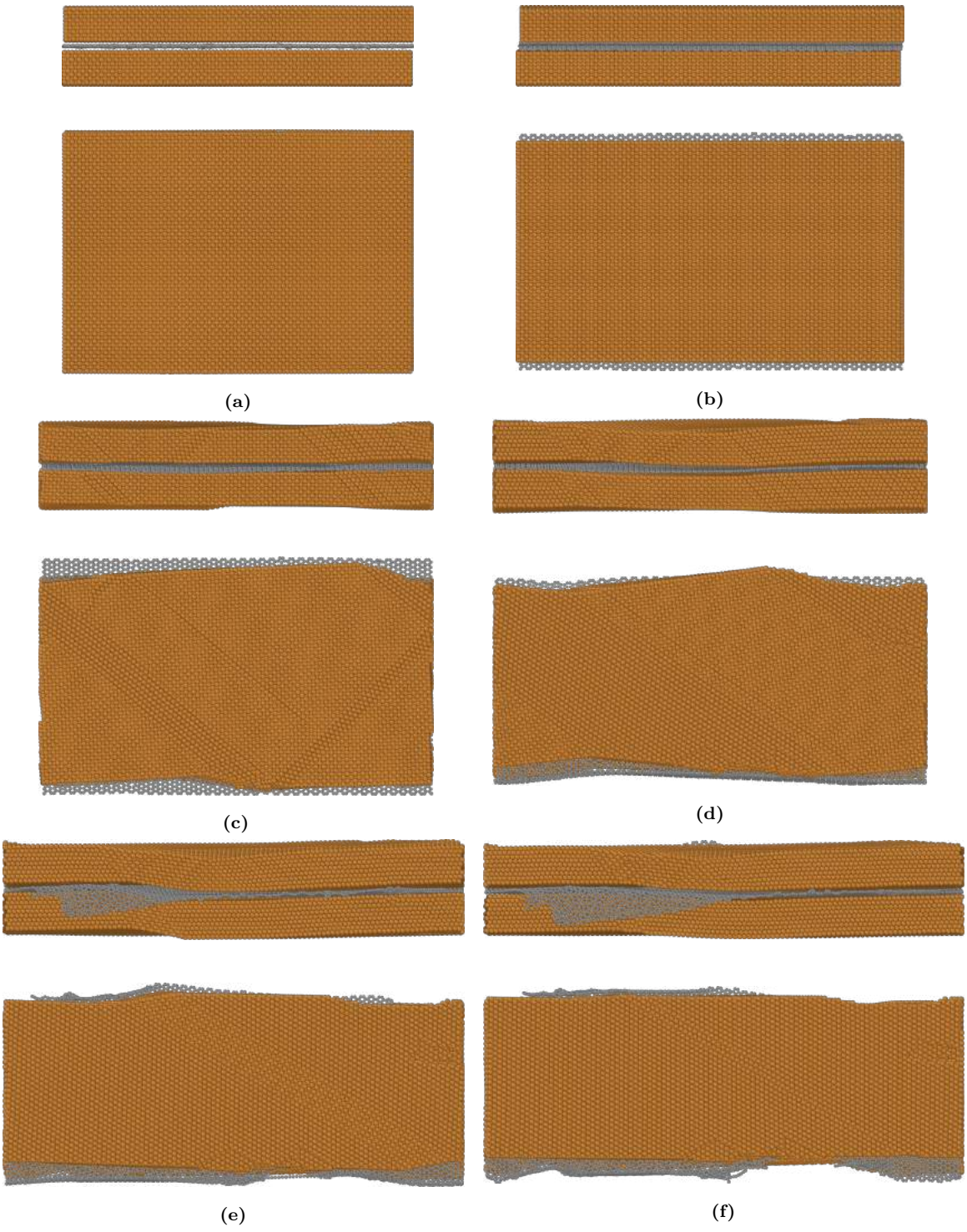

Figure C.5: Snapshots (front and top views) of the tensile test conducted in the AC G-Cu heterostructure with SW defects in the graphene layer at $\rho_{SW} = 0.03$ and different ε_x^s. (a) $\varepsilon_x^s = 0.0000$. Nanocomposite before straining. (b) $\varepsilon_x^s = 0.1050$, near to the σ_Y point. (c) $\varepsilon_x^s = 0.1240$, near to the lower-yield point. (d) $\varepsilon_x^s = 0.2400$, near to the σ_{TS} point. (e) $\varepsilon_x^s = 0.3155$. Minimum point reached in the SSC right after ε_F. (f) $\varepsilon_x^s = 0.3700$. Here, advanced failure in the graphene layer has occurred (see figure C.6).

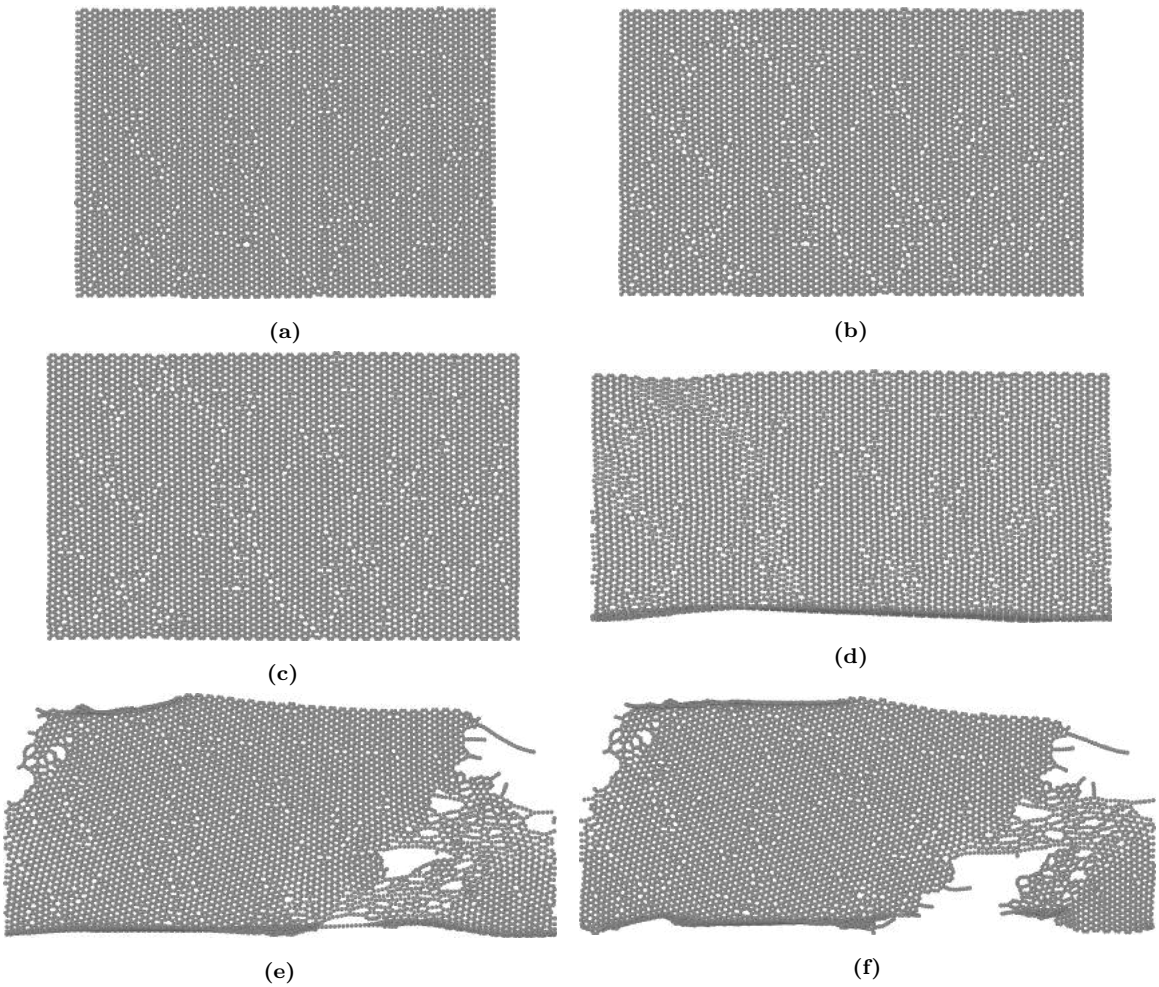

Figure C.6: Snapshots (top view) of the graphene layer with SW defects in the AC G-Cu heterostructure at ρ_{SW} = 0.03 and different ε_x^s. (a) ε_x^s = 0.0000. Before straining. (b) ε_x^s = 0.1050, near to the σ_Y point. (c) ε_x^s = 0.1240, near to the lower-yield point. (d) ε_x^s = 0.2400, near to the σ_{TS} point. (e) ε_x^s = 0.3155. Minimum point reached in the SSC right after ε_F. (f) ε_x^s = 0.3700. Here, advanced failure in the graphene layer has occurred.

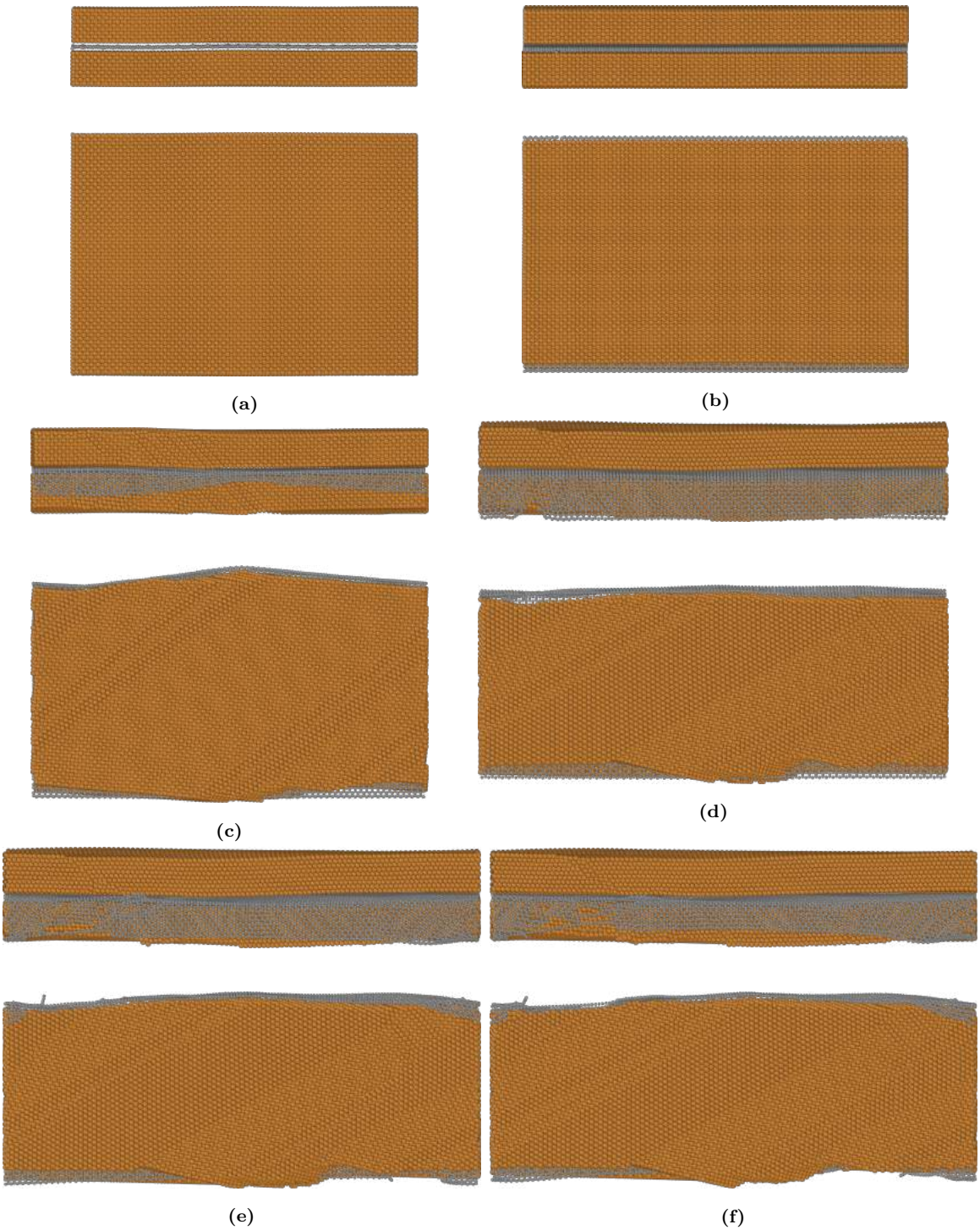

Figure C.7: Snapshots (front and top views) of the tensile test conducted in the pristine ZZ G-Cu heterostructure at different ε_x^s. (a) $\varepsilon_x^s = 0.0000$. Nanocomposite before straining. (b) $\varepsilon_x^s = 0.1100$, near to the σ_Y point. (c) $\varepsilon_x^s = 0.1425$, near to the lower-yield point. (d) $\varepsilon_x^s = 0.3515$, near to the σ_{TS} point. (e) $\varepsilon_x^s = 0.3740$. Here, failure has already taken place in the graphene layer (see figure C.8). (f) $\varepsilon_x^s = 0.4000$.

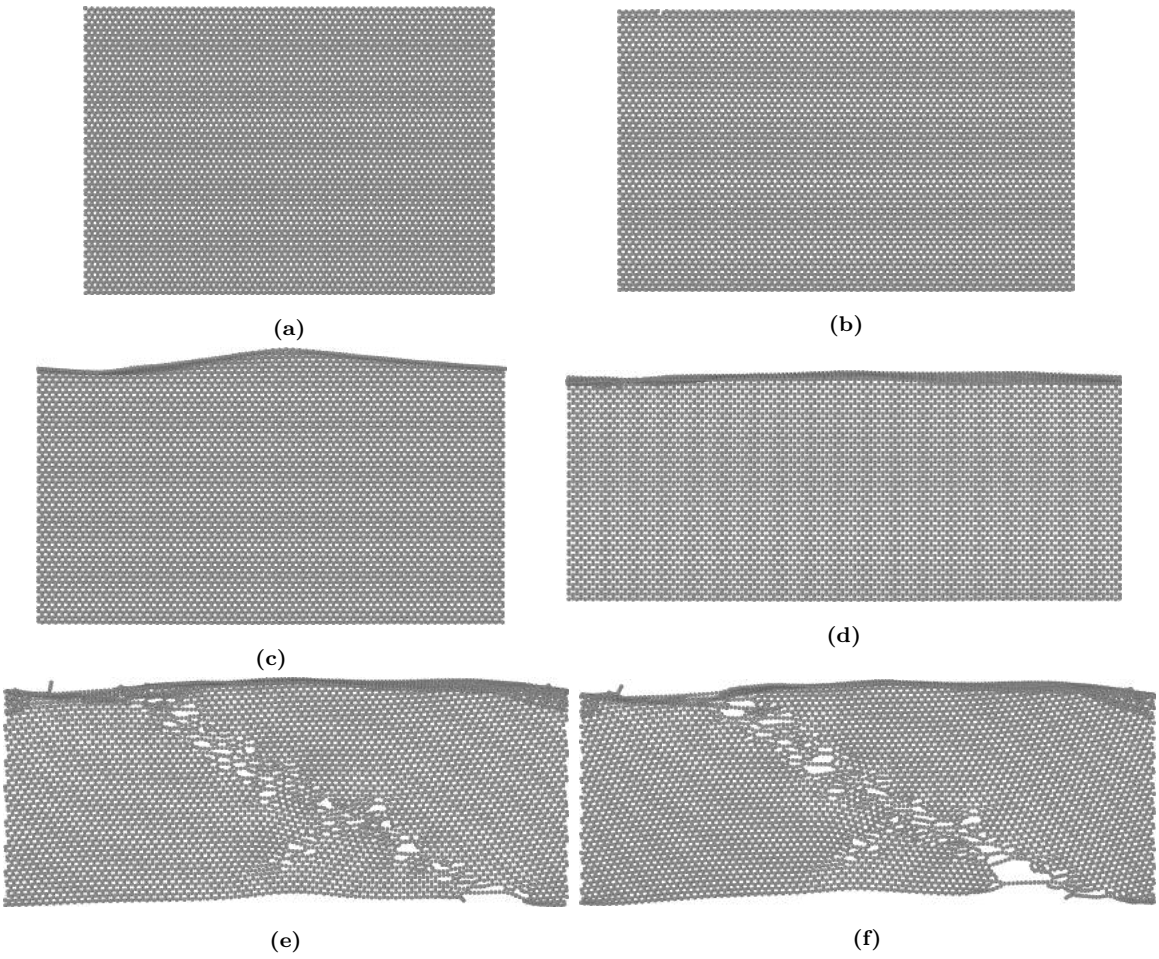

Figure C.8: Snapshots (top view) of the graphene layer in the pristine ZZ G-Cu heterostructure at different ε_x^s values. (a) $\varepsilon_x^s = = 0.0000$. Pristine ZZ graphene layer before straining. (b) $\varepsilon_x^s = 0.1100$, around the σ_Y point. (c) $\varepsilon_x^s = 0.1425$, around the lower-yield point. (d) $\varepsilon_x^s = 0.3515$, around the σ_{TS} point. (e) $\varepsilon_x^s = 0.3740$. Here, failure has already taken place in the graphene layer. (f) $\varepsilon_x^s = 0.4000$.

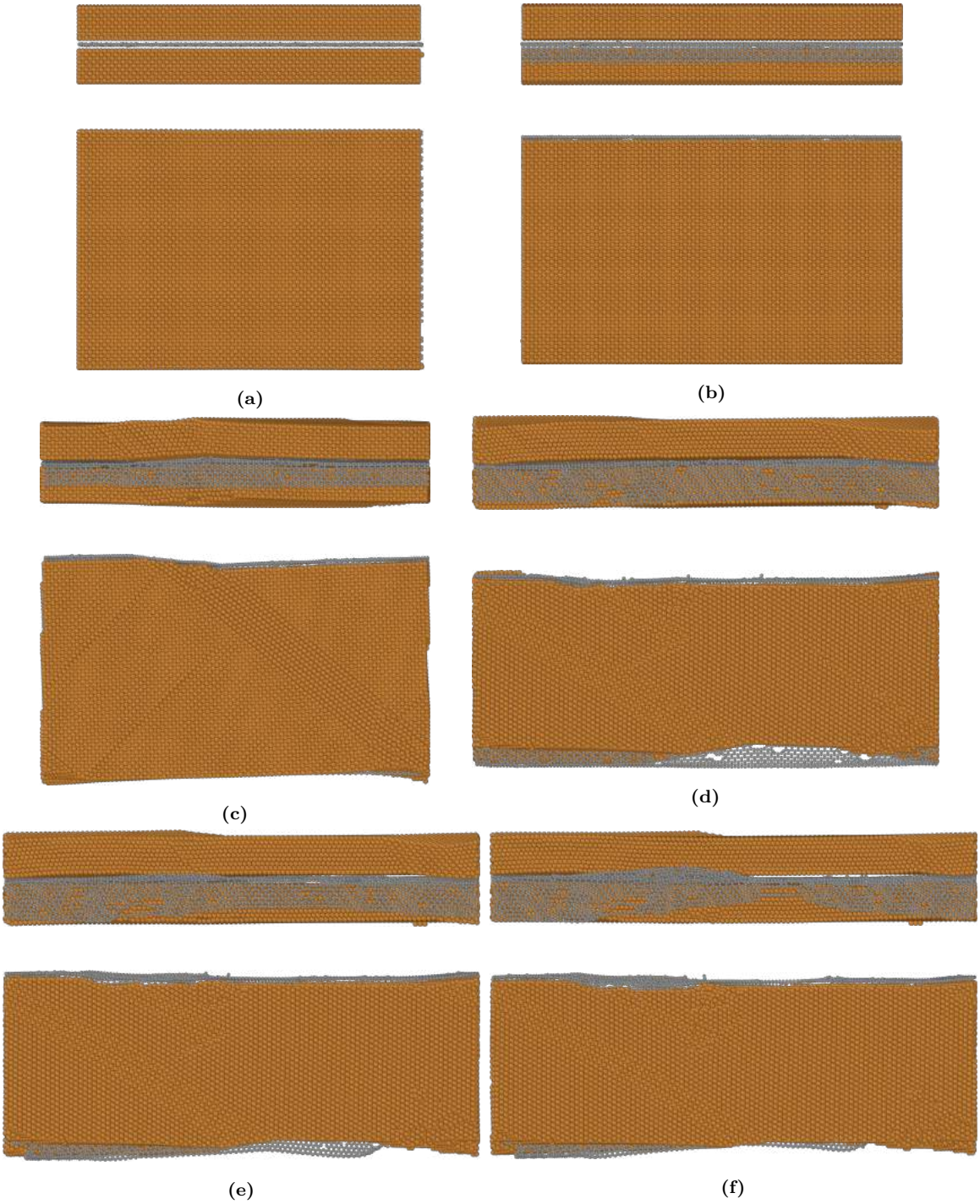

Figure C.9: Snapshots (front and top views) of the tensile test conducted in the ZZ G-Cu heterostructure with vacancies in the graphene layer at a $\rho_{Vac} = 0.03$ and different ε_x^s. (a) $\varepsilon_x^s = 0.0000$. Nanocomposite before straining. (b) $\varepsilon_x^s = 0.1005$, around the σ_Y point. (c) $\varepsilon_x^s = 0.1195$, near to the lower-yield point. (d) $\varepsilon_x^s = 0.3425$, near to the σ_{TS} point. (e) $\varepsilon_x^s = 0.3715$. Here, failure has already taken place in the graphene layer (see figure C.10). (f) $\varepsilon_x^s = 0.4000$.

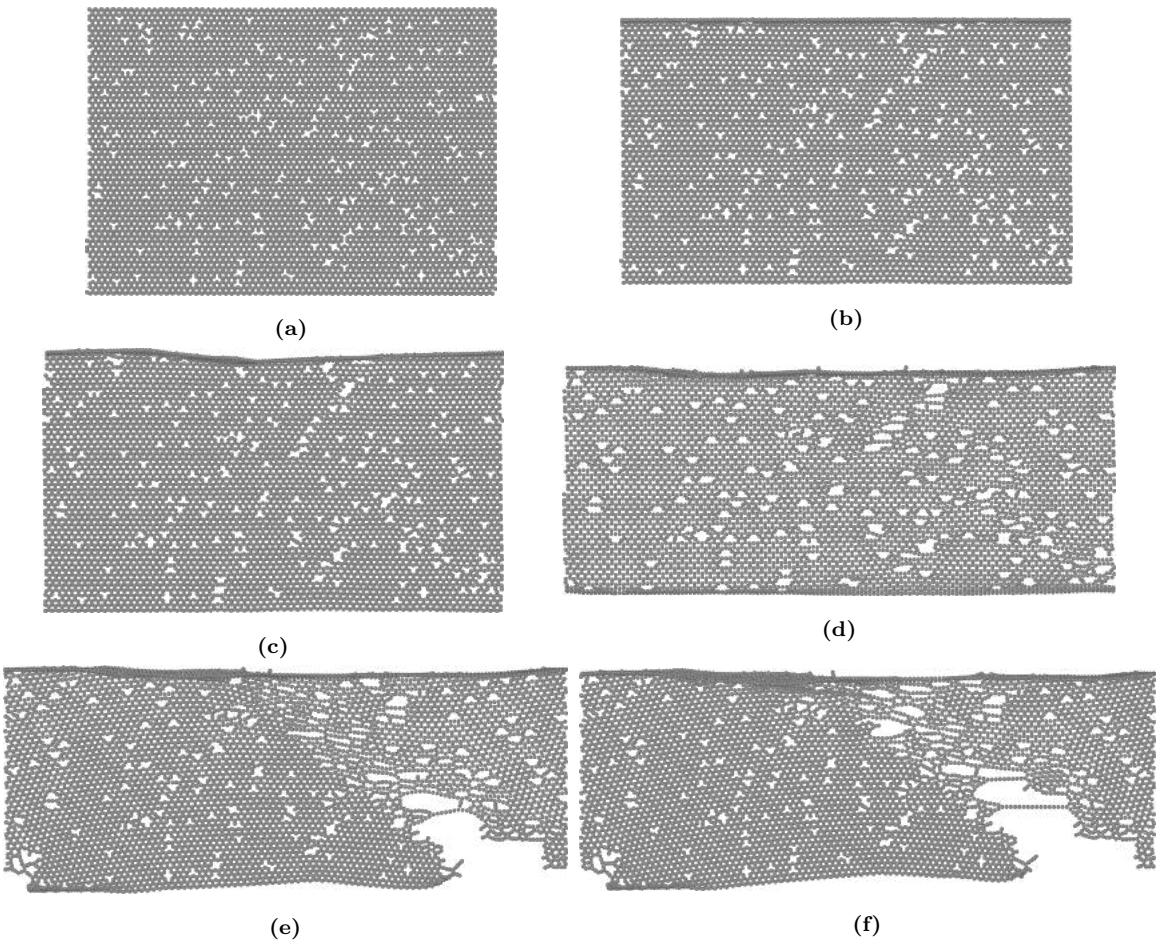

Figure C.10: Snapshots (top view) of the graphene layer in the ZZ G-Cu heterostructure with vacancies at $\rho_{Vac} = 0.03$ and different ε_x^s. (a) $\varepsilon_x^s = 0.0000$. Before straining. (b) $\varepsilon_x^s = 0.1005$, near to the σ_Y point. (c) $\varepsilon_x^s = 0.1195$, near to the lower-yield point. (d) $\varepsilon_x^s = 0.3425$, near to the σ_{TS} point. (e) ε_x^s =0.3715. Here, failure has already taken place in the graphene layer. (f) $\varepsilon_x^s = 0.4000$.

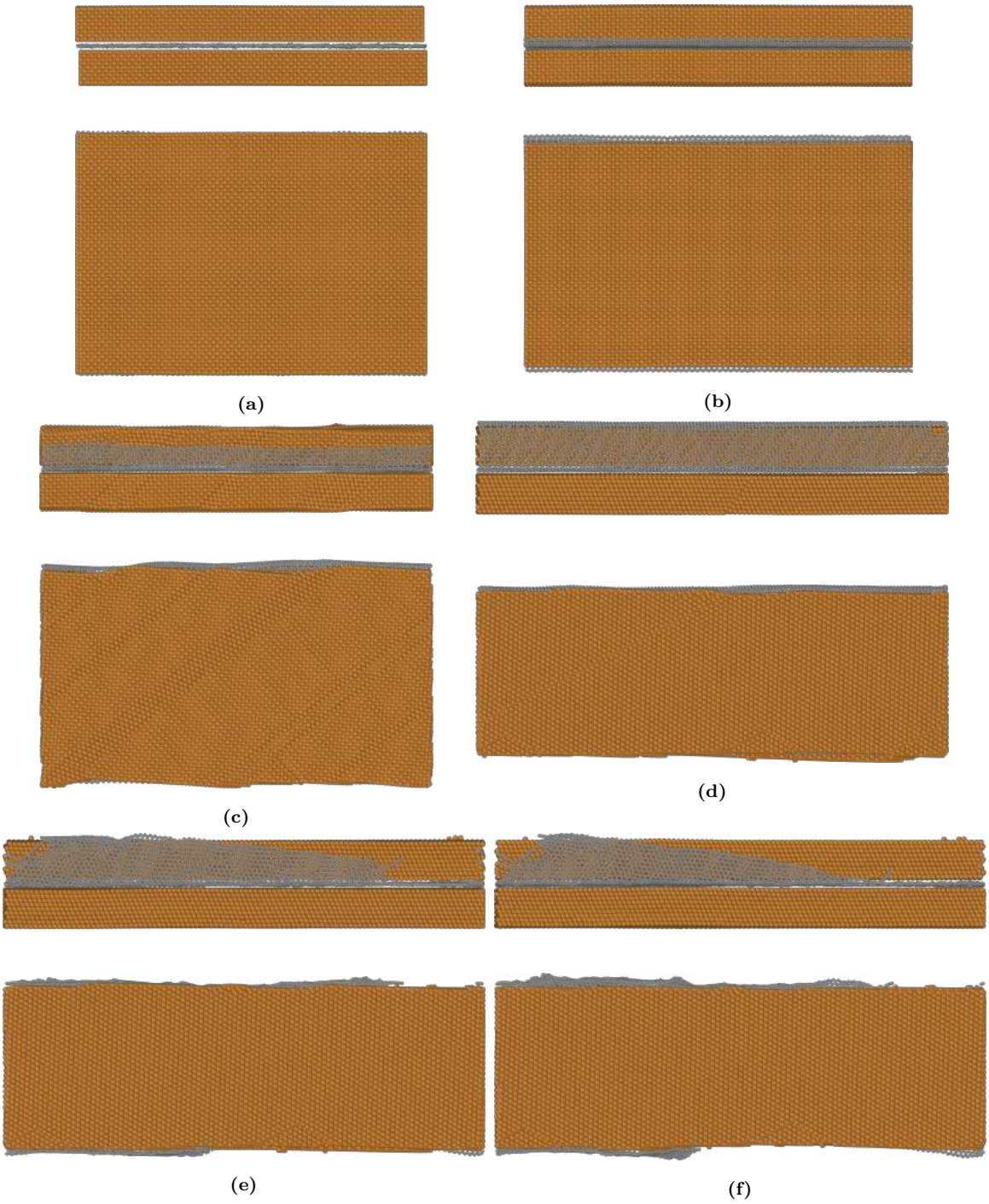

Figure C.11: Snapshots (front and top views) of the tensile test conducted in the ZZ G-Cu heterostructure with SW defects in the graphene layer at $\rho_{SW} = 0.03$ and different ε_x^s. (a) $\varepsilon_x^s = 0.0000$. Nanocomposite before straining. (b) $\varepsilon_x^s = 0.1070$, near to the σ_Y point. (c) $\varepsilon_x^s = 0.1205$, around the lower-yield point. (d) $\varepsilon_x^s = 0.3485$, around the σ_{TS} point. (e) $\varepsilon_x^s = 0.3740$. Here, failure has already taken place in the graphene layer (see figure C.12). (f) $\varepsilon_x^s = 0.4000$.

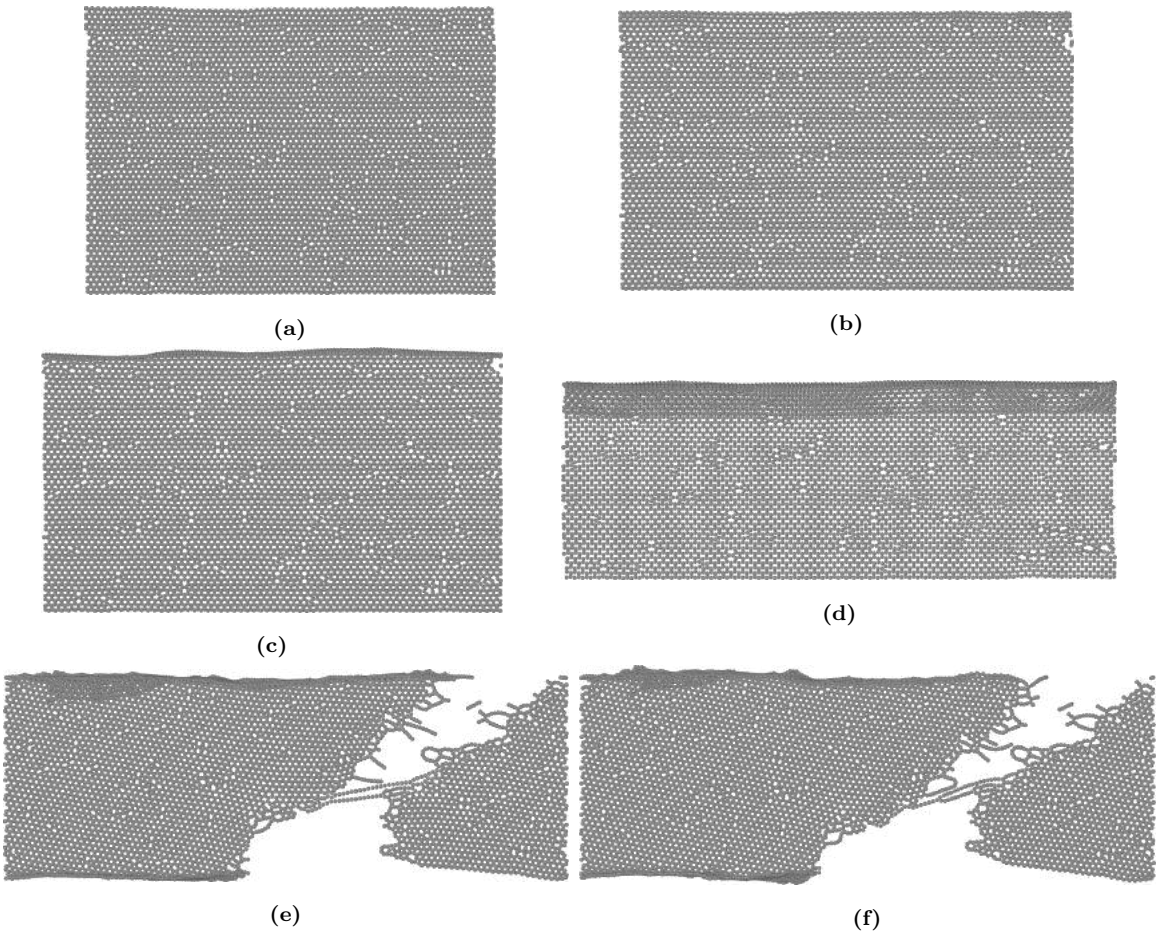

Figure C.12: Snapshots (top view) of the graphene layer in the ZZ G-Cu heterostructure with SW defects at ρ_{SW} = 0.03 and different ε_x^s. (a) ε_x^s = 0.0000. ZZ graphene layer with SW defects before straining. (b) ε_x^s = 0.1070, around the σ_Y point. (c) ε_x^s = 0.1205, around the lower-yield point. (d) ε_x^s = 0.3485, around the σ_{TS} point. (e) ε_x^s = 0.3715. Here, failure has already taken place in the graphene layer. (f) ε_x^s = 0.4000.

Bibliography

[1] K. S. Novoselov, A. K. Geim, S. V. Morozov, D. Jiang, Y. Zhang, S. V. Dubonos, I. V. Grigorieva, and A. A. Firsov, "Electric field effect in atomically thin carbon films," *Science*, vol. 306, no. 5696, pp. 666–669, 2004.

[2] K. S. Novoselov, D. Jiang, F. Schedin, T. J. Booth, V. V. Khotkevich, S. V. Morozov, and A. K. Geim, "Two-dimensional atomic crystals," *PNAS*, vol. 102, no. 30, pp. 10 451–10 453, 2005.

[3] C. Lee, X. Wei, J. W. Kysar, and J. Hone, "Measurement of the elastic properties and intrinsic strength of monolayer graphene," *Science*, vol. 321, no. 5887, pp. 385–388, 2008.

[4] C. Zhang, C. Lu, L. Pei, J. Li, R. Wang, and K. Tieu, "The negative Poisson's ratio and strengthening mechanism of nanolayered graphene/Cu composites," *Carbon*, vol. 143, pp. 125–137, 2019.

[5] C. Zhang, C. Lu, L. Pei, J. Li, and R. Wang, "Molecular dynamics simulation of the negative Poisson's ratio in graphene/Cu nanolayered composites: Implications for scaffold design and telecommunication cables," *ACS Appl. Nano Mater.*, vol. 3, no. 1, pp. 496–505, 2020.

[6] R. Ansari, S. Ajori, and B. Motevalli, "Mechanical properties of defective single-layered graphene sheets via molecular dynamics simulation," *Superlattices Microstruct.*, vol. 51, no. 2, pp. 274–289, 2012.

[7] F. Hao, D. Fang, and Z. Xu, "Mechanical and thermal transport properties of graphene with defects," *Appl. Phys. Lett.*, vol. 99, no. 4, p. 041901, 2011.

[8] Z. Li, X. Fu, Q. Guo, L. Zhao, G. Fan, Z. Li, D. Xiong, Y. Su, and D. Zhang, "Graphene quality dominated interface deformation behavior of graphene-metal composite: The defective is better," *Int. J. Plast.*, vol. 111, pp. 253–265, 2018.

[9] M. Eisenstadt, *Introduction to Mechanical Properties of Materials.* New York: Macmillan, 1971.

[10] J. Pelleg, *Mechanical properties of materials.* Dordrecht, Netherlands: Springer, 2013.

[11] ASM International, *Atlas of Stress-strain Curves*, 2nd ed. Materials Park, OH: ASM International, 2002.

[12] V. H. Carneiro, J. Meireles, and H. Puga, "Auxetic materials - a review," *Mater. Sci.-Pol.*, vol. 31, no. 4, p. 561–571, 2013.

[13] M. Mir, M. N. Ali, J. Sami, and U. Ansari, "Review of mechanics and applications of auxetic structures," *Adv. Mater. Sci. Eng.*, vol. 2014, pp. 1–17, 2014.

[14] Z. Zhang, H. Zhu, R. Yuan, S. Wang, T. Fan, Y. Rezgui, and D. Zhang, "Auxetic interpenetrating composites: A new approach to non-porous materials with a negative or zero Poisson's ratio," *Compos. Struct.*, vol. 243, p. 112195, 2020.

[15] Z. Q. Wang, T. Y. Lü, H. Q. Wang, Y. P. Feng, and J. C. Zheng, "Review of borophene and its potential applications," *Front. Phys.*, vol. 14, no. 3, p. 33403, 2019.

[16] B. Wang, Q. Wu, Y. Zhang, L. Ma, and J. Wang, "Auxetic B_4N monolayer: A promising 2D material with in-plane negative Poisson's ratio and large anisotropic mechanics," *ACS Appl. Mater. Interfaces*, vol. 11, no. 36, pp. 33 231–33 237, 2019.

[17] G. Liu, Q. Zeng, P. Zhu, R. Quhe, and P. Lu, "Negative Poisson's ratio in monolayer $PdSe_2$," *Comput. Mater. Sci.*, vol. 160, pp. 309–314, 2019.

[18] A. Yeganeh-Haeri, D. J. Weidner, and J. B. Parise, "Elasticity of α-cristobalite: A silicon dioxide with a negative Poisson's ratio," *Science*, vol. 257, no. 5070, pp. 650–652, 1992.

[19] R. H. Baughman, J. M. Shacklette, A. A. Zakhidov, and S. Stafström, "Negative Poisson's ratios as a common feature of cubic metals," *Nature*, vol. 392, no. 6674, p. 362–365, 1998.

[20] J. Hou, B. Deng, H. Zhu, Y. Lan, Y. Shi, S. De, L. Liu, P. Chakraborty, F. Gao, and Q. Peng, "Magic auxeticity angle of graphene," *Carbon*, vol. 149, pp. 350–354, 2019.

[21] Y. Fan, Y. Xiang, and H. Shen, "Temperature-dependent mechanical properties of graphene/Cu nanocomposites with in-plane negative Poisson's ratios," *Research*, vol. 2020, p. 1–12, 2020.

[22] J. Warner, F. Schaffel, M. Rummeli, and A. Bachmatiuk, *Graphene: Fundamentals and emergent applications*. Waltham, MA: Elsevier Science, 2013.

[23] V. Skakalova and A. B. Kaiser, *Graphene: Properties, Preparation, Characterization and Applications*, 2nd ed. Duxford, United Kingdom: Elsevier Science, 2021.

[24] G. Van Lier, C. Van Alsenoy, V. Van Doren, and P. Geerlings, "Ab initio study of the elastic properties of single-walled carbon nanotubes and graphene," *Chem. Phys. Lett.*, vol. 326, no. 1, pp. 181–185, 2000.

[25] E. Konstantinova, S. O. Dantas, and P. M. Barone, "Electronic and elastic properties of two-dimensional carbon planes," *Phys. Rev. B*, vol. 74, p. 035417, 2006.

[26] F. Liu, P. Ming, and J. Li, "Ab initio calculation of ideal strength and phonon instability of graphene under tension," *Phys. Rev. B*, vol. 76, p. 064120, 2007.

[27] A. Cao and J. Qu, "Atomistic simulation study of brittle failure in nanocrystalline graphene under uniaxial tension," *Appl. Phys. Lett.*, vol. 102, no. 7, p. 071902, 2013.

[28] F. Gayk, J. Ehrens, T. Heitmann, P. Vorndamme, A. Mrugalla, and J. Schnack, "Young's moduli of carbon materials investigated by various classical molecular dynamics schemes," *Phys. E: Low-Dimens. Syst. Nanostructures.*, vol. 99, pp. 215–219, 2018.

[29] I. V. Lebedeva, A. S. Minkin, A. M. Popov, and A. A. Knizhnik, "Elastic constants of graphene: Comparison of empirical potentials and DFT calculations," *Phys. E: Low-Dimens. Syst. Nanostructures.*, vol. 108, pp. 326–338, 2019.

[30] H. Zhao, K. Min, and N. R. Aluru, "Size and chirality dependent elastic properties of graphene nanoribbons under uniaxial tension," *Nano Lett.*, vol. 9, no. 8, pp. 3012–3015, 2009.

[31] Z. Ni, H. Bu, M. Zou, H. Yi, K. Bi, and Y. Chen, "Anisotropic mechanical properties of graphene sheets from molecular dynamics," *Phys. B: Condens. Matter*, vol. 405, no. 5, pp. 1301–1306, 2010.

[32] F. Ma, Y. Sun, D. Ma, K. Xu, and P. K. Chu, "Reversible phase transformation in graphene nano-ribbons: Lattice shearing based mechanism," *Acta Mater.*, vol. 59, no. 17, pp. 6783–6789, 2011.

[33] M. A. N. Dewapriya and R. K. N. D. Rajapakse, "Molecular dynamics simulations and continuum modeling of temperature and strain rate dependent fracture strength of graphene with vacancy defects," *J. Appl. Mech.*, vol. 81, no. 8, p. 081010, 2014.

[34] J. Zhang, T. Ragab, and C. Basaran, "Comparison of fracture behavior of defective armchair and zigzag graphene nanoribbons," *Int. J. Damage Mech.*, vol. 28, no. 3, pp. 325–345, 2019.

[35] M. Neek-Amal and F. M. Peeters, "Linear reduction of stiffness and vibration frequencies in defected circular monolayer graphene," *Phys. Rev. B*, vol. 81, p. 235437, 2010.

[36] N. Jing, Q. Xue, C. Ling, M. Shan, T. Zhang, X. Zhou, and Z. Jiao, "Effect of defects on Young's modulus of graphene sheets: a molecular dynamics simulation," *RSC Adv.*, vol. 2, pp. 9124–9129, 2012.

[37] L. Xu, N. Wei, and Y. Zheng, "Mechanical properties of highly defective graphene: from brittle rupture to ductile fracture," *Nanotechnology*, vol. 24, no. 50, p. 505703, 2013.

[38] J. Kotakoski, J. C. Meyer, S. Kurasch, D. Santos-Cottin, U. Kaiser, and A. V. Krasheninnikov, "Stone-Wales-type transformations in carbon nanostructures driven by electron irradiation," *Phys. Rev. B*, vol. 83, p. 245420, 2011.

[39] A. V. Krasheninnikov, K. Nordlund, M. Sirviö, E. Salonen, and J. Keinonen, "Formation of ion-irradiation-induced atomic-scale defects on walls of carbon nanotubes," *Phys. Rev. B*, vol. 63, p. 245405, 2001.

[40] F. Banhart, J. Kotakoski, and A. V. Krasheninnikov, "Structural defects in graphene," *ACS Nano*, vol. 5, no. 1, pp. 26–41, 2011.

[41] A. Hashimoto, K. Suenaga, A. Gloter, K. Urita, and S. Iijima, "Direct evidence for atomic defects in graphene layers," *Nature*, vol. 430, no. 7002, p. 870–873, 2004.

[42] M. M. Ugeda, I. Brihuega, F. Guinea, and J. M. Gómez-Rodríguez, "Missing atom as a source of carbon magnetism." *Phys. Rev. Lett.*, vol. 104, no. 9, p. 096804, 2010.

[43] J. C. Meyer, C. Kisielowski, R. Erni, M. D. Rossell, M. F. Crommie, and A. Zettl, "Direct imaging of lattice atoms and topological defects in graphene membranes," *Nano Lett.*, vol. 8, no. 11, pp. 3582–3586, 2008.

[44] M. Gass, U. Bangert, A. Bleloch, P. Wang, R. Raveendran-Nair, and A. Geim, "Free-standing graphene at atomic resolution," *Nat. Nanotechnol.*, vol. 3, pp. 676–681, 2008.

[45] L. Xu, N. Wei, and Y. Zheng, "Mechanical properties of highly defective graphene: from brittle rupture to ductile fracture," *Nanotechnology*, vol. 24, no. 50, p. 505703, 2013.

[46] A. Krasheninnikov, P. Lehtinen, A. Foster, and R. Nieminen, "Bending the rules: Contrasting vacancy energetics and migration in graphite and carbon nanotubes," *Chem. Phys. Lett.*, vol. 418, no. 1, pp. 132–136, 2006.

[47] A. A. El-Barbary, R. H. Telling, C. P. Ewels, M. I. Heggie, and P. R. Briddon, "Structure and energetics of the vacancy in graphite," *Phys. Rev. B*, vol. 68, p. 144107, 2003.

[48] L. Li, S. Reich, and J. Robertson, "Defect energies of graphite: Density-functional calculations," *Phys. Rev. B*, vol. 72, p. 184109, 2005.

[49] A. Stone and D. Wales, "Theoretical studies of icosahedral C60 and some related species," *Chem. Phys. Lett.*, vol. 128, no. 5, pp. 501–503, 1986.

[50] M. Lusk and L. Carr, "Nano-engineering defect structures on graphene," *Phys. Rev. Lett.*, vol. 100, p. 175503, 2008.

[51] W. Lawrence and B. A. Bragg, "XLII. The crystalline structure of copper," *Lond. Edinb. Dub. Philos. Mag. J. Sci.*, vol. 28, no. 165, pp. 355–360, 1914.

[52] Y. Guan, B. Chen, J. Zou, T. B. Britton, J. Jiang, and F. P. Dunne, "Crystal plasticity modelling and HR-DIC measurement of slip activation and strain localization in single and oligo-crystal Ni alloys under fatigue," *Int. J. Plast.*, vol. 88, pp. 70–88, 2017.

[53] W. D. Nielsen. Metallurgy of copper-base alloys. [Online]. Available: http://www.copper.org/resources/properties/703_5/

[54] P. Sanders, J. Eastman, and J. Weertman, "Elastic and tensile behavior of nanocrystalline copper and palladium," *Acta Mater.*, vol. 45, no. 10, pp. 4019–4025, 1997.

[55] D. Y. W. Yu and F. Spaepen, "The yield strength of thin copper films on Kapton," *J. Appl. Phys.*, vol. 95, no. 6, pp. 2991–2997, 2004.

[56] S. Zhang, M. Sakane, T. Nagasawa, and K. Kobayashi, "Mechanical properties of copper thin films used in electronic devices," *Procedia Eng.*, vol. 10, pp. 1497–1502, 2011.

[57] S. Jha, D. Balakumar, and R. Paluchamy, "Experimental analysis of microstructure and mechanical properties of copper and brass based alloys," *Int. J. Automot. Mech. Eng.*, vol. 11, pp. 2317–2331, 2015.

[58] L. B. Freund and S. Suresh, *Thin Film Materials: Stress, Defect Formation and Surface Evolution*. Cambridge: Cambridge University Press, 2004.

[59] Y. Gao, H. Wang, J. Zhao, C. Sun, and F. Wang, "Anisotropic and temperature effects on mechanical properties of copper nanowires under tensile loading," *Comput. Mater. Sci.*, vol. 50, no. 10, pp. 3032–3037, 2011.

[60] Y. T. Gu and H. F. Zhan, "MD investigations for mechanical properties of copper nanowires with and without surface defects," *Int. J. Comput. Methods*, vol. 09, no. 01, p. 1240003, 2012.

[61] K. M. Tsysar, V. S. Zelenskiy, V. A. Vdovin, and V. G. Andreev, "Size effect in dependence of the elastic characteristics of thin copper films on their thickness," *Zhurnal Radioelektroniki - J. Radio Electronics*, vol. 12, 2017.

[62] J. Hwang, T. Yoon, S. H. Jin, J. Lee, T. Kim, S. H. Hong, and S. Jeon, "Enhanced mechanical properties of graphene/copper nanocomposites using a molecular-level mixing process," *Adv. Mater.*, vol. 25, no. 46, pp. 6724–6729, 2013.

[63] R. Jiang, X. Zhou, Q. Fang, and Z. Liu, "Copper–graphene bulk composites with homogeneous graphene dispersion and enhanced mechanical properties," *Mater. Sci. Eng. A*, vol. 654, pp. 124–130, 2016.

[64] M. Cao, D. Xiong, Z. Tan, G. Ji, B. Amin-Ahmadi, Q. Guo, G. Fan, C. Guo, Z. Li, and D. Zhang, "Aligning graphene in bulk copper: Nacre-inspired nanolaminated architecture coupled with in-situ processing for enhanced mechanical properties and high electrical conductivity," *Carbon*, vol. 117, pp. 65–74, 2017.

[65] V. Konakov, O. Kurapova, E. Solovyeva, I. Lomakin, and I. Archakov, "Synthesis, structure and mechanical properties of bulk "copper-graphene" composites," *Rev. Adv. Mater. Sci.*, vol. 57, no. 2, pp. 151–157, 2018.

[66] O. Y. Kurapova, I. Lomakin, E. Solovieva, I. Y. Archakov, and V. Konakov, "Oxidation resistance and microhardness of NI-YSZ composites, manufactured by powder metallurgy technique." *Rev. Adv. Mater. Sci.*, vol. 52, pp. 99–106, 2017.

[67] D. T. Ho, S. Park, S. Kwon, K. Park, and S. Y. Kim, "Negative Poisson's ratios in metal nanoplates," *Nat. Commun.*, vol. 5, no. 1, p. 3255–3261, 2014.

[68] A. Satoh, *Introduction to Practice of Molecular Simulation: Molecular Dynamics, Monte Carlo, Brownian Dynamics, Lattice Boltzmann and Dissipative Particle Dynamics*. London: Elsevier Science, 2011.

[69] D. Frenkel and B. Smit, *Understanding Molecular Simulation: From Algorithms to Applications*, 2nd ed. San Diego: Academic Press, 2002, vol. 1.

[70] M. R. Chávez-Castillo, "Estudio de las propiedades mecánicas de siliceno mediante simulaciones de dinámica molecular," Ph.D. dissertation, Instituto de Física, Benemérita Universidad Autónoma de Puebla, Puebla, Mexico, 2016.

[71] M. P. Allen and D. J. Tildesley, *Computer Simulation of Liquids*. New York: Clarendon Press, 1989.

[72] L. Verlet, "Computer "experiments" on classical fluids. I. Thermodynamical properties of Lennard-Jones molecules," *Phys. Rev.*, vol. 159, pp. 98–103, 1967.

[73] S. Plimpton, "Fast parallel algorithms for short-range molecular dynamics," *J. Comput. Phys.*, vol. 117, no. 1, pp. 1–19, 1995.

[74] Sandia National Laboratories. LAMMPS molecular dynamics simulator. [Online]. Available: http://lammps.sandia.gov/

[75] S. Nosé, "A unified formulation of the constant temperature molecular dynamics methods," *J. Chem. Phys.*, vol. 81, pp. 511–519, 1984.

[76] W. G. Hoover, "Canonical dynamics: Equilibrium phase-space distributions," *Phys. Rev. A*, vol. 31, pp. 1695–1697, 1985.

[77] M. A. N. Dewapriya, "Molecular dynamics study of effects of geometric defects on the mechanical properties of graphene," M.S. thesis, The University of British Columbia, Vancouver, 2012.

[78] S. Huang, D. S. Mainardi, and P. B. Balbuena, "Structure and dynamics of graphite-supported bimetallic nanoclusters," *Surf. Sci.*, vol. 545, no. 3, pp. 163–179, 2003.

[79] S. J. Stuart, A. B. Tutein, and J. A. Harrison, "A reactive potential for hydrocarbons with intermolecular interactions," *J. Chem. Phys.*, vol. 112, no. 14, pp. 6472–6486, 2000.

[80] Y. Mishin, M. J. Mehl, D. A. Papaconstantopoulos, A. F. Voter, and J. D. Kress, "Structural stability and lattice defects in copper: Ab initio, tight-binding, and embedded-atom calculations," *Phys. Rev. B*, vol. 63, p. 224106, 2001.

[81] J. E. Lennard-Jones, "On the determination of molecular fields. II. From the equation of state of a gas," *Proc. R. Soc. Lond. A*, vol. 106, no. 738, pp. 463–477, 1924.

[82] D. W. Brenner, "Empirical potential for hydrocarbons for use in simulating the chemical vapor deposition of diamond films," *Phys. Rev. B*, vol. 42, pp. 9458–9471, 1990.

[83] ——, "Erratum: Empirical potential for hydrocarbons for use in simulating the chemical vapor deposition of diamond films," *Phys. Rev. B*, vol. 46, pp. 1948–1948, 1992.

[84] D. W. Brenner, J. A. Harrison, C. T. White, and R. J. Colton, "Molecular dynamics simulations of the nanometer-scale mechanical properties of compressed buckminsterfullerene," *Thin Solid Films*, vol. 206, no. 1, pp. 220–223, 1991.

[85] C. Wade, "Hessian of the AIREBO potential," M.S. thesis, Gdańsk Tech, Gdańsk, Poland, 2015.

[86] M. S. Daw and M. I. Baskes, "Embedded-atom method: Derivation and application to impurities, surfaces, and other defects in metals," *Phys. Rev. B*, vol. 29, pp. 6443–6453, 1984.

[87] J. Adams, "Bonding energy models," in *Encyclopedia of Materials: Science and Technology*, K. J. Buschow, R. W. Cahn, M. C. Flemings, B. Ilschner, E. J. Kramer, S. Mahajan, and P. Veyssière, Eds. Oxford: Elsevier, 2001, pp. 763–767.

[88] A. Stukowski, "Visualization and analysis of atomistic simulation data with OVITO-the Open Visualization Tool," *Model. Simul. Mat. Sci. Eng.*, vol. 18, no. 1, pp. 1–7, 2010.

BUAP

Oficio No. IF-SACAD236/2021

Asunto: **Oficio de modalidad de titulación.**

MTRO. RICARDO VALDERRAMA VALDEZ
Director de Administración Escolar
Benemérita Universidad Autónoma de Puebla
Presente

El que suscribe, Director del Instituto de Física "Ing. Luis Rivera Terrazas", le informo que **THAISON TALLES FELIX**, matrícula: **219470779**, presentará y defenderá su examen de grado de **MAESTRÍA EN CIENCIAS (EN LA ESPECIALIDAD DE CIENCIA DE MATERIALES)** en la **MODALIDAD DE PRESENTACION DE TESIS**, cuyo título es: **"ROLE OF DEFECTS IN THE MECHANICAL PROPERTIES OF GRAPHENE-COPPER HETEROSTRUCTURES"**, que se llevará a cabo el día **jueves 28 de octubre de 2021 a las 17:00 horas**. Se informa que dicho **EXAMEN DE GRADO SERÁ EN LÍNEA** debido a la emergencia sanitaria por el virus SARS CoV-2 a través de la plataforma *Meet* de la VIEP. El Jurado Examinador estará integrado por:

Dra. Minerva González Melchor	**Presidente**
Dr. José Luis Eustolio Carrillo Estrada	**Secretario**
Dr. Alfredo Díaz de Anda.	**Vocal**
Dra. Lilia Meza Montes.	**Vocal**

Sin otro asunto que el particular, aprovecho la ocasión para enviarle un cordial saludo.

A T E N T A M E N T E
"Pensar Bien, Para Vivir Mejor"
Puebla, Pue., a 25 de octubre de 2021

DR. FELIPE PÉREZ RODRÍGUEZ
DIRECTOR

C.c.p. Archivo
DR*FPR/DR*AMB/*mhr

Instituto de Física
"Luis Rivera Terrazas"

Av. San Claudio esq. 18 Sur, Edif. IF1,
Ciudad Universitaria, Col. San Manuel
Puebla, Pue. C.P. 72570
01 (222) 229 55 00 Ext. 5610, 5611, 2008